HTL TR No. 94

EXPERIMENTAL TURBULENT VISCOSITIES FOR SWIRLING FLOW IN A STATIONARY ANNULUS

by

C. J. SCOTT and D. R. RASK

August, 1971

Research Supported by
U. S. Army Research Office-Durham
Contract Number DAH-CO4-67-C-0021

Heat Transfer Laboratory

Department of Mechanical Engineering

Unclassified

Security Classification

DOCUMENT CONTROL DATA - R & D

(Security classification of title, body of abstract and indexing annotation must be entered when the overall report is classified)

1. ORIGINATING ACTIVITY (Corporate author) Department of Mechanical Engineering School of Mechanical and Aerospace Engineering University of Minnesota	2a. REPORT SECURITY CLASSIFICATION 2b. GROUP

3. REPORT TITLE

Experimental Turbulent Viscosities for Swirling Flow in a Stationary Annulus

4. DESCRIPTIVE NOTES (Type of report and inclusive dates)

Research Report

5. AUTHOR(S) (First name, middle initial, last name)

Charles J. Scott
Dean R. Rask

6. REPORT DATE	7a. TOTAL NO. OF PAGES	7b. NO. OF REFS
August 1, 1971	103	66

8a. CONTRACT OR GRANT NO.	9a. ORIGINATOR'S REPORT NUMBER(S)
DAH C04-67-C-0021 b. PROJECT NO.	HTL TR No. 94
c. d.	9b. OTHER REPORT NO(S) (Any other numbers that may be assigned this report)

10. DISTRIBUTION STATEMENT

This document has been approved for public release and sale; Its distribution is unlimited.

11. SUPPLEMENTARY NOTES	12. SPONSORING MILITARY ACTIVITY
	U.S. Army Research Office - Durham Box CM, Duke Station Durham, North Carolina, 27706

13. ABSTRACT

An important feature of many flows encountered in practice (such as in turbomachinery) is the fact that the streamlines may be curved, thereby introducing a pressure gradient in the direction perpendicular to the main flow direction. The purpose of the present research is to isolate the effects of curvature (swirl) on the turbulence and hence the transport properties.

The experimental effort is concerned with mapping out the details of the developing axial and decaying tangential velocity fields using isothermal air as the working fluid in an annulus with a single diameter ratio ($d_i/d_o = 0.4$) and at a single bulk Reynolds number ($Re = \bar{U}D_h/\nu = 130{,}000$). In this report, interest is centered on a critical discussion of the data reduction techniques for obtaining the radial variations of the axial and tangential momentum diffusivities.

DD FORM 1 NOV 68 1473 (PAGE 1)

S/N 0101-807-6811

Unclassified

Security Classification

A-31408

14. KEY WORDS	LINK A ROLE	LINK A WT	LINK B ROLE	LINK B WT	LINK C ROLE	LINK C WT
Vortex flows						
Swirl flows						
Turbulent						
Momentum Diffusivity						
Turbulent Viscosity						
Angular Momentum						

EXPERIMENTAL TURBULENT VISCOSITIES FOR SWIRLING FLOW IN A STATIONARY ANNULUS

C. J. Scott and D. R. Rask

August, 1971

Research supported by
U.S. Army Research Office - Durham
Contract Number DAH-CO4-67-C-0021

Heat Transfer Laboratory
Department of Mechanical Engineering
University of Minnesota
Minneapolis, Minnesota 55455

ABSTRACT

An important feature of many flows encountered in practice, (such as in turbomachinery), is the fact that the streamlines may be curved, thereby introducing a pressure gradient in the direction perpendicular to the main flow direction. The purpose of the present research is to isolate the effects of curvature (swirl) on the turbulence and hence the transport properties.

The experimental effort is concerned with mapping out the details of the developing axial and decaying tangential velocity fields using isothermal air as the working fluid in an annulus with a single diameter ratio ($d_i/d_o = 0.4$) and at a single bulk Reynolds number ($Re = \bar{U}D_h/\nu = 130{,}000.$) In this report, interest is centered on a critical discussion of the data reduction techniques for obtaining the radial variations of the axial and tangential momentum diffusivities.

NOMENCLATURE

A,B	coefficients in Eq. 22
C_1,C_2,C_3	constants in least squares fits
C_{fx}	local axial skin-friction coefficient $C_{fx} = \tau/(\frac{1}{2}\rho u_1^2)$
d_i	inner diameter of annulus
d_o	outer diameter of annulus
D_h	hydraulic diameter, $D_h = d_o - d_i$
k	Karman constant, $k = 0.4$
l	mixing length
$\dot{m}$	mass flow rate
n	velocity exponent (see Appendix B)
p	pressure
r, r_m, r_i, r_o	radius, radius of maximum axial velocity, inner wall radius, outer wall radius
R	gas constant
Re_{D_h}	Reynolds number, $Re_{D_h} = \bar{U}D_h/\nu$
T	temperature
u	axial velocity component
u_1	axial velocity at outer edge of axial boundary layer
$\bar{u}$	average axial velocity
u^*	axial shear stress velocity, $u^* = \sqrt{\tau/\rho}$
u^+	law-of-the-wall variable, $u^+ = u/u^*$
v	radial velocity component
w	tangential velocity component
x	axial coordinate, axial distance from inlet trip
y	distance from wall

Greek Symbols

α, α_{crit}	angular position of cylindrical probe pressure tap relative to the flow direction, value of α at which pressure tap indicates the static pressure
ε	turbulent diffusivity for momentum defined in Eq's. 4 and 9
μ	dynamic viscosity of air
ν	kinematic viscosity of air
π	Turbulent energy production, Eq. 3
ρ	density
τ, τ_i, τ_o	wall shear stress, shear stress at inner wall, shear stress at outer wall
$\bar{\phi}$	inlet vane setting
ϕ	flow angle, Fig. 9

Subscripts

atm	atmospheric
i	inside wall
o	outside wall
max	absolute maximum
rx	axial component
rθ	tangential component
$\tau_{rx} = 0$	locus of zero axial shear
$\tau_{r\theta} = 0$	locus of zero tangential shear

EXPERIMENTAL TURBULENT VISCOSITIES FOR SWIRLING FLOW IN A STATIONARY ANNULUS

by C. J. Scott and D. R. Rask

INTRODUCTION

An important feature of many swirling flows encountered in practice (such as in turbomachinery) is the existence of strongly curved streamlines that introduce a pressure variation in a direction perpendicular to the main flow. An engineer's principal hope of understanding such an obviously complex flow system is through a synthesis of some simpler modes into analytically tractable forms or else through laboratory simulations. The former approach has only been fruitful in laminar swirl situations where the transport properties are known. The availability of digital computers and refined numerical schemes have only recently resulted in a clearer understanding of some of the constant-property, laminar, rotating flow systems. On the other hand, rotating turbulent flows are difficult to treat because of the lack of accurate turbulent transport coefficients. For the relatively simple case of a turbulent core vortex, the values of turbulent viscosity suggested in the literature vary ten-fold.

The experimental effort reported here is concerned with mapping out the details of the developing axial and decaying tangential velocity fields using isothermal air as the working fluid in an annulus with a single diameter ratio ($d_i/d_o = 0.4$) and at a single bulk Reynolds number ($Re = \bar{U}D_h/\nu = 130{,}000$). In this report, interest is centered on a critical discussion of the data reduction techniques for obtaining the radial variations of the axial and tangential momentum diffusivities. The annular geometry was selected because the inner and outer walls produce different effects on the swirl turbulence.

Consider a high, axial Reynolds-number, flow through an annulus. If both walls

are stationary, then if a wheel-like rotation (solid-body) is initially imparted to the flow, near the inner wall the positive radial gradient of angular momentum is known to have a stabilizing effect. Near the fixed outer boundary, a destabilizing effect is encountered. The net effect of the centripetal acceleration field is to exert a stabilizing influence on the flow which depends on the shape of the angular momentum distribution. Local stability variations modify the turbulent structure mainly through the production of turbulent energy such that the turbulent transport coefficients are inhibited. Near the outer wall - the unstable case - the net effect of the centripetal acceleration field is to increase the turbulent production and promote turbulent transport.

The characteristics of swirl flows have been investigated during the last three decades and are still the subject of extensive research. Much of the work was summarized in a symposium [1]* on "Concentrated Vortex Motion in Fluids," organized by the International Union for Theoretical and Applied Mechanics and held at the University of Michigan, Ann Arbor, Michigan, in July, 1964 as summarized in J. Fluid Mech., Vol. 21, No. -, 1965. Later in 1966, a book, Vol. 7 of "Progress in Aeronautical Sciences," [2] reports in more detail matters discussed at that particular symposium and presents revised versions of summary reports presented there.

A few practical applications of swirling flows are listed below:

1) Heat transfer per unit area as well as ratio of heat transfer to friction loss is increased if rotation is superimposed on axial flow through tubes.

2) In pipe flow, twisted tapes have been inserted to augment heat transfer. Applications here include throat regions of regeneratively-cooled rocket nozzles (where local hot spots must be avoided) or in high performance

---

* Numbers in brackets designate References at end of report.

heat exchangers.

3) A common instance of flow between concentric cylinders occurs in rotating machinery where the heat transfer characteristics of the air gap are frequently the least understood of the many heat flow paths in electric rotating equipment.

4) In gaseous nuclear reactor rocket motors, swirling motion achieves a longer hold-up time of the fissionable gas.

5) In plasma generators, a swirling motion is superimposed on the axial gas flow through the nozzle in order to move the arc attachment point on the anode circumferentially and, thereby, avoid overheating the anode material.

6) In advanced combustion chambers, swirling motion of the gases improves flow stability and combustion efficiency while reducing the heat loss through the walls.

7) With increased levels of temperature, cooling must be applied to rotating and stationary components of gas turbine disks and shrouds. From a heat transfer standpoint, this poses the question of predicting the heat transfer in passages enclosed by surfaces which are partially rotating.

8) Swirling flows are used to separate particles such as dust separators in the air intakes of helicopters hovering over dusty fields.

9) Ranque-Hilsch tube cooling devices are now in production based on the energy separation of a gas stream into a portion with higher, and another portion with lower, temperatures than the inlet temperature.

10) In certain flow regimes, the effect of swirl is to improve diffuser performance; while in others, the performance is reduced.

11) In a typical submarine condenser, the turbogenerator exhaust inlet is located on top and at one end of the condenser but is offset from the

symmetrical plane. The vapor entering the condenser through the inlet is analogous to a jet streaming tangentially into an annulus. Once within the annulus, the vapor tends to move spirally toward the opposite end of the cylinder.

12) One might add to this list atmospheric and geophysical vortical phenomena such as dust devils, waterspouts, tornadoes, whirlwinds, etc.

Swirling flows have been classified by King, Rothfus, and Kermode [3] according to the boundary conditions in the following fashion:

1) Unconfined swirling flows where the wall effects are negligible. Examples are swirling free jets, rotary gas burners, trailing vortices from aircraft wings, and swirling compressible nozzle flows.

2) Small L/D_h swirling flows in short, large-diameter, chambers where sidewall effects strongly interact with the swirl to produce significant secondary flows. An example here is core-flow containment in gaseous nuclear rockets.

3) Large L/D_h swirling flows in tubes where circumferential wall effects interact strongly with the swirl flow.

Revolving fluid flows, in which the tangential velocity distribution w(r) is described by wr = constant, are normally classified as vortex flows. The revolving fluid is caused to move inward toward the axis of revolution. If the fluid friction is low, or if the radial flux of angular momentum is high, the fluid executes a vortex motion. These flows are normally in contact with one or more solid boundaries. Flows may be rotating over stationary walls or inside confining stationary walls. The boundaries may be rotating and impart swirl to the main body of fluid by turbulent diffusion. In the case of a grounded storm funnel, both the fluid and the surroundings are rotating.

For swirling internal flows in long stationary ducts, the axial flow (u)

assumes a fully developed velocity distribution at large distances downstream and the swirl (w) decays asymptotically to zero. If wall rotation is present, a fully developed swirl profile is produced. If the swirl ratio is sufficiently large*, stagnant regions and regions of reversed flow may exist in the entrance section. This phenomenon, known as vortex breakdown, may occur in swirl diffusers and influences their performance. It helps to stabilize flames and alters the flow from rotating jets. It has been proposed to contain a volume of fluid within a body of different fluid with relatively little mixing.

Bossel [4] investigated laminar vortex breakdown flows. One special case involves swirling flow in a cylindrical stream tube. These solutions are characterized by a maximum swirl angle of $\phi = 62.5°$. At larger swirl angles, a stagnation point and a reversed flow exist along the axis of the tube. The present experimental studies are confined to the subcritical case where vortex breakdown does not occur because of the difficulty in deducing distributions of turbulent transport properties with reversed local axial flows.

Another interesting feature of swirling flows is related to their hydrodynamic stability. Since particles in revolving motion tend to conserve their angular momentum, the stability criterion first proposed by Rayleigh [5] suggests that flows with positive radial angular momentum gradients are stable while flows with negative gradients are unstable. Rayleigh describes the equilibrium behavior of a fluid particle near the outer wall in a curved channel. Upon being displaced to a larger radius, the fluid possesses a larger angular momentum than its neighbors. The centrifugal force on the displaced particles ($\rho w^2/r$) will be

---

* The term swirl rate (ratio) used here is subjective in nature. One could say a swirl flow is of a high rate if in the inlet region $u_{max} << w_{max}$ (u_{max} and w_{max} are the maximum axial and tangential velocities). The largest swirl rate reported here has a w_{max}/u_{max} ratio of 1.6 at the first data station ($x/D_h = 1.7$).

greater than the centripetal pressure gradient existing at the new location and the particle will tend to be displaced to a still larger radius. Therefore, a radial displacement is unstable near the outer wall. Near the inner wall, the converse is true. Rotating flows with solid body rotation ($w = cr$) are very stable, "free" vortex flows ($wr = c$) are neutrally stable, and the boundary layer region inside the channel wall is extremely unstable.

In 1932 and 1936, Taylor [6, 7, 8] investigated fully-developed rotating turbulent flow between concentric rotating cylinders. In Taylor's rotating cylinder, the Taylor vortices appeared when the outer cylinder was stationary and the inner cylinder was rotating. In that case, the angular momentum distribution is unstable. In Gortler's experiments [9] with flows over concave and convex walls, the 3-D disturbances appeared only for flow over concave walls.

In 1935, Wattendorf [10] attempted to isolate the effect of streamline curvature on turbulent flow by using a curved channel of constant curvature and cross section. He found that for fully-developed, curved, internal flows, the turbulent viscosity data were less than that for straight flow near the inner (convex) wall and greater near the outer wall in accordance with Rayleigh's criterion of stability. Viscosities near the outer wall were up to four times corresponding inner wall values. Eskinazi and Yeh [11], and later Margolis and Lumley [12], demonstrated that the turbulent structure is dependent on the shape of the angular momentum profile. Their results with curved channel flows led to the conclusions that on the convex wall the gradient of angular momentum is positive and turbulence is suppressed; whereas on the concave wall, the gradient of angular momentum is negative and turbulence is promoted. In 1968, Bradshaw [13] concluded that the effect of streamline curvature on the turbulence is probably more important than the effect of streamline curvature on the mean equations. To conclude, the chain of reasoning is that streamline curvature influences the flow

stability, thereby modifying the local turbulence properties. Swirling flow in an annulus is adopted here as the experimental geometry because it provides variable streamline curvature and because annular flows appear to develop and decay more rapidly than pipe flows.

Four pertinent survey articles on swirling flow are by Westley [14], Kreith [15], Lavin and Fejer [16], and Gambill and Bundy [17]. In 1937, G. J. Ranque [18] applied for a vortex tube patent. In 1944, Hilsch developed a vortex cooling device which frequently bears his name. In 1946-48, Milton [19], and later Reed [20], pointed out the important phenomena occurring in vortex tubes. In 1948, Kassner and Knoernschild [21] explained the energy separation assuming that the potential vortex (wr = const) initially formed at the nozzle inlet is transformed into solid body rotation (w/r = const) as the flow proceeds axially toward the outlet. A similar analysis was given by Deissler and Perlmutter [22,23] who proposed that the axial flow was necessary in the energy separation process because most of the temperature separation occurs where the bulk flow changes from radial to axial.

In papers by Deissler and Perlmutter [22] and Donaldson and Sullivan [24], the flow is assumed to be two-dimensional or have an axial velocity proportional to the axial coordinate. In this case, the shape of the tangential velocity distribution is controlled by the radial Reynolds number, Re_r, and is independent of the tangential velocity magnitude. For very low Re_r, the tangential velocity is found to be $w \approx r$ (solid-body rotation). As Re_r increases, the velocity profile approaches $w \approx r^{-1}$ (free vortex flow) except near the axis where solid body rotation always occurs. Kreith and Margolis [25], Smithberg and Landis [26], and Thorsen and Landis [27] studied the effects of turbulent swirling motion on heat transfer from tubes. Krassner and Knoerschild [21], Hartnett and Eckert [28], Deissler and Perlmutter [23], Ragsdale [29], Keyes [30], Kerrebrock and Meghreblian

[31], Reynolds [32], Kendall [33], and Sibulkin [34], all studied forms of the Ranque-Hilsch tube.

Collatz and Gortler [35] and Talbot [36] analyzed swirling flow in pipes by linearizing the tangential momentum conservation equation and employing a constant turbulent viscosity. The simplified equation is often referred to the "swirl" equation. Kreith and Sonju [37], Rochino and Lavan [38], and Scott [39] all extended the method by varying initial conditions, using variable properties and annular geometries. Muslof [40] measured the decay of turbulent swirl in a stationary pipe. Persen [41] studied swirling inlet flow in a tube using a boundary layer approach. Rask and Scott [42] studied the decay of turbulent swirl in an annular duct. Boerner [43] employed the time-averaged Navier Stokes equations for turbulent flow for the annular geometry. In Boerner's work, the effects of turbulent transport are incorporated through the use of two apparent turbulent viscosities which are computed separately for use in the axial and tangential momentum equations. Best results, as measured by agreement with the data of Rask and Scott [42], were obtained with a tangential viscosity model that links the viscosity to tangential velocity via the average flow angle, the wall shear velocity, and the distance of the zero shear location to the wall.

From a review of the literature, it is evident that only a limited number of previous investigations, either experimental or analytical, have been devoted to vortex flows in concentric annuli. A fair number of investigators have studied the flow between concentric rotating cylinders in the absence of an axial flow, but this is relatively far removed from the present investigation.

Palanek [44] investigated swirling flow in an annular duct of diameter ratio $d_i/d_o = 0.307$. Palenek's study was initiated as an extension of an earlier work by Talcott [45] on essentially the same apparatus. Talcott investigated heat transfer characteristics in straight flow and also briefly in swirling flow. The

swirl rates used in Palenk's study were so extreme that reversed flow is observed in each case.

A study closely related to that reported here was done by Yeh [46]. The major differences were that his test section was of larger hydraulic diameter and diameter ratio, and was relatively shorter than the present test section in terms of hydraulic diameters. In an annulus, the hydraulic diameter is given by $D_h = d_o - d_i$. The pertinent dimensions of Yeh's apparatus were $d_i/d_o = 0.5$ and $D_h = 5$ inches. Yeh reported local skin friction coefficients at the inner and outer walls but the investigation is somewhat incomplete in that only straight flow and one swirl rate were investigated. Acharyn and associates [47] also analyzed the data that was obtained by Yeh. The shear stress results are in poor agreement with those reported by Yeh.

Turbulent Transport Properties

For laminar flow along a curved path, $\tau_\ell = \mu(\partial u/\partial r - u/r)$. It is a customary but questionable practice to use an analogous expression for the turbulent shear stress, i.e., $\tau_t = \rho\varepsilon_t(\partial u/\partial r - u/r)$, where ε_t represents an apparent turbulent coefficient of kinematic viscosity or the "exchange coefficient" of the mixing process. Using this approach $\tau_t = 0$ when $(\partial u/\partial r - u/r) = 0$. Kline [13] has pointed out that if an experimental shear stress is divided by an experimentally determined gradient of velocity, the ratio can go to plus or minus infinity. This leads to difficulties in plotting experimentally determined transport coefficients. For rectilinear flows, Prandtl's mixing length and Taylor's vorticity length hypotheses give $\tau_t = \ell^2|\partial u/\partial y|\partial u/\partial y$. Again the shear stress depends on the velocity gradient. ℓ^2 is the square of the mixing length and a function of the space position. Von Karman tried to relate turbulent transport properties to local conditions. His similarity of turbulent motion concept yields $\tau_t = \text{const}\ (\partial u/\partial y)^4/(\partial^2 u/\partial y^2)^2$ for rectilinear flows. This is also a

gradient model.

Prandtl [48] applied Rayleigh's instability reasoning to developed curved turbulent flows, assuming the local angular momentum (ur) constant during displacement of fluid particles perpendicular to mean streamlines and leads to $|\overline{ru'}| \approx \ell \partial(ru)/\partial r$

$$\tau r = \rho \ell v \frac{\partial (ur)}{\partial r} = \rho \ell v \left(\frac{\partial u}{\partial r} + \frac{u}{r}\right) \qquad (1)$$

where $(\partial u/\partial r + u/r)$ represents the vorticity at the point, v the normal velocity and ℓ the mixing length. This formula is identical to Prandtl's formula for shear stress in parallel motion except the velocity slope is replaced by $(\partial u/\partial r + u/r)$. Equation (1) leads to a vanishing turbulent shear stress for irrotational mean flows--a behavior contrary to the experimental observations of Taylor, Wattendorf, and Rask and Scott.

Kinney [49], in dealing with plane rotating turbulent flows, in the absence of an axial component, applied an extension of von Karman's similarity hypothesis. A family of similar velocity profiles was generated which includes both the rotational solid body case and the irrotational free vortex case. A universal constant appearing in the equations was evaluated using G. I. Taylor's rotating cylinder velocity and wall shear stress measurements. Kinney relates the local angular velocity of the fluctuating flow to the local angular velocity of the mean flow with the relation $|\overline{w'}/r| = \ell\, \partial(\overline{w}/r)/\partial r$, and concludes that in plane-curved turbulent flows which possess universal similarity, the angular velocity is a transferable quantity, just as linear momentum is a transferable quantity in rectilinear flows.

Rochino and Lavan [38] added the axial dimension to the problem in investigating turbulent swirling flow in stationary ducts by using both Taylor's modified vorticity theory and von Karman's similarity hypothesis [50]. Three possible

expressions for the turbulent shear stress were found

$$\overline{v'w'} \approx \left(\frac{\partial w}{\partial r} - \frac{w}{r}\right)^2 \text{ or } \left(\frac{\partial x}{\partial r} + \frac{w}{r}\right)^2 \text{ or } \left(\frac{\partial u}{\partial x}\right)^2 \qquad (2)$$

It is not yet established which relation is valid. The normal procedure seems to adopt an analogy to the laminar equation $\overline{v'w'} = \rho\varepsilon_t(\partial w/\partial r - w/r)$ where the eddy diffusivity for momentum is related to the mixing length ℓ by $\varepsilon_t = \text{const}\ \ell^2 \cdot (\partial w/\partial r - w/r)$. The radial dependence of the mixing length is then the focal point of the controversy. In the core flow away from any wall influence, $\ell = kr$, i.e., the mixing length increases at a rate proportional to the distance from the axis of symmetry. Near the walls, the mixing length increases at a rate proportional to the distance from the wall according to Prandtl. Since the annular geometry has two walls with opposite wall behaviors, it provides a versatile test geometry to study the anomalous shear stress assumptions.

Both swirl and an annular geometry generate asymmetric mean axial velocity distributions such that the locus of zero axial shear and the point of zero velocity gradient do not coincide. The computed ε_t values are negative in a small range of radial distances. Both Wattendorf [10] and Eskinazi and Yeh [11] showed that in a fully-developed curved channel having an unsymmetrical profile, the location of the zero turbulent stress $(-\rho\overline{u'v'})$ did not occur at the point where the velocity derivative $(\partial u/\partial r)$ was zero nor where the viscous shear was zero $[\mu(\partial u/\partial r - u/r) = 0]$.

The difficulties of having opposite signs for the shear stress and the velocity gradient are discussed at great length in [13]. Alternate proposals are given. Of the three shear expressions: $\tau = \rho\varepsilon_1\ \partial u/\partial y$, $\tau = \rho\varepsilon_2\sqrt{q^2}\ \partial u/\partial y$, $\tau = \rho\varepsilon_3 q^2$, $(q^2 = \overline{u_i u_i})$; the third model proposed by Townsend, Bradshaw, and McDonald [13] is the only non-gradient model. This model requires that if a turbulent kinetic energy exists, a shear stress exists. Therefore, the production

of turbulent kinetic energy assumes increased importance. In cylindrical x, r, θ, u, v, w, coordinates, the production of total turbulent energy is [50] written for fully-developed, isotropic, swirling flow as

$$\pi = -\rho\left[\overline{v'w'}\, r\frac{\partial}{\partial r}\left(\frac{w}{r}\right) - \overline{u'v'}\,\frac{\partial u}{\partial r}\right] \tag{3}$$

The production is positive over the entire duct. If $w \equiv 0$, or with solid body rotation $w = cr$, the normal axial flow production results. For a free vortex $w = c/r$, the term $\partial(w/r)/\partial r$ is negative and the possibility of subtraction occurs depending on the correlation $\overline{v'w'}$. Therefore, swirling flows also have the difficulties of negative "apparent" tangential turbulent viscosities defined as

$$\varepsilon_t = \frac{\overline{v'w'}}{\frac{\partial w}{\partial r} - \frac{w}{r}} \tag{4}$$

It is informative to examine the equations used to deduce the turbulent shear stress and eddy diffusivities when developing profiles occur.

The Governing Equations

Consider a cylindrical coordinate system with x, r, and θ as the axial, radial, and azimuthal coordinates. Let u, v, and w be the time mean velocities in the x, r, and θ directions and u', v', and w' be the corresponding turbulent fluctuation velocities. Writing the continuity and Navier-Stokes equations in this notation, taking mean values with respect to time, requiring the mean motion to be steady, the mean density to be constant, density fluctuations to be negligible, and symmetry with respect to θ, results in the following governing equations [52]:

Conservation of mass

$$\frac{\partial}{\partial x}(ru) + \frac{\partial}{\partial r}(rv) = 0 \tag{5}$$

Conservation of axial momentum

$$u\frac{\partial u}{\partial x} + v\frac{\partial u}{\partial r} = -\frac{1}{\rho}\frac{\partial p}{\partial x} + \nu\nabla^2 u - \left[\frac{\partial \overline{u'^2}}{\partial x} + \frac{1}{r}\frac{\partial}{\partial r}(r\overline{u'v'})\right] \tag{6}$$

Conservation of radial momentum

$$u\frac{\partial v}{\partial x} + v\frac{\partial v}{\partial r} - \frac{w^2}{r} = -\frac{1}{\rho}\frac{\partial p}{\partial r} + \nu\left[\nabla^2 v - \frac{v}{r^2}\right] - \left[\frac{\partial}{\partial x}(\overline{u'v'}) + \frac{1}{r}\frac{\partial}{\partial r}(r\overline{v'^2}) - \frac{\overline{w'^2}}{r}\right] \tag{7}$$

Conservation of angular momentum

$$u\frac{\partial w}{\partial x} + v\frac{\partial w}{\partial r} + \frac{wv}{r} = +\nu\left[\nabla^2 w - \frac{w}{r^2}\right] - \left[\frac{\partial}{\partial x}(\overline{u'w'}) + \frac{\partial}{\partial r}(\overline{v'w'}) + 2\frac{\overline{v'w'}}{r}\right] \tag{8}$$

where $\nabla^2 = \frac{\partial^2}{\partial x^2} + \frac{\partial^2}{\partial r^2} + \frac{1}{r}\frac{\partial}{\partial r}$

The resulting set of turbulent Navier-Stokes equations is non-linear and indeterminate due to the turbulent shear terms at the extreme right in equations 6 - 8. Since there are more dependent variables than governing equations, no general method of solution exists. We shall now form integrals of the equations of motion in the following manner.

(a) Equation 6 is multiplied by r and integrated across the flow from $r = r_i$ at the inner wall to $r = r$. The result is

$$r\tau_{rx} = r_i\tau_{rx_i} - \rho u\frac{\partial}{\partial x}\int_{r_i}^{r} r u\,dr + \rho\frac{\partial}{\partial x}\int_{r_i}^{r} r u^2\,dr + \frac{\partial}{\partial x}\int_{r_i}^{r} r p\,dr + \frac{\partial}{\partial x}\int_{r_i}^{r} r\overline{u'^2}\,dr \tag{9}$$

where $\tau_{rx} = \mu\frac{\partial u}{\partial r} - \rho\overline{u'v'} = \rho(\nu + \varepsilon_{rx})\frac{\partial u}{\partial r}$

is the axial shear stress. The term $\mu\partial^2 u/\partial x^2$ was omitted in equation 9 in accordance with an order of magnitude analysis using the data taken in this study which revealed that except for regions close to the walls (closer than the closest experimental point), the turbulent viscous terms in the equations of motion are on the order of 50 times the molecular terms. Coupling this fact

with the normal assumption that in the sidewall boundary layers ($\partial/\partial x \ll \partial/\partial r$), $\nabla^2 \cong \partial^2/\partial r^2 + 1/r \cdot \partial/\partial r$ applies accurately for molecular quantities. Equation 9 is made non-dimensional by dividing by $1/2\ \rho\bar{u}^2\ r$ ($\bar{u}$ is the average axial velocity)

$$\frac{\tau_{rx}}{\frac{1}{2}\rho\bar{u}^2} = \frac{r_i}{r}\frac{\tau_{rx_i}}{\frac{1}{2}\rho\bar{u}^2} - \frac{u}{\frac{1}{2}\bar{u}^2 r}\frac{\partial}{\partial x}\int_{r_i}^{r} r u\,dr + \frac{1}{\frac{1}{2}\bar{u}^2 r}\frac{\partial}{\partial x}\int_{r_i}^{r} r u^2\,dr \qquad (9')$$

$$+ \frac{1}{\frac{1}{2}\rho\bar{u}^2 r}\frac{\partial}{\partial x}\int_{r_i}^{r} r P\,dr + \frac{1}{\frac{1}{2}\rho\bar{u}^2 r}\frac{\partial}{\partial x}\int_{r_i}^{r} r\overline{u'^2}\,dr$$

The five terms on the right-hand side of equation (9') represent

1) The axial shear on the inner wall of the annulus
2) Mean velocity changes
3) Kinetic energy changes
4) Pressure changes
5) Turbulence intensity changes

Integrating across the entire annulus yields the following relevant integral relationship

$$r_o\tau_{rx_o} - r_i\tau_{rx_i} = \frac{d}{dx}\left(\int_{r_i}^{r_o}(P + u^2 + \overline{u'^2})\ r\,dr\right) \qquad (10)$$

where the left side corresponds to the total shear force per unit length ($\tau_{rx_i} < 0$) and the right side represents the change in axial flux of linear momentum. The turbulence level and the radial pressure variations are important here because of the tangential velocity.

(b) Equation 8 is multiplied by r^2 and integrated from the inner wall outward (again neglecting $\mu\partial^2 w/\partial x^2$)

$$r^2\tau_{r\theta_r} = r_i^2\tau_{r\theta_i} + \rho\frac{\partial}{\partial x}\int_{r_i}^{r} uwr^2dr - \rho wr^2\frac{\partial}{\partial x}\int_{r_i}^{r} urdr + \rho\frac{\partial}{\partial x}\int_{r_i}^{r}\overline{u'w'}rdr \tag{11}$$

The four terms on the right-hand side of equation 11 represent

1) The torque per unit length on the inner wall of the annulus
2) Change in axial flux of angular momentum between inner wall and radial location r
3) Effects of axial acceleration on the axial flux of angular momentum
4) The turbulence shear stress $\tau_{\theta x} \approx \overline{u'w'}$

Integration over the entire annular gap yields

$$r_o^2\tau_{r\theta_o} - r_i^2\tau_{r\theta_i} = \rho\frac{d}{dx}\left(\int_{r_i}^{r_o}(uw + \overline{u'w'})r^2dr\right) \tag{12}$$

The left-hand side is the total torque per unit length while the right-hand side is the change in the axial flux of angular momentum. Equation 11 is made non-dimensional by division by $1/2\ \rho\overline{u}^2r^2$

$$\frac{\tau_{r\theta_r}}{\frac{1}{2}\rho\overline{u}^2} = \frac{r_i^2}{r^2}\frac{\tau_{r\theta_i}}{\frac{1}{2}\rho\overline{u}^2} + \frac{1}{\frac{1}{2}\overline{u}^2r^2}\frac{\partial}{\partial x}\int_{r_i}^{r} uwr^2dr - \frac{w}{\frac{1}{2}\overline{u}^2r}\frac{\partial}{\partial x}\int_{r_i}^{r} urdr + \frac{1}{\frac{1}{2}\overline{u}^2r^2}\frac{\partial}{\partial x}\int_{r_i}^{r}\overline{u'w'}r^2dr \tag{11'}$$

These equations do not assume that the direction of the shear stress is the same as the resultant velocity or resultant velocity gradient.

The radial momentum equation integrates directly to

$$\frac{1}{\rho}\left[P(r) - P(r_i)\right] = -v^2 - \overline{v'^2} + \int_{r_i}^{r}\left(\frac{w^2 - v^2 + \overline{w'^2} - \overline{v'^2}}{r}\right) dr$$
$$+ \int_{r_i}^{r} \nu\left(\frac{\partial^2 v}{\partial r^2} + \frac{1}{r}\frac{\partial v}{\partial r} - \frac{v}{r^2}\right)dr - \frac{\partial}{\partial x}\int_{r_i}^{r}\left(uv + \overline{u'v'} - \nu\frac{\partial v}{\partial x}\right)dr \qquad (13)$$

According to Hinze [51], the term $\partial(\overline{u'v'})/\partial x$ is of smaller order of magnitude than the other turbulence terms.

Finally, the integral expression for mass conservation results from direct integration of its differential form (equation 5)

$$rv = -\frac{d}{dx}\int_{r_i}^{r} ur\,dr \qquad (14)$$

No turbulence measurements were made during the present investigation. Equations 9' and 11' were used (neglecting the fifth term in equation 9' and the fourth term of equation 11') to obtain radial profiles of axial and tangential shear. Axial wall shear values were obtained using a Preston tube or a Clauser chart. Tangential wall shear values were obtained using the flow angle at the wall, i.e., $\tau_{r\theta} = \tau_{rx} \tan \phi$.

EXPERIMENTAL APPARATUS

Eddy diffusivity models have proven to be a useful tool--particularly in adapting laminar flow solution techniques to permit calculations in complex turbulent flows. Since all diffusivity models ultimately depend on empirical methods, their value must be tested by comparison with reliable experiments. It is the intention of the present paper to describe suitable experiments carried out at the Heat Transfer Laboratory of the University of Minnesota.

The present experimental program was carried out in an open circuit wind tunnel designed for swirl flows. A detailed description of the facility is given by Rask and Scott in [42]. A schematic drawing is shown as Fig. 1. Pertinent photographs of the experimental equipment are presented in Figs. 2-5. Initially room air enters the inlet radially where airfoil-shaped guide vanes impart a swirling motion to the flow prior to entry into the annular test section. Upon emergence from the test section, the mean velocity head is recovered in a conical diffuser. The swirl is then removed from the flow in a cylindrical duct filled with straightening tubes. The flow is then monitored at an orifice, controlled by means of a low resistance by-pass and finally flows into the inlet of a blower which exhausts to the atmosphere outside of the laboratory.

The inlet section receives the initial radial inflow, imparts a swirling motion to it and finally converts the flow into the axial direction. The inflow enters between two converging, saucer-shaped, guide plates, each 48 inches in diameter with a radius of curvature of 42 inches. Twelve airfoil-shaped inlet guide vanes are evenly spaced on an 18-inch circumference. The guide vanes are collectively rotated, thereby producing variable swirl velocities. The vane angle setting, $\overline{\phi}$, corresponding to a straight axial flow is designated as zero degrees. Increasing the vane angle of attack increases the downwash velocities behind a blade and increases the resulting tangential velocities. The airstream acquires angular momentum in passing through the cascade of vanes at the inlet of the

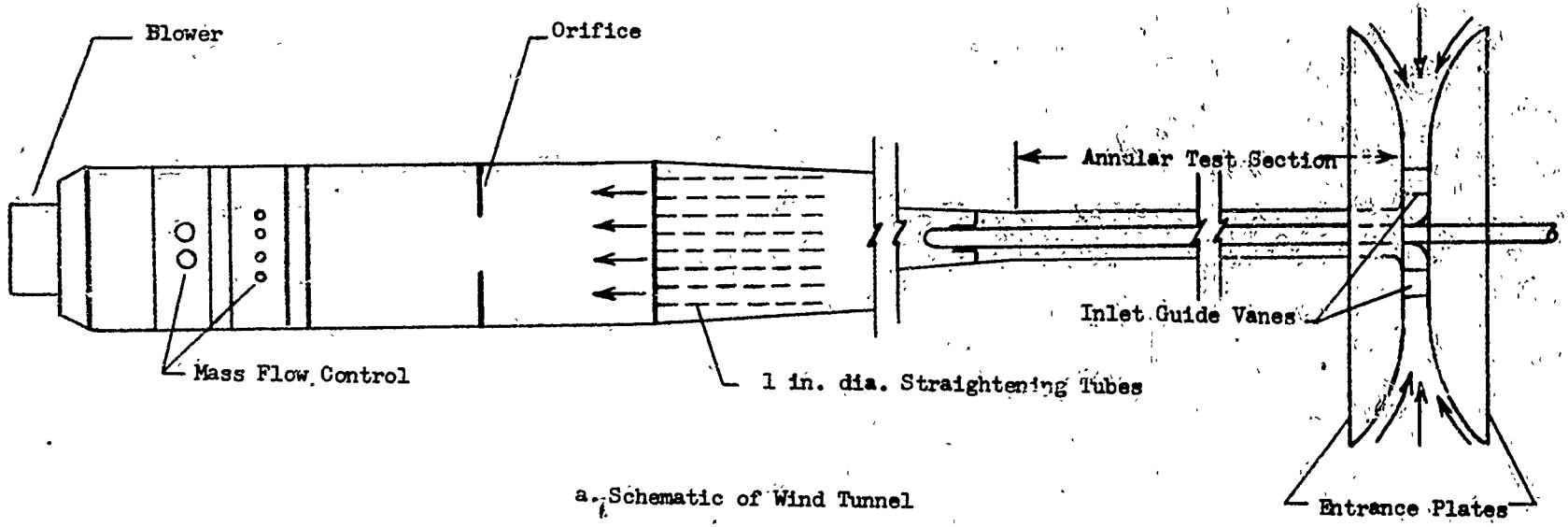

a. Schematic of Wind Tunnel

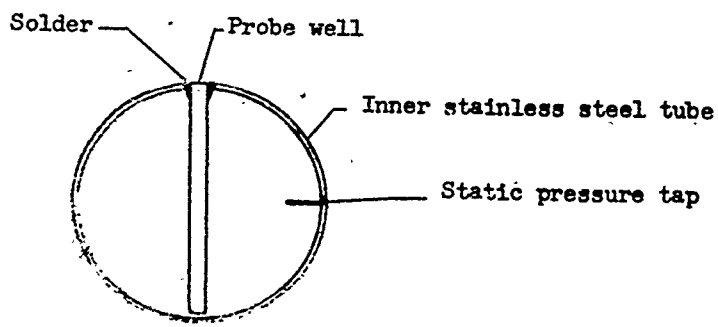

b. Probe Well

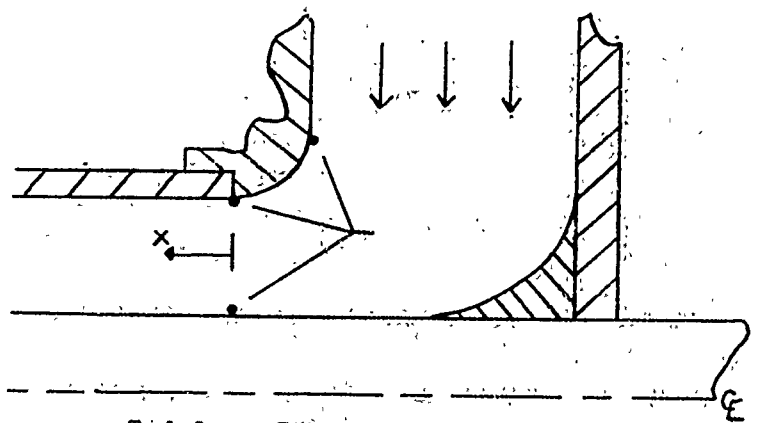

c. Turbulence Trip Locations

Figure 1. Experimental Setup

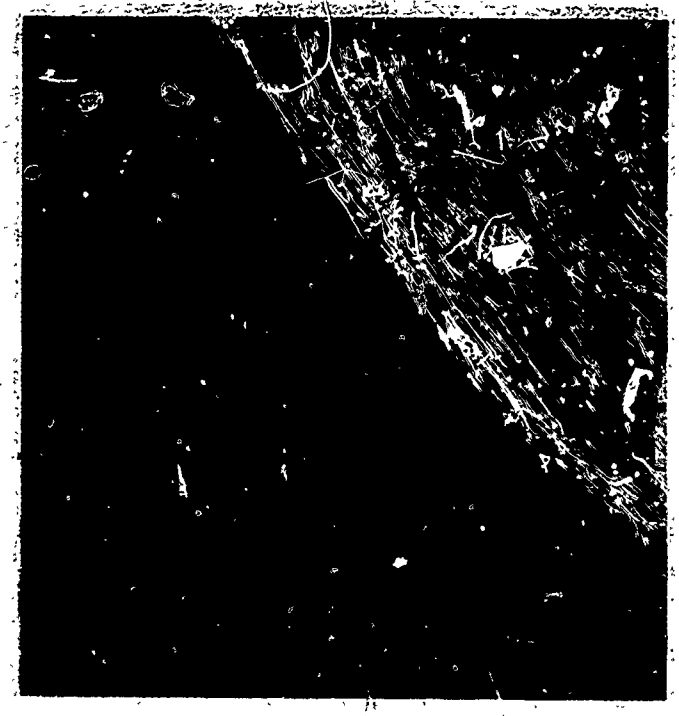

Figure 2 Wind Tunnel

Figure 3 Vortex Generator

Figure 4 Probe Traverse

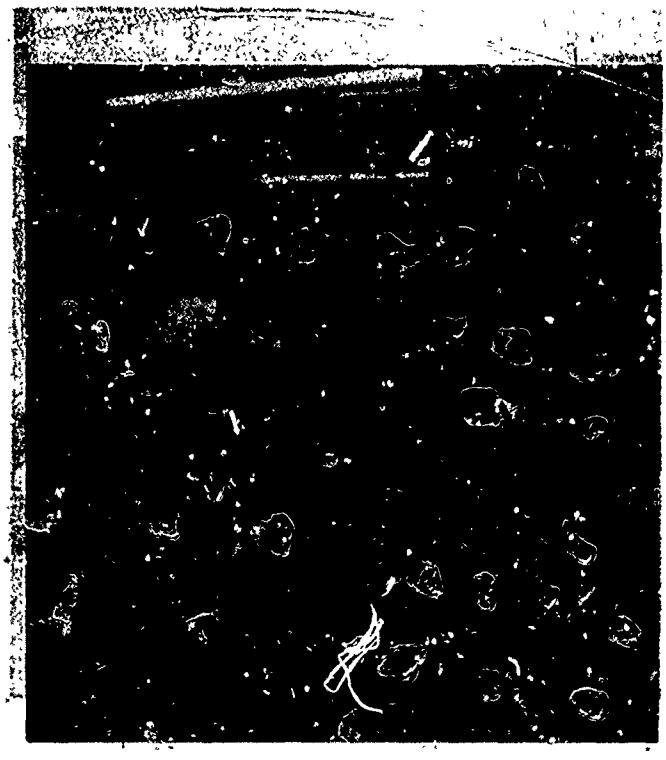

Figure 5 Potentiometer

tunnel. If no retarding forces are present, the moment of momentum is constant as the flow spirals inward and a free vortex type of flow is generated. The actual situation is complicated by the drag of the vanes, the presence of wakes behind the vanes, the sidewall plate drag, and the drag along the inner wall of the annulus within the inlet.

As the flow encounters the 90 degree bend which converts the principal motion into an axial motion, it encounters three, ring-shaped, boundary layer trips (Figure 1c). The trips serve to fix the point of transition from laminar to turbulent flow at the entrance to the annulus, and thereby achieve a steadier gross flow. Olson and Sparrow [52] and Okiishi and Serovy [53] found that in smooth, rounded-entrance annuli, the locus of transition is asymmetric and unsteady. The irregular axial drift of the transition point causes an unsteadiness of the flow which was easily measurable when the trips are removed.

The test section is a concentric, constant-area, annular duct. The outer tube is of clear plexiglass with a 5.0-inch I.D. and 1/4-inch wall thickness. A stainless steel inner tube, 2.00-inch O.D. and 1/16-inch wall thickness is used. The inner tube can be translated axially or removed completely. The overall length of the test section is 118 inches or 39.3 hydraulic diameters.

The inner stainless steel tube is instrumented along a single ray with 29 static pressure taps. Variable flow spiraling prevents repeated roughness effects. Six probe wells, Figure 1b, are located in the inner tube in order to accept the cylindrical pressure survey probe. The probe wells are installed 90 degrees from the static pressure taps and at longitudinal locations midway between two pressure taps.

The conical diffuser commences with the 5-inch diameter plexiglass tube and increases to an 18.4-inch circular cross section. The walls form a total included angle of 7 degrees. Straightening tubes made from mailing tube 1-inch in diameter and 18 inches long fill the diffuser cross section upstream of the

metering orifice. Their primary function is to remove the swirl such that the total channel flow can be accurately measured. The orifice was calibrated by numerically integrating the axial velocity profiles. The calibration was found to be independent of the magnitude of the swirl--demonstrating the effectiveness of the diffuser-straightening-tube-bank combination. The mass flow rate is controlled by means of a low-resistance by-pass. A section of the tunnel, located between the orifice and the blower, has bleed holes in it which can be exposed by means of a rotatable sleeve. By opening the bleed holes, room air can be induced into the system downstream of the orifice--thereby reducing the rate of mass flow through the test section.

The blower used to draw air through the tunnel is powered by a 3 h.p. motor equipped with an adjustable v-belt drive. The blower is isolated from its angle-iron mounting frame by four coil springs and isolated from the annular channel by means of flexible canvas sections.

The cylindrical pressure probe and the hot film probe used to sense the local velocities are each held in identical brass blocks which can be displaced vertically along a dovetail track by a micrometer which is, in turn, secured to the base section of a surveyor's theodolite. Either probe can be rotated a full 360 degrees and the rotation angle determined to within five minutes. The micrometer has a 2-inch travel and is graduated in 0.001-inch increments. Comparisons between Pitot cylinder probe and hot film probe performance are made in Appendix A.

Measurement of the Mean Values of the Local Static and Total Pressures. The radial velocity distribution $\overline{v}$ may be calculated from the continuity equation 5. This relation, written for rotationally symmetric flow with steady mean values, holds without deviating more than a few percent from the complete turbulent equation of continuity. Integrating equation 5 yields

$$rv = -\int_{r_i}^{r} \frac{\partial}{\partial x}(ur)\,dr \tag{15}$$

The radial velocity is identically zero at both the inner and the outer walls. Only near the entrance are axial variations of the axial velocity of significance. The average axial velocity remains constant. Therefore, the radial component of the velocity is everywhere small and the direction of the flow can be described by a single angle ϕ between the total velocity and the axial direction.

In surveying the pressure fields in internal flows with superimposed secondary flows, most investigators have observed that the flow is sensitive to disturbances resulting from the presence of a conventional Pitot probe.[+] These disturbances are minimized when a Pitot cylinder is used which is oriented along a radius and is of sufficient length to span the cross section. The principal design and construction problem of this type of probe is in establishing a known angle between the static holes. The present Pitot cylinder (Fig. 6) was made from 0.083-inch O.D., 0.063-inch I.D. hypodermic tubing. In order to use the probe as a flow direction sensor, two pressure taps, 0.020-inch in diameter, were located 90° apart on the circumference. By locating the pressure taps 45° on either side of the stagnation point (Fig. 7), maximum sensitivity to the flow direction was obtained. Thom [54] demonstrated that the wall pressure sensed in a hole drilled in a cylinder is not the pressure at the center of the hole, rather it is the pressure existing at a point halfway along the hole radius upstream of its' center. Therefore, the correct angle between the centers of the two holes is $2\alpha_{ref} = 2\alpha_{crit} + 180\ d/\pi D$ where α_{crit} is the angular location of the point on the cylinder where the pressure is just equal to the approach flow static pressure and d and D are the diameters of the hole (0.020-inch) and of the cylinder (0.083-inch), respectively.

[+]Static pressure obtained using the static pressure holes of a Pitot tube are usually too low due to the turbulence velocities normal to the tube.

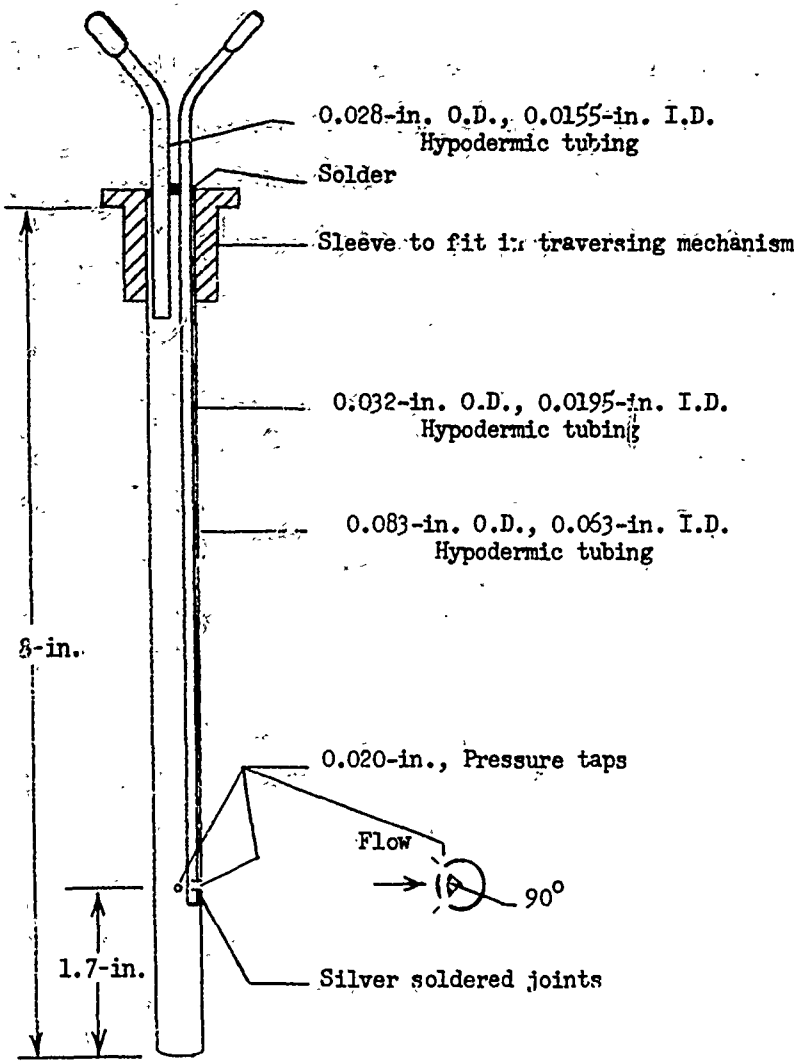

Figure 6. Schematic of Cylindrical Pressure Probe

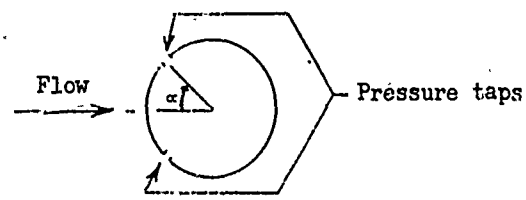

Figure 7. Probe Cross Section Showing Pressure Taps and the Angle α

The potential flow solution for the flow past a circular cylinder in cross flow is given by $u = 2U_\infty \sin \alpha$. Apply Bernoulli's theorem, the pressure is given by $p = p_\infty + \rho(U_\infty^2 - u^2)/2$. The pressure p will equal the undisturbed static pressure when $\alpha = 30°$. Thus, the simplified approach of potential theory gives $\alpha_{crit} = 30°$. From calibrations in steady flow, Glaser [55] found that $\alpha_{crit} = 34.8°$. Thom [54] measured $\alpha_{crit} = 34.2°$ at $Re_D = 8.5 \times 10^3$ and 34.3° at $Re_D = 1.7 \times 10^4$. Using Glaser's result in Thom's equation yields $\alpha_{ref} = 34.8 + (90)(0.020)^2(.083) = 41.7°$ for the present probe geometry.

The slope of the potential flow pressure distribution $(p_\infty - p)/\rho u^2/2$ is 0.05 per degree near a pressure coefficient of zero. Therefore, it is necessary to determine 2α to within 0.4 degrees in order to prevent a systematic error of one percent in $1/2\ \rho u^2$. Since the slope of the static pressure is nearly linear near α_{crit}, a good first approximation to the local static pressure (or flow angle) can be obtained by taking the average pressure of the two holes. In reality an elaborate calibration was required.

The pressure distribution along the forward surface of a long Pitot cylinder varies only slightly when the axis of the cylinder is no longer set perpendicular to the flow. This result was anticipated by Glaser from potential flow theory--that the form of the pressure distribution about an infinite cylinder is independent of the angle between the free flow and the axis of the cylinder. Therefore, the flow can be broken up into components along and normal to the cylinder, the former having little effect on the pressure distribution since the velocity potential has the property of being additive for superimposed flows. In the present experimental situation, the probe is always aligned normal to the local total velocity while the crossflow arises because of the swirl.

Lavan [16] used $\alpha_{ref} = 40°$ and calibrated $P_{ref}(\alpha)/P_{stag.}$ as a function of Mach number. A strong Mach number dependence on the pressure distribution was

observed. Bruun [56] also calibrated a short Pitot cylinder in a free jet (to minimize wall effects). The observed α_{ref} (approximately 45°) was constant for velocities under 100 m/sec. Above 100 m/sec, α_{ref} has increased by about 2°. Finally, Hinze [51] cautions that the diameter of the cylinder must be small, at least not much larger than the microscale of the ambient turbulence.

In order to measure the flow angles directly, the probe was first aligned such that in pure axial flow a flow angle reading of $\phi = 0°$ is obtained. Values of α_{ref} were obtained by rotating the pressure probe until the indicated static pressure agreed with that measured using a static wall tap located in the inner tube at the same axial (x/D_h) location. Sample calibrations performed in straight flow at three values of x/D_h are given in Fig. 8. α_{ref} variations of $\pm 1/2°$ are observed at a fixed radial location. In actual practice, each α_{ref} profile was plotted on a larger scale and a smooth curve drawn through the data. α_{ref} profiles at intermediate values of x/D_h were obtained from interpolation of the calibration profiles.

Laufer [57] has suggested that in the vicinity of the wall, velocity correction should be made because of the large local turbulent intensities. If U is the total velocity, he suggests using

$$U_{corr} = U_{meas} \sqrt{1 - \frac{\overline{u'^2} + \overline{v'^2} + \overline{w'^2}}{U^2}} \qquad (16)$$

For normal turbulence intensities, the correction is of the order of five percent or less. Corrections were not made to the present data because turbulence intensities were not measured.

EXPERIMENTAL PROCEDURE

One of the primary objectives of this study was to obtain velocity profiles at various axial stations (D_h locations) using different swirl rates (inlet vane settings). Velocity surveys were obtained at stations 3, 7, 11, 15, 19, 24, and

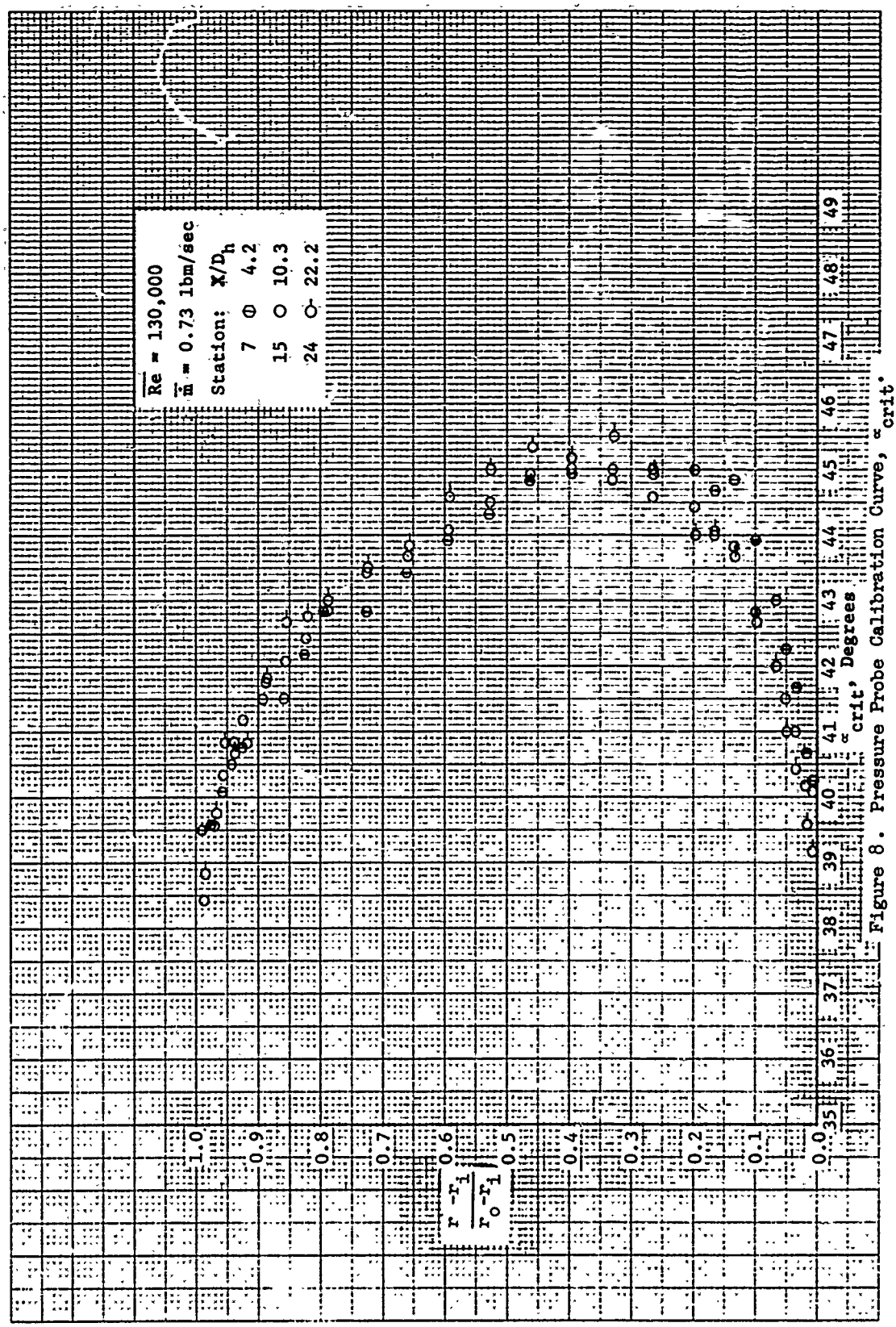

Figure 8. Pressure Probe Calibration Curve, α_{crit}

28 (x/D_h values of 1.7, 4.2, 7.0, 10.3, 14.8, 22.2, and 32.7) for nominal inlet vane settings of 0°, 10°, 30°, 45°, and 60°. The bulk of the data involved local measurements of the flow angle, the total pressure, the static pressure, and the static temperature of the flow. All of these quantities are needed to obtain the local velocity components at a single point. The first readings were always taken at a radial distance of 0.010-inch from the inner tube wall. In all, readings were taken at thirty different radial locations which spanned the annular gap. At any given r-location, the flow angle was determined first by using the manometer setup as a U-tube manometer and rotating the probe until a null reading was obtained. The flow angle was read, to the nearest five minutes, directly from the scale on the base of the traversing mechanism. Once the flow angle had been determined, the probe could be turned to the proper angles for measuring the total and static pressure. All velocity measurements were made at sufficiently low velocities (less than 200 ft/sec) that compressibility effects could be neglected.

The axial and tangential velocity components were calculated from the total velocity vector using the relations

$$u = V \cos \phi \tag{17}$$

and

$$w = V \sin \phi \tag{18}$$

where

ϕ = flow angle

u = axial velocity

w = tangential velocity

A sketch showing the relative position of the total velocity vector and the flow angle ϕ is shown in Fig. 9.

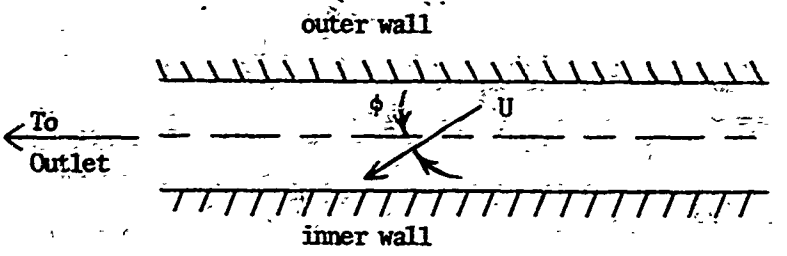

Fig. 9
Sketch Showing Flow Angle ϕ

The mass flow rate was determined by numerically integrating the axial velocity profiles. Recall that with swirl, the orifice was never calibrated directly to obtain the mass flow rate. The mass flow rate is given by the following integral

$$\dot{m} = 2\Pi \int_{r_i}^{r_o} \rho u r dr \tag{19}$$

The numerical integration was carried out in the following manner. A least squares, second-degree, polynomial was fit through the first four data points, with the first point now being taken as the zero velocity point at the inner wall. The least squares fit was of the form $ur = C_1 + C_2 r + C_3 r^2$. This polynomial was then integrated between the wall and the third data point, thus giving the mass flow rate through that interval as

$$\dot{m}_1 = 2\Pi\rho\{C_1[r(3) - r_1] + C_2/2[r(3)^2 - r_1^2] + C_3/3[r(3)^3 - r_1^3]\} \tag{20}$$

The local density used was the average of the densities at the points over which the integration was performed. Away from the inner wall, a set of five points was used for the least squares fit and the integration was carried out between the second and third point of the five-point set. The first point of each set was the same as the second point of the previous set. At the outer wall, the fit was again through four points and the integration was carried out over two intevals.

The radial velocity gradients were also calculated at each point. Essentially, the same technique was used to differentiate the velocity profiles as was used to integrate them. Instead of integrating a fitted least squares polynomial, a differentiation was required. For example, the least squares polynomial fitted to the axial data was of the form $u = C_1 + C_2 \cdot y + C_3 \cdot y^2$, where y is equal to the radial distance measured from inner wall $(r - r_i)$.

The velocity gradient was evaluated at the center point of each five-point fit. At each wall, a four-point fit was used and the gradient was evaluated at the wall and the next two points.

DISCUSSION OF RESULTS

Axial Velocity Profiles. The extreme axial velocity profiles, presented in Figs. 10 and 11, were plotted at the initial and final axial location with inlet vane angle as the parameter. A somewhat unexpected profile exists at station 3 (Fig. 10). For zero swirl, the axial velocity profiles have a nearly fully-developed characteristic shape although located quite close to the entrance ($x/D_h = 1.7$) where centrally flat profiles were expected. It appears that the friction drag of the entrance plates, coupled with the profile drag of the turbulence trips, has strongly retarded the flow near both walls, thereby producing the more rounded velocity profiles characteristic of fully developed turbulent annular flows. Further downstream, the calculated average axial velocities of the $\overline{\phi} = 0° \rightarrow 45°$ data are constant to within ±3 percent, while the $\overline{\phi} = 60°$ profiles seem to have changed considerably in comparison with the other profiles.

The axial flow field is most sensitive to inlet vane angle $\overline{\phi}$ greater than 45°. For $\overline{\phi} = 60°$ in the inlet region, the flow is approaching a reversed flow condition, (axial velocity near the inner wall moving in the negative x-direction), which explains the skewed nature of the 60° profile. Since the inner flow is

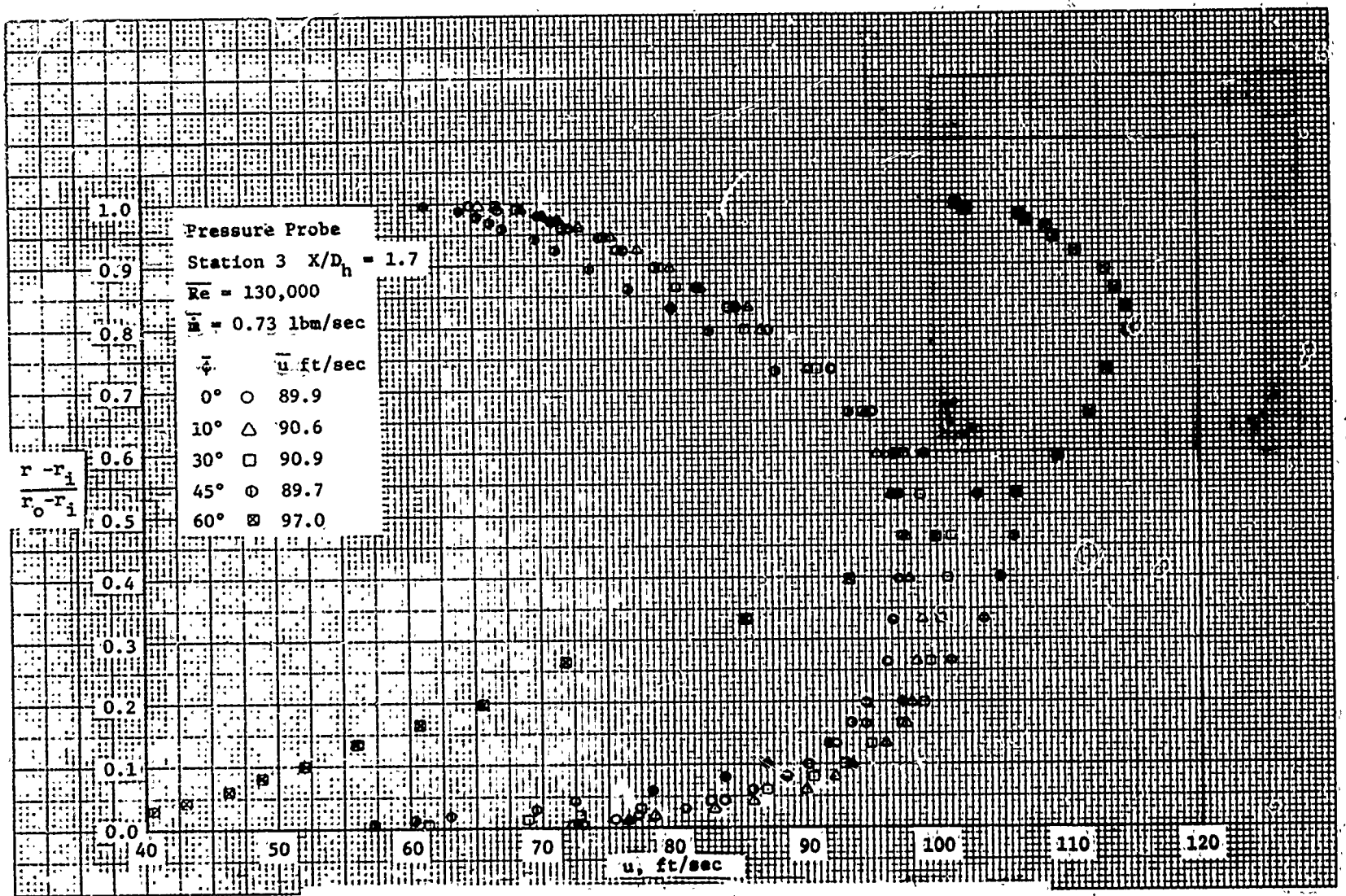

Figure 10. Axial Velocity Profiles. Pressure Probe, Station 3.

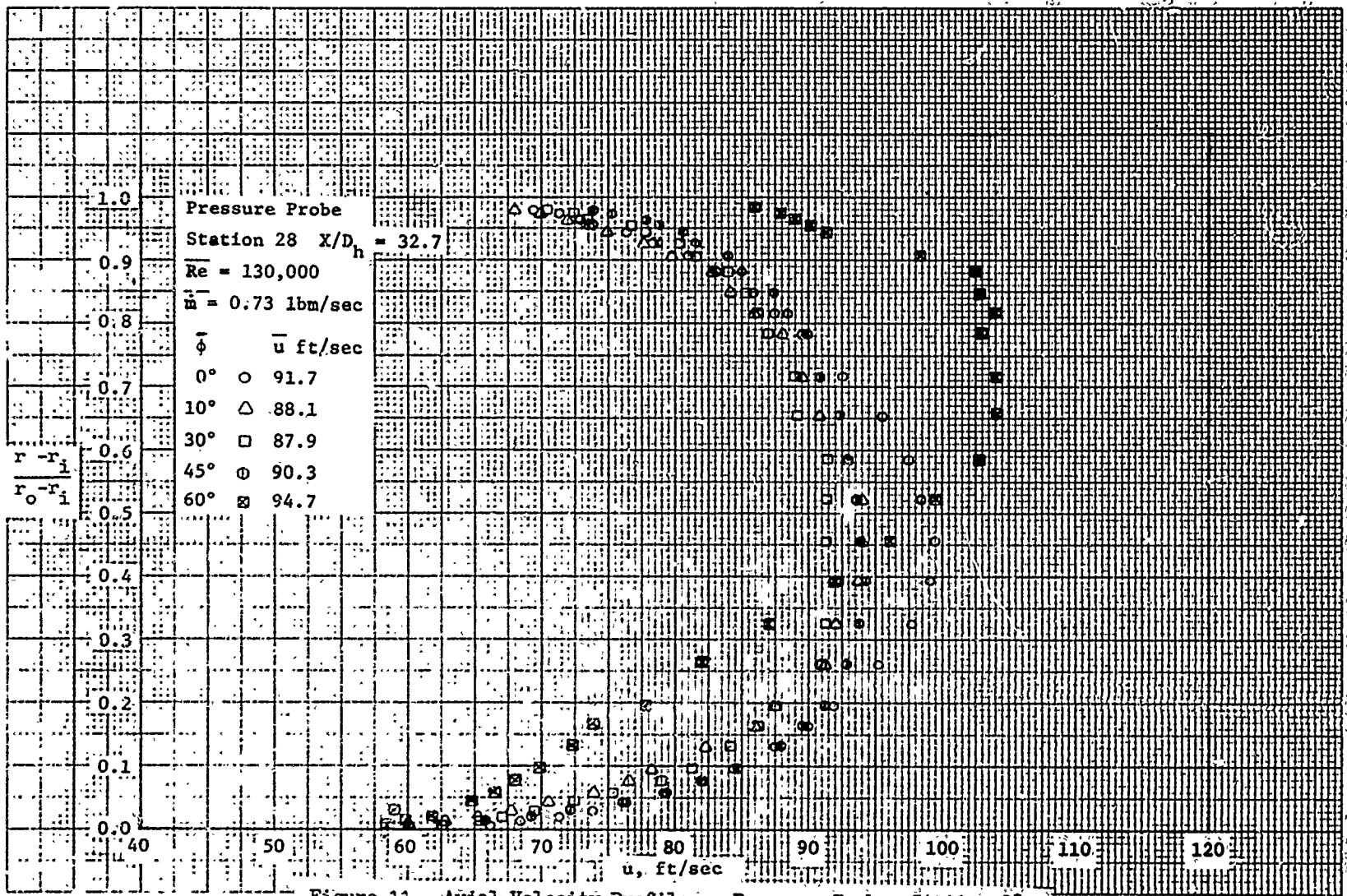

Figure 11. Axial Velocity Profiles. Pressure Probe, Station 28.

retarded, the outer flow must be accelerated to a larger than normal velocity to compensate. Flow reversal did occur at an inlet vane setting of approximately $\bar{\phi} = 65°$ in agreement with the calculations of Bossel [4]. The $\bar{\phi} = 60°$ profiles developed in a regular manner, becoming flatter and fuller as one moves downstream. This data exhibited more unsteadiness and larger than normal scatter resulted.

For straight flow, the maximum axial velocity at station 3 is located at a dimensionless radial position $(r_m - r_i)/(r_o - r_i)$ of about 0.46. Downstream of station 3 the velocity maximum first moves closer to the inner wall and then outward to a final value of 0.45 at station 28. For $\bar{\phi} = 10°$, the maximum location begins at 0.37 at station 3, moves inward and then outward until at station 28 it occurs at $\Delta r_m/\Delta r_o = 0.50$. The same trends are noted for $\bar{\phi} = 30°$ and $\bar{\phi} = 45°$. The values reported are only approximate since they were obtained by visual inspection of the graphs, while the irregularities in the location of the maximum velocity are clearly observed. For $\bar{\phi} = 60°$, the maximum velocity occurs much closer to the outer wall. At station 3, the maximum occurs at a dimensionless radius of approximately 0.8 and does not vary from this location as the flow proceeds downstream.

Tangential Velocity Profiles. The tangential velocity profiles obtained using the pressure probe are plotted for each inlet vane setting with the station, i.e., dimensionless axial location, x/D_h, as the parameter. The axial decay of the tangential velocity component can be readily observed by plotting the profiles in this manner. The profiles will be discussed starting with those for $\bar{\phi} = 10°$, Fig. 12.

One obvious characteristic of the profiles is the existence of two relative maximum points for over half of the profiles at $\bar{\phi} = 10°$. The swirl is also relatively weak with the absolute maximum tangential velocity at station 3 being

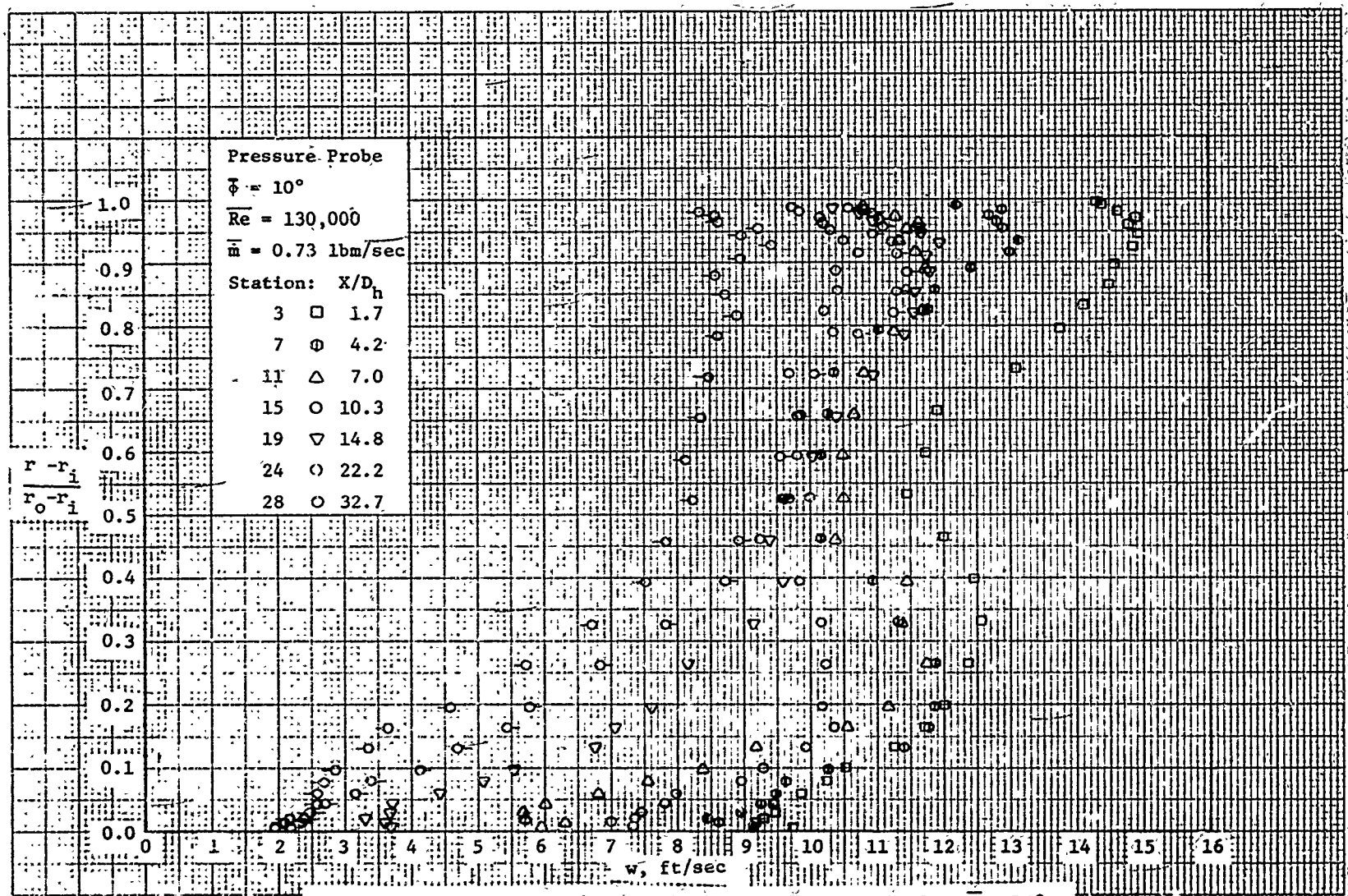

Figure 12. Tangential Velocity Profiles. Pressure Probe, $\bar{\phi}$ = 10°.

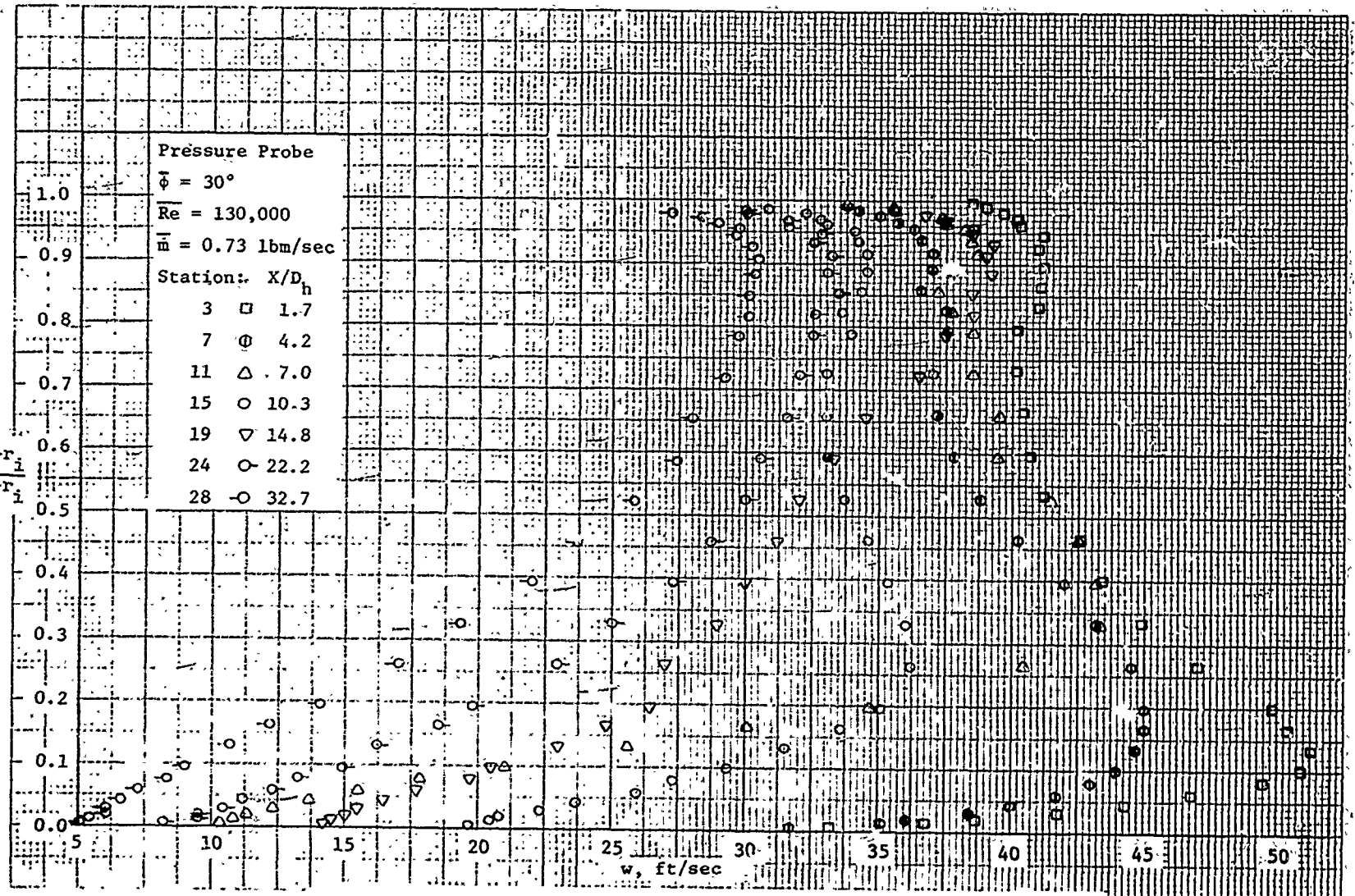

Figure 13. Tangential Velocity Profiles. Pressure Probe, $\bar{\phi}$ = 30°.

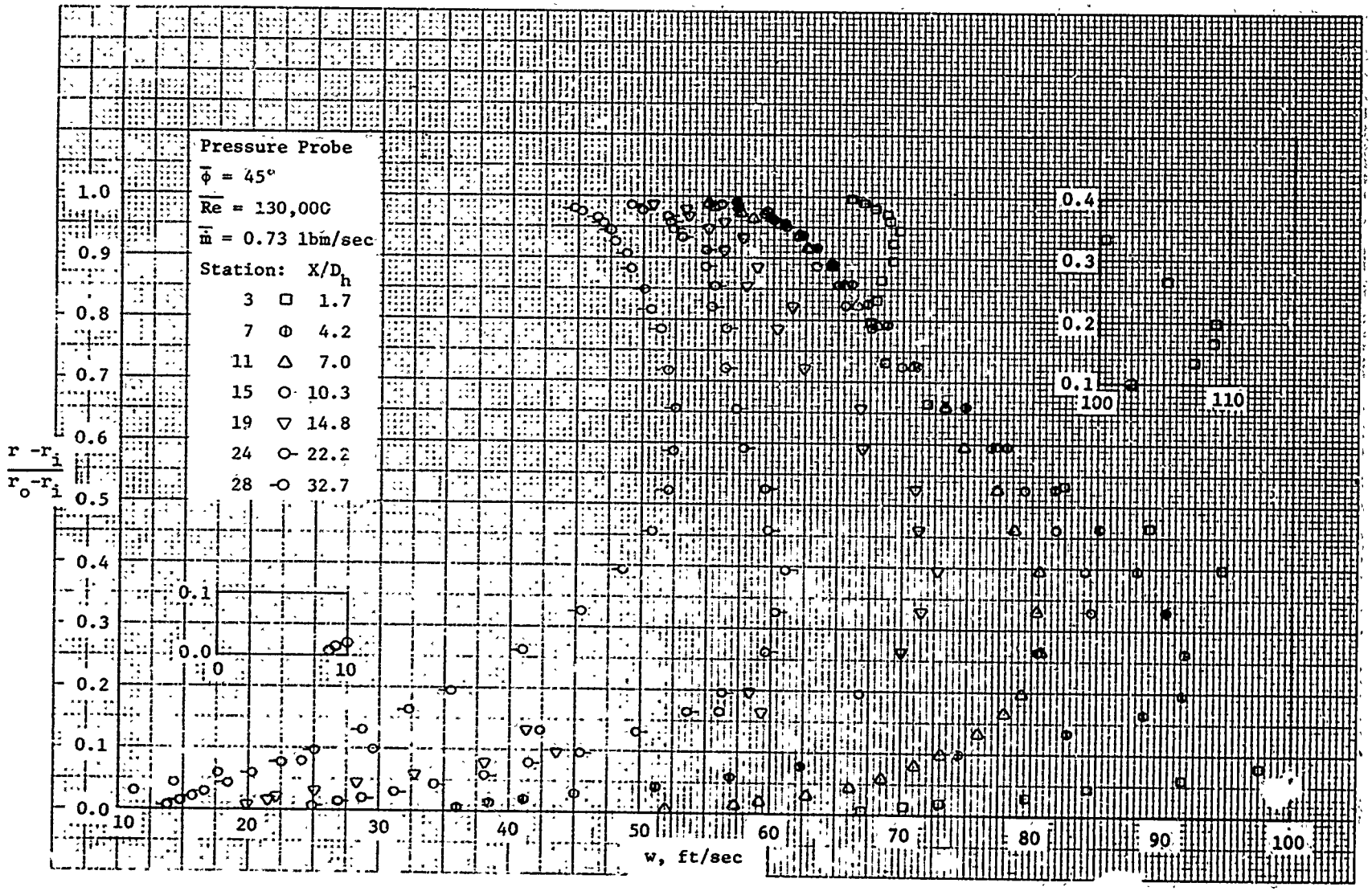

Figure 14. Tangential Velocity Profiles. Pressure Probe, $\overline{\phi}$ = 45°

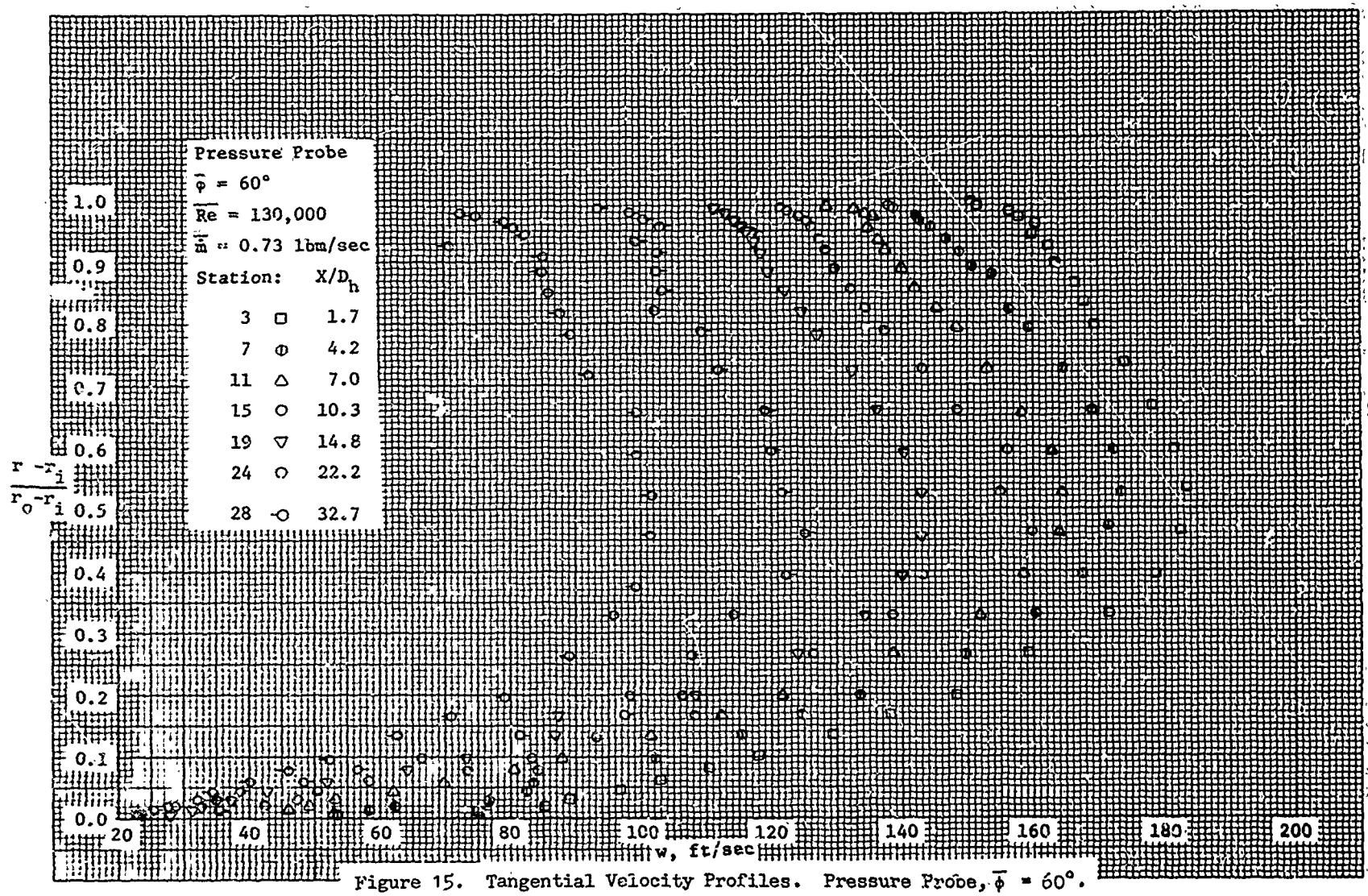

Figure 15. Tangential Velocity Profiles. Pressure Probe, $\bar{\phi}$ = 60°.

only 15% of the corresponding maximum axial velocity. The absolute maximum of each profile occurs close to the outer wall, i.e., at a dimensionless radial position of 0.9. The smaller relative maximum points, when they occur, are near to the inner wall (around 0.3). Further downstream, the existence of the two relative maximum points becomes less apparent, until at station 24 only one maximum point is found.

The flow adjacent to the inner boundary layer is similar to a solid body rotation (forced vortex type) as is evident at stations 24 and 28. Closer to the inlet the forced vortex flow gradually reverts to a free vortex form which extends outward toward the outer wall. Adjacent to the outer wall the flow reverts back to the forced vortex form, and produces the double maximum.

At $\overline{\phi}$ = 30°, the maximum tangential velocity at station 3 is nominally 50% of the maximum axial velocity. The existence of two relative maximum points is noted only at stations 3, 7, 11, and 15. At station 3 the absolute maximum point is at a $\Delta r_m/\Delta r_o$ of 0.13. The maximum points at stations 7, 11, and 15 are again close to the outer wall. One now observes that at station 3 the majority of the flow is of a free vortex type. At $\overline{\phi}$ = 30° the vortex generator is operating as planned. It is of interest to note the rapid change from essentially a free vortex type in the outer 2/3 of the annulus at station 15, to a completely forced vortex type at station 19. The forced vortex pattern is even more evident at stations 24 and 28.

At $\overline{\phi}$ = 45°, Fig 14, the maximum tangential velocity is now more than twice that observed at $\overline{\phi}$ = 30°. The maximum tangential velocity at station 3 is 103% of the corresponding maximum axial velocity. The profile at station 3 is the only one that exhibits two relative maximum points. All of the maximum points occur within the inner half of the annulus except at station 28 where the maximum occurs at a dimensionless position of about 0.62. All of the profiles

exhibit a free vortex type of flow over a major portion of the annular flow region and the free vortex nature is still preserved at station 28. The free vortex produced by the inlet guide vanes is becoming stronger, i.e., a larger total angular momentum is initially produced and is making its presence felt over the entire length of the test section. The forced vortex type of flow is still evident close to the inner wall and it moves out until at station 28 the flow in the inner half of the annulus has a forced vortex character.

At $\overline{\phi}$ = 60°, Fig. 15, the maximum tangential velocity at station 3 is now approximately 160% of the corresponding maximum axial velocity. No double-maximum profiles occur. All of the profiles now exhibit a maximum point at a dimensionless position (within 10%) of 0.5, with the maximum at station 28 being closer to the inner wall than the maximum at station 3. The annular flow region is thus approximately divided in half with the inner half exhibiting forced vortex flow and the outer half exhibiting free vortex flow.

To summarize, the tangential velocity curves for each inlet vane setting reveal the following regions:

1) Inner wall boundary layer produced by the no-slip boundary condition at the inner, impermeable wall, i.e., at $r = r_i$, $u = v = w = 0$, $dw/dr > 0$.
2) Forced vortex zone. The region above the slight discontinuity in shape of the swirl velocity profile. The tangential velocity increases with increasing radius according to the approximate relation $w = \text{const } r^m$, $0 < m \leq 1$ and the constant is a function of axial position x.
3) Transition zone. The region brackets the location of maximum tangential velocity.
4) Free vortex zone. The tangential velocity is described by approximate relation $w = \text{const } r^m$, $-1 \leq m \leq 0$.
5) Outer wall boundary layer occurs in the region adjacent to the outer wall. The swirl velocity gradient is negative and at $r = r_o$, $u = v = w = 0$.

The static pressure distributions along the inner wall are presented in Fig. 16. Since atmospheric pressure (P_{atm}) exists at the inlet, all of the measured pressures are subatmospheric. The pressure differences at $x/D_h = 0$ represent the entrance pressure losses and are due primarily to vortex generator friction. The flow cross sections within the vortex generator become quite small at $\bar{\phi} = 60°$. The airfoil sections nearly overlap. The average velocity within the vortex generator increases sharply.

The slope of the profiles is given by

$$\frac{\partial (P_{atm} - P)}{\partial\, x/D_h} = -D_h \frac{\partial p}{\partial x} \tag{21}$$

The normal behavior of a decreasing static pressure with axial distance is observed for $\bar{\phi} = 0°$, 10°, and 30°. An extensive region of nearly uniform pressure is observed in the region $6 < x/D_h < 22$ for $\bar{\phi} = 45°$. The internal wall pressure gradient is positive over the entire test length for $\bar{\phi} = 60°$. Therefore, the normal physical feeling that there can be no extensive regions of flow against a pressure gradient is clearly not true in rotating flow systems.

Further Data Reduction and Tests. More extensive discussion of the $\bar{\phi} = 45°$ data will be presented here because this data represents the results of an intermediate swirl. The axial velocity, flow angle, tangential velocity, and angular momentum profiles are given in Figs. 17, 18, 19, and 20, respectively.

Local Skin-Friction Coefficient. Local axial skin-friction coefficients were computed for both inner and outer walls. The universal velocity-distribution equation for turbulent boundary layer flow has the form

$$u^+ = A \cdot \log\ y^+ + B \tag{22}$$

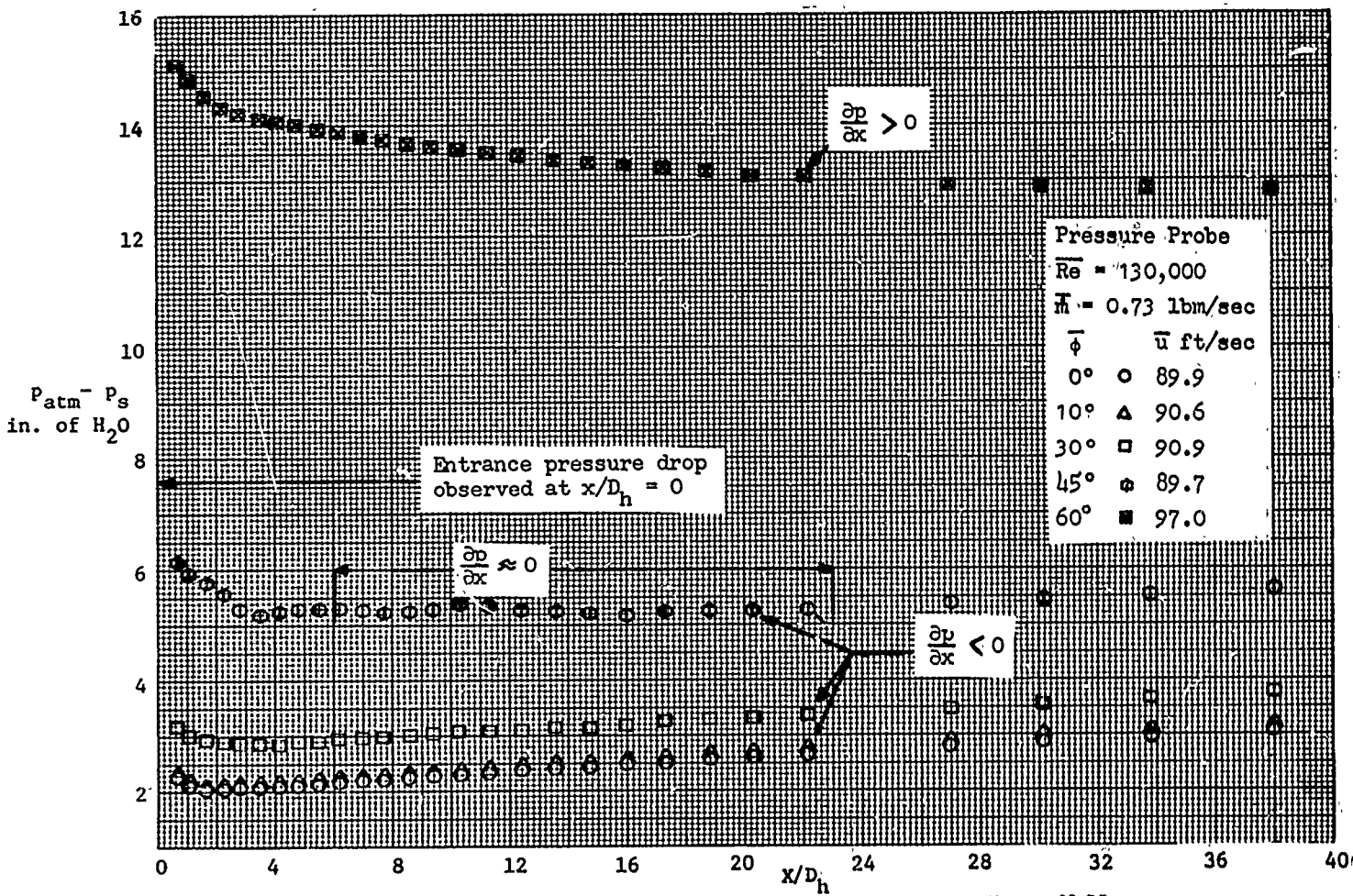

Figure 16. Static Pressure Distribution Along Inner Wall.

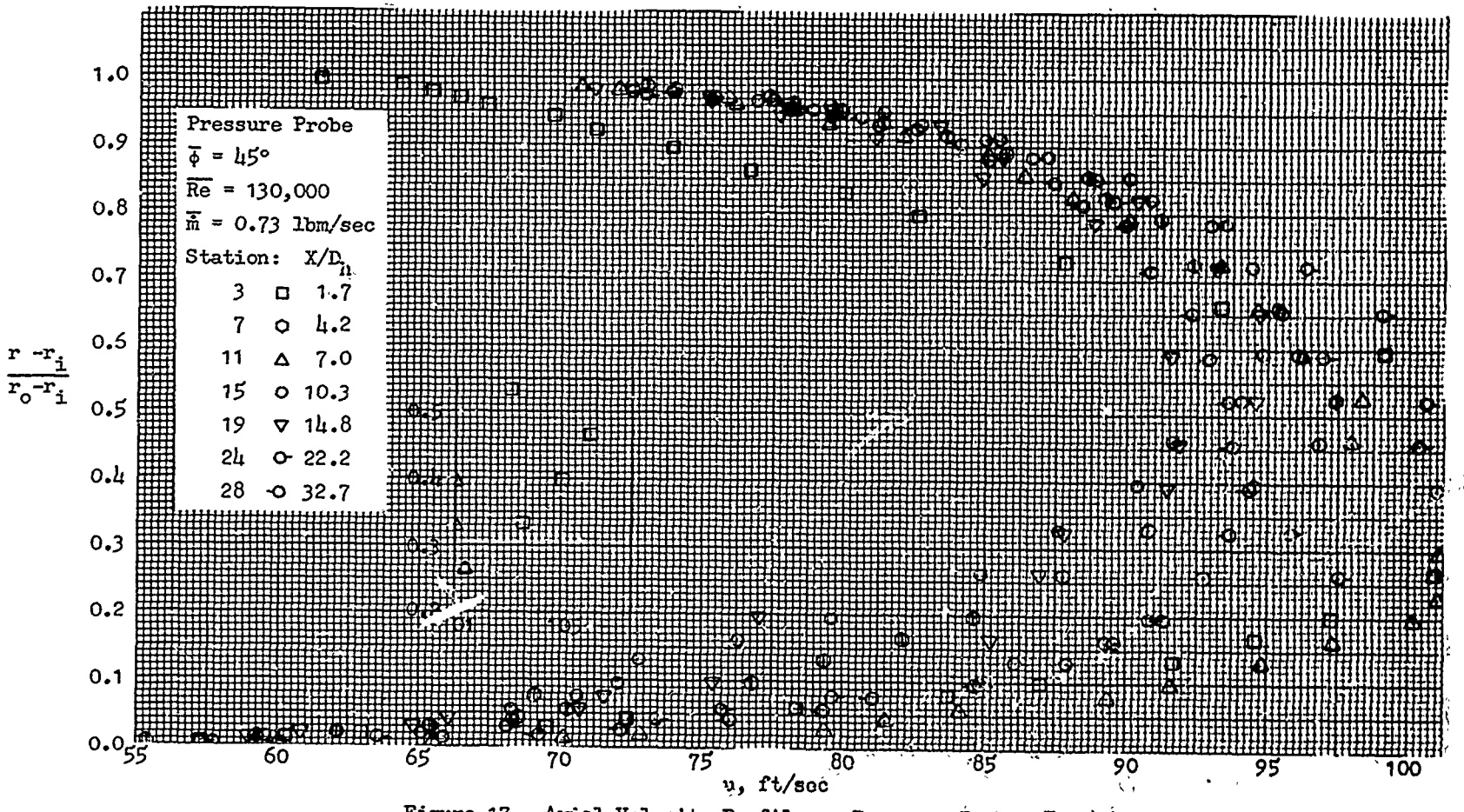

Figure 17. Axial Velocity Profiles. Pressure Probe, $\bar{\phi}$ = 45°.

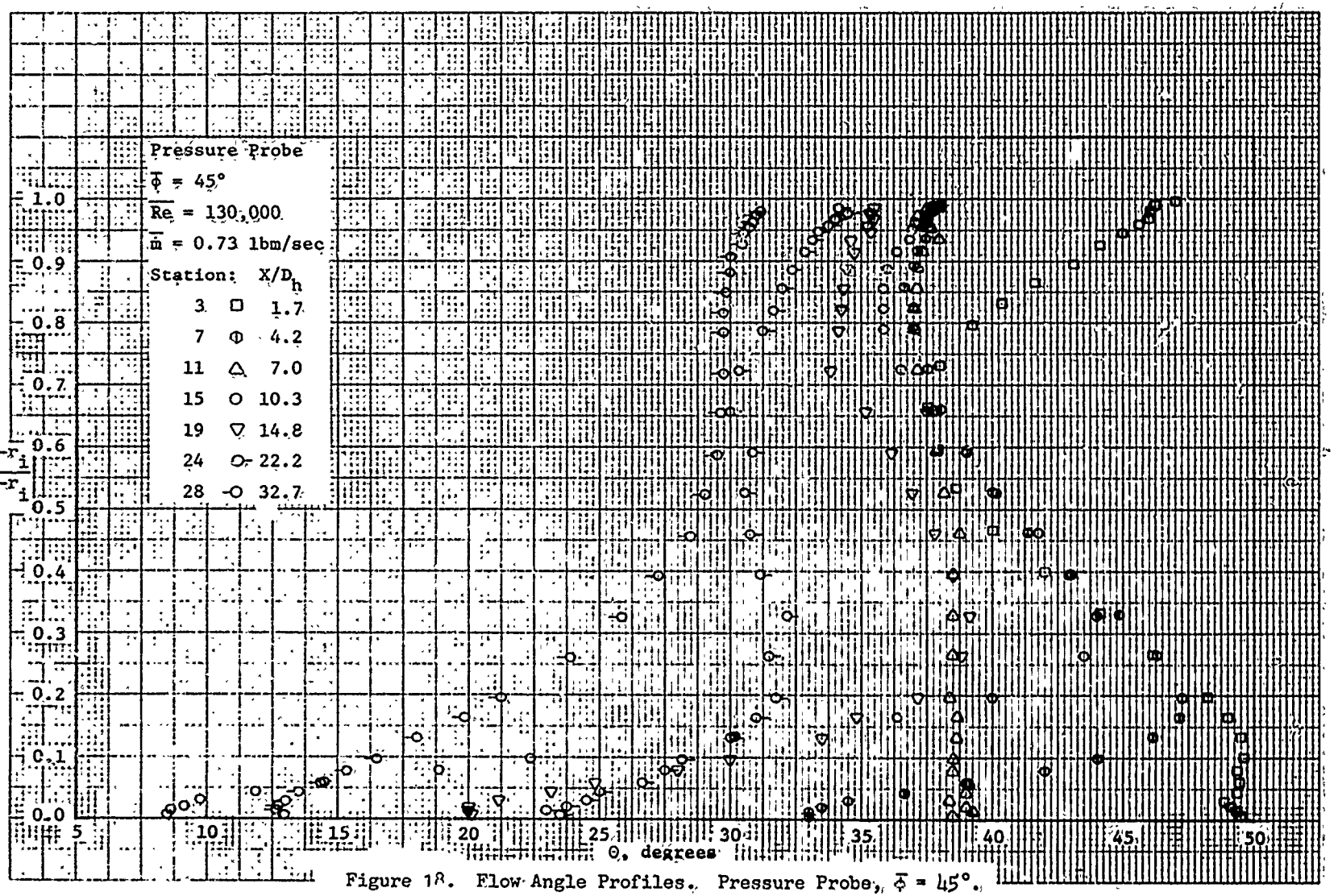

Figure 18. Flow Angle Profiles. Pressure Probe, $\bar{\Phi}$ = 45°.

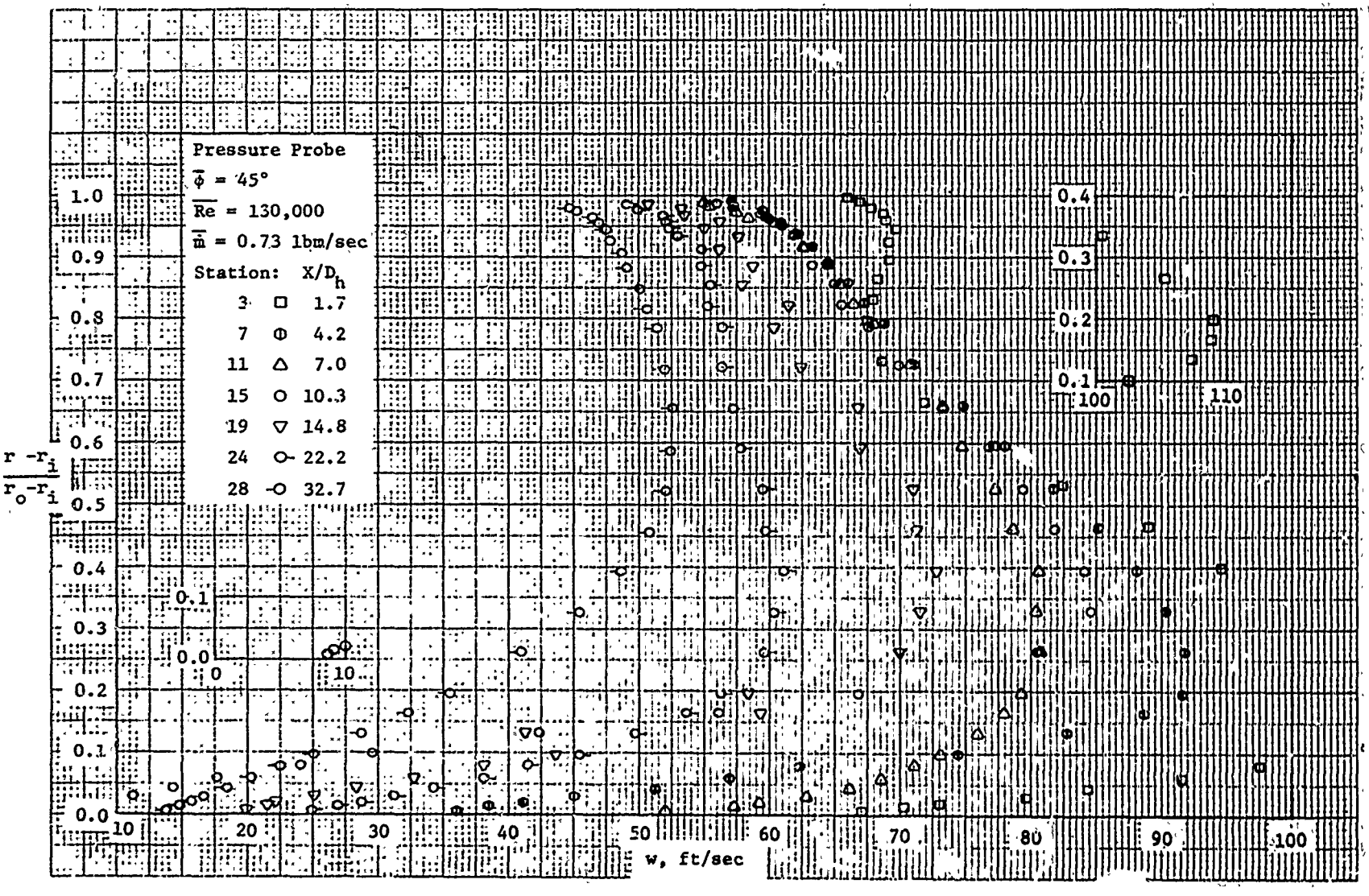

Figure 19. Tangential Velocity Profiles. Pressure Probe, $\overline{\phi}$ = 45°

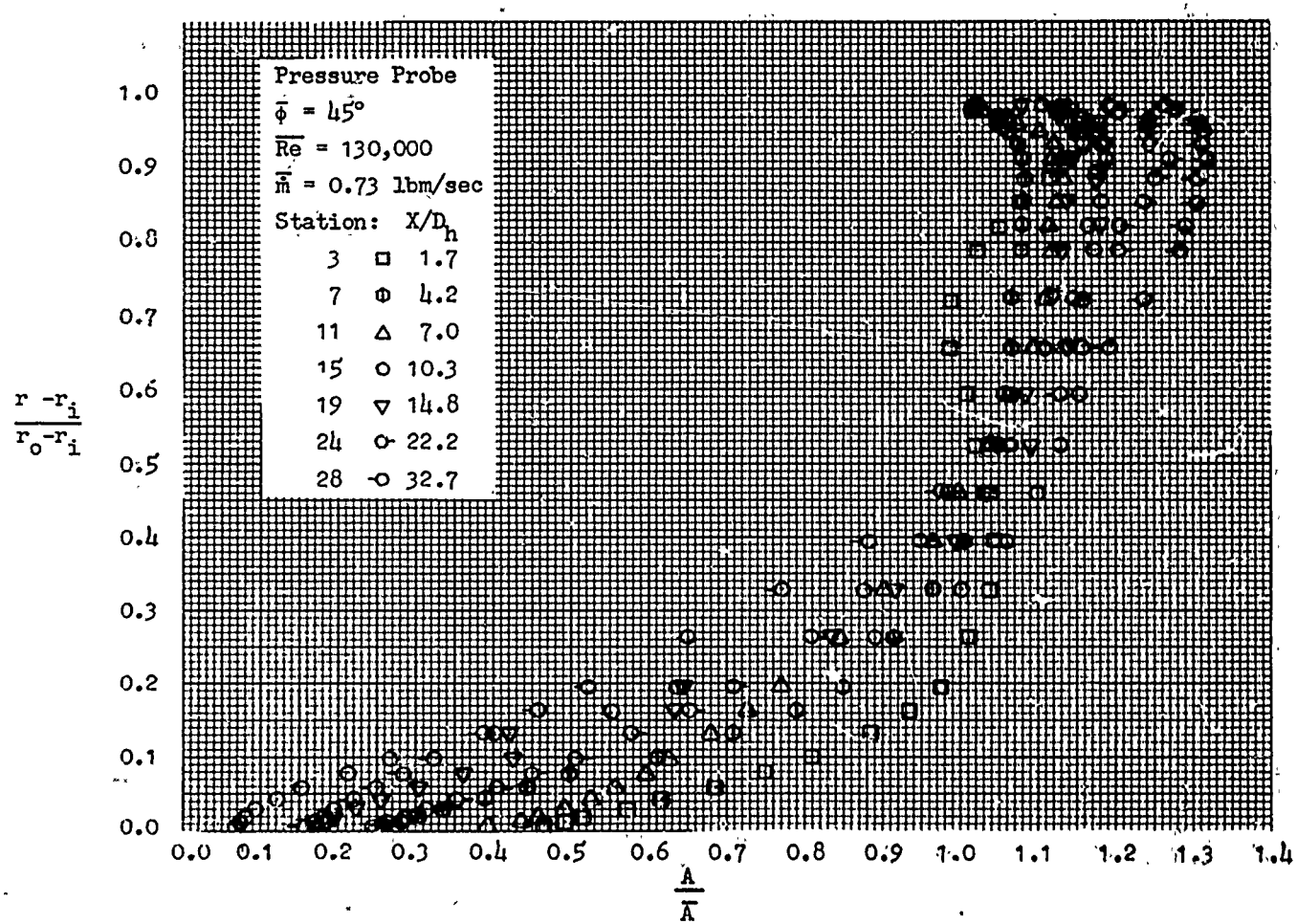

Figure 20. Angular Momentum Profiles. Pressure Probe, $\bar{\phi}$ = 45°.

where

$$u^+ = u/u^* \tag{23}$$

$$y^+ = y \cdot u^*/\nu \tag{24}$$

The values of the law of the wall constants A and B vary somewhat as is observed in the following table.

Table I. Law of Wall Constants

Source	A	B
Nikuradse	5.5	5.8
Clauser	5.6	4.4
Coles	5.62	5.0
Smith and Walker	5.0	7.15
Patel	5.5	5.45
NPL Staff	4.9	5.9

B assumes different values for roughness as summarized in [58]. Brighton and Jones [59] have carried out careful experiments in annuli with several radius ratios. They find the values of u^+ generally lie close to the distribution of Nikuradse [58] for the outer profile, as do the results of Knudsen and Katz [60]. The inner profile results for $r_i/r_o = 0.56$ agree better with the Clauser constants.

Similarity considerations by Eskinazi and Yeh [11] describe deviations from the universal law for smooth walls due to the radius of curvature of the channel. For convex walls (inner wall) the velocities are larger than predicted by equation 22, whereas for concave (outer walls) the velocities are less than predicted by the straight-wall universal law.

The values of A and B used herein were those of Nikuradse. Using these constants, the equation 22 represents the turbulent core region, i.e., $y^+ > 30$.

Making use of the fact that

$$u^*/u_1 = (C_{fx}/2)^{1/2} \tag{25}$$

where

$$u^* = \sqrt{\tau_{w_i}/\rho} \; ; \text{ axial shear stress velocity, ft/sec} \tag{26}$$

u_1 = axial velocity at outer edge of inner axial boundary layer, ft/sec. (In this case, it is also equal to the maximum axial velocity.)

$C_{fx} = \tau_{w_i}/\frac{1}{2}\rho u_1^2$; local axial skin-friction coefficient at inner wall

Equation 22 can be rewritten

$$u/u_1 = (C_{fx}/2)^{1/2} \left[2.5 \ln (y \cdot u_1/\nu) + 2.5 \ln (C_{fx}/2)^{1/2} + 5.5\right] \tag{27}$$

Thus, this equation gives a curve of u/u_1 versus $y \cdot u_1/\nu$ for each value of the parameter C_{fx} (see Fig. 21). As suggested by Clauser [61], values of C_{fx} may now be estimated by plotting the experimental values of u/u_1 versus $y \cdot u_1/\nu$ and selecting the C_{fx} value that best fits the data. Equation 27 was plotted on semi-log paper so that curves of constant C_{fx} would plot as straight lines.

The values of u_1 needed to determine C_{fx} were determined from the appropriate axial velocity profiles. For the axial velocity profiles, the value of u_1 was the same as the maximum axial velocity.

Pierce [62] has given a good discussion of a Clauser plot as applied to a skewed boundary layer flow. At least four variations of the conventional Clauser plot are possible for a three-dimensional turbulent flow. He compares experimental results of pressure driven skewed turbulent boundary layer flows using calibrated Preston tubes [63], Clauser plots, claw Preston tubes, a direct force balance system, and a wall heat meter. Pierce concluded from accumulated

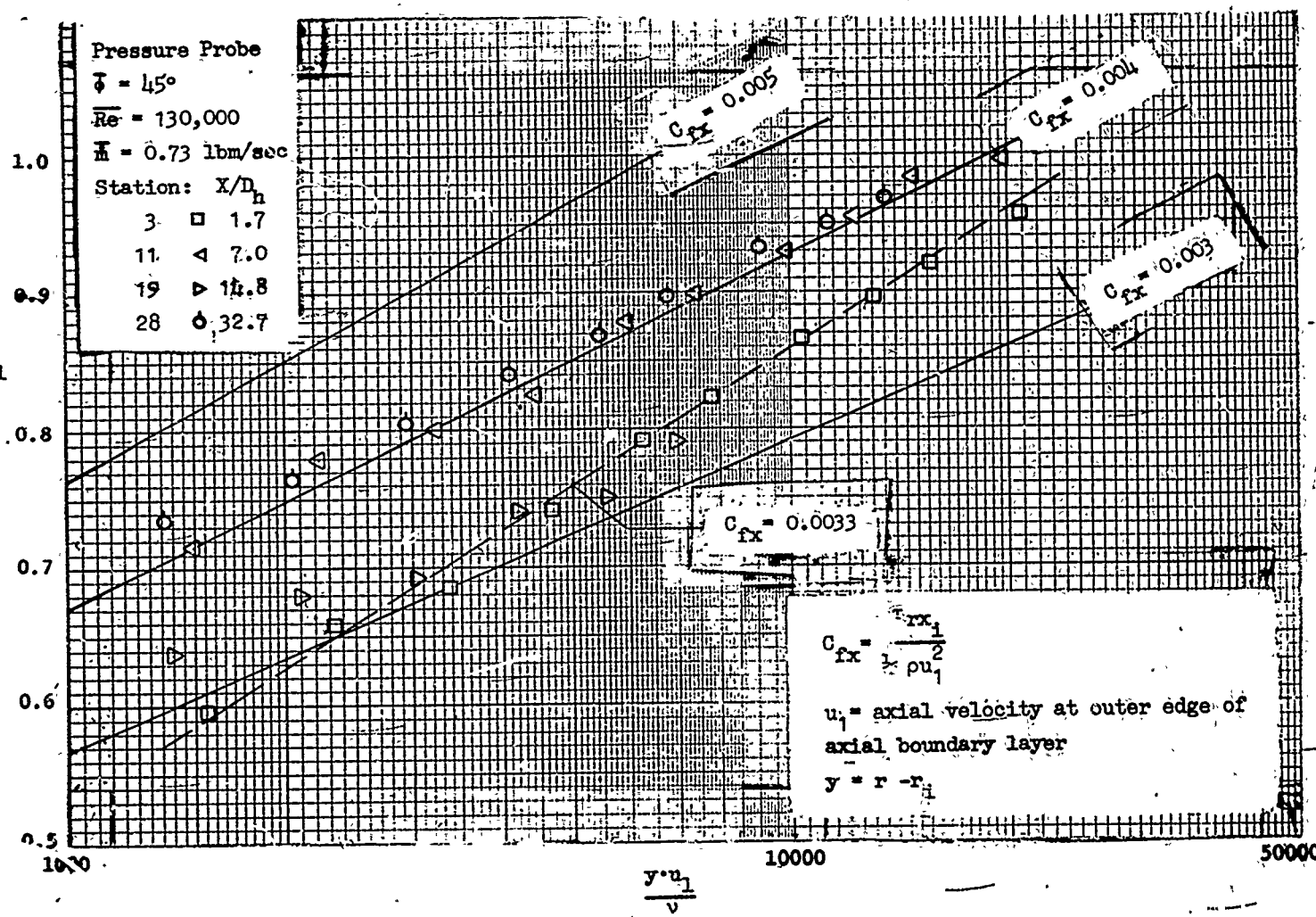

Figure 21. Clauser Chart--Inner Wall.

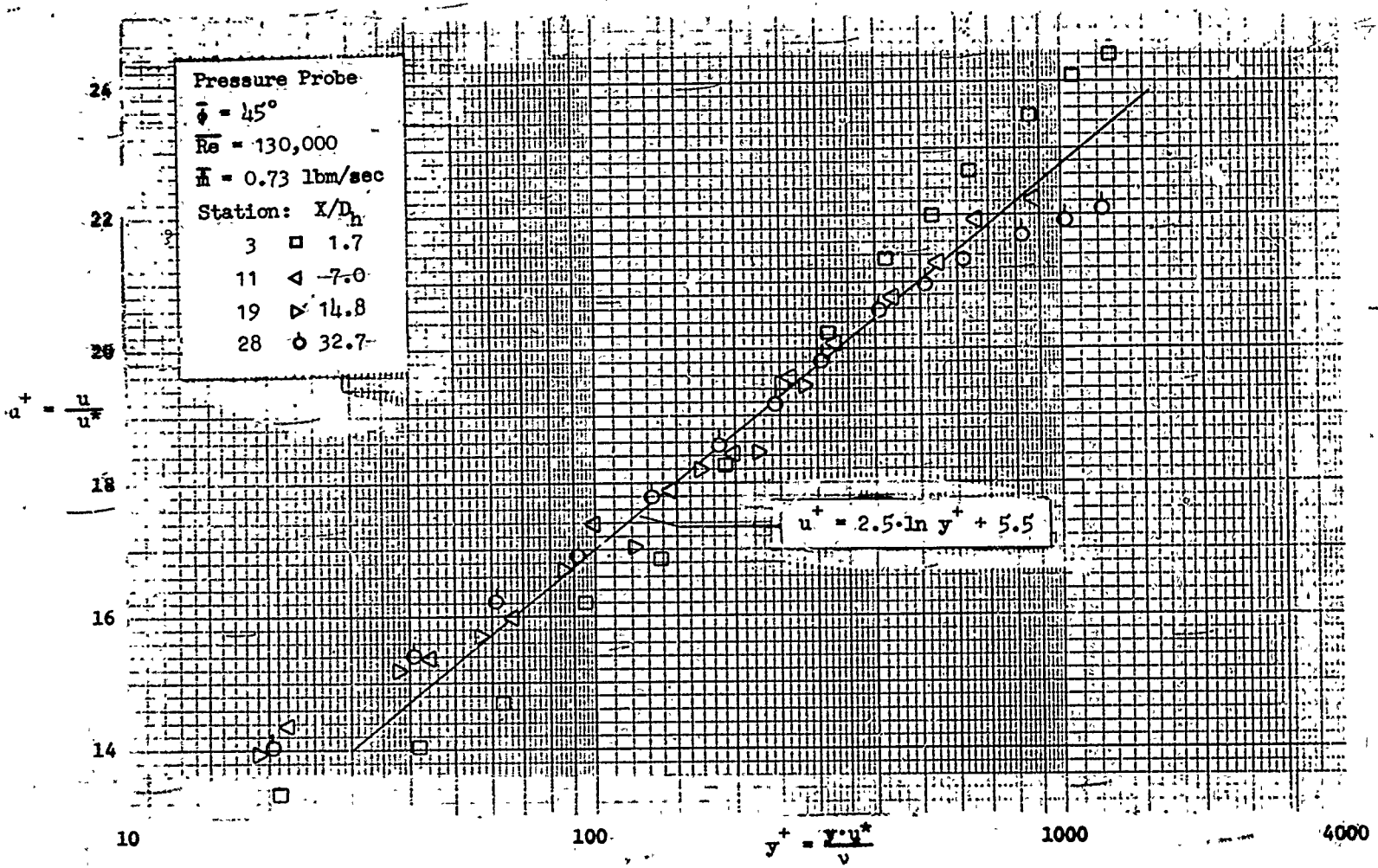

Figure 22. Universal Velocity Distribution--Inner Profile.

data that the Clauser chart described above should predict local wall shear values with as much accuracy as in the two-dimensional case provided a reasonable number of measured velocity points are recorded in the wall similarity region.

The experimental data plotted in Fig. 22 represents some of the best fits and the two worst fits of the $\bar{\phi} = 45°$ data to lines of constant C_{fx}. For each flow angle, stations 3, 11, 10, and 28 generally represent the worst to the best fits, respectively.

The actual plot used to determine the values of C_{fx} has an enlarged linear scale of 10 squares per inch, with one inch representing an increment of 0.02 in u/u_1, and an enlarged log scale with one cycle covering approximately 10 inches. Lines of constant C_{fx} were drawn in at increments of 0.0002. A linear interpolation was used between these lines to determine the values of the constant C_{fx} lines that were drawn through the data points. For data points that did not fall along lines of constant C_{fx}, a straight line was drawn through the data points and the value of C_{fx} was evaluated at the point where a line of constant $y \cdot u_1/\nu = 5{,}000$ intersected the line through the data points. The method is illustrated in Fig. 21 for station 3, $\bar{\phi} = 45°$.

Law-of-the-Wall Variables. Once the axial skin-friction coefficients had been determined, the law-of-the-wall variable for the inner profile, u^+ and y^+, could be calculated. Making use of equation 25, the values of u^+ and y^+ can be easily calculated from their definitions.

The logarithmic velocity-distribution equation for turbulent flow is attributed to Prandtl, who used his mixing length theory as a basis. As discussed in the previous section, the constants used in the universal velocity law were those of Nikuradse. Using his values for the constants, the equation becomes

$$u^+ = 2.5 \cdot \ln y^+ + 5.5 \qquad (28)$$

Values of u^+ versus y^+ were then plotted on semi-log paper (see Fig. 22) and compared with the assumed relation given by equation 28.

Dimensional values of the axial and tangential wall shear values are plotted in Figs. 23 and 24. Inner wall axial shear values obtained separately from a calibrated Preston tube and the Pitot cylinder probe-Clauser chart are in agreement. Outer wall tangential shear stress values are approximately twice as great as the inner wall values, reflecting the large tangential velocity gradients near the outer wall shown in Fig. 19. The inner wall shear data exhibit a wavy behavior in the range $x/D_h < 10$ which reflect the pressure distributions plotted in Fig. 16. Axial pressure distributions are given for $(r - r_i)/(r_o - r_i) = 0$ (inner wall), and 0.2, 0.4, 0.6, 0.8, and 1.0 (outer wall). For $x/D_h > 10$, the inner wall pressure gradient is negative but small. At other radial locations, the local pressure gradients are positive.

The entrance pressure losses are largest near the outer wall. Here, the pressure gradient in the axial direction is due, on one hand, to the effect of accelerating, and overaccelerating, the flow (which initially has no axial component) to the velocity it attains at station x. On the other hand, ultimate radial pressure equilibrium and the axial decay of angular momentum lead to complex pressure patterns.

Local axial shear coefficient profiles for $\bar{\phi} = 45°$ are given in Fig. 26 at five axial stations. These values were obtained by numerical integration of equation 9', omitting the turbulence intensity change term (term 5). The radial location for zero axial shear moves outward from $\Delta r/\Delta r_o = 0.34$ at station 7 to $\Delta r/\Delta r_o = 0.61$ at station 24. The axial velocity profiles attain their maximum values (u_1) at $\Delta r/\Delta r_o = 0.52$ at station 7 and 0.58 at station 24. This discrepancy will prove to be serious when eddy diffusivities are computed later. The outer portions of the profile at station 7 indicate a thick constant shear region.

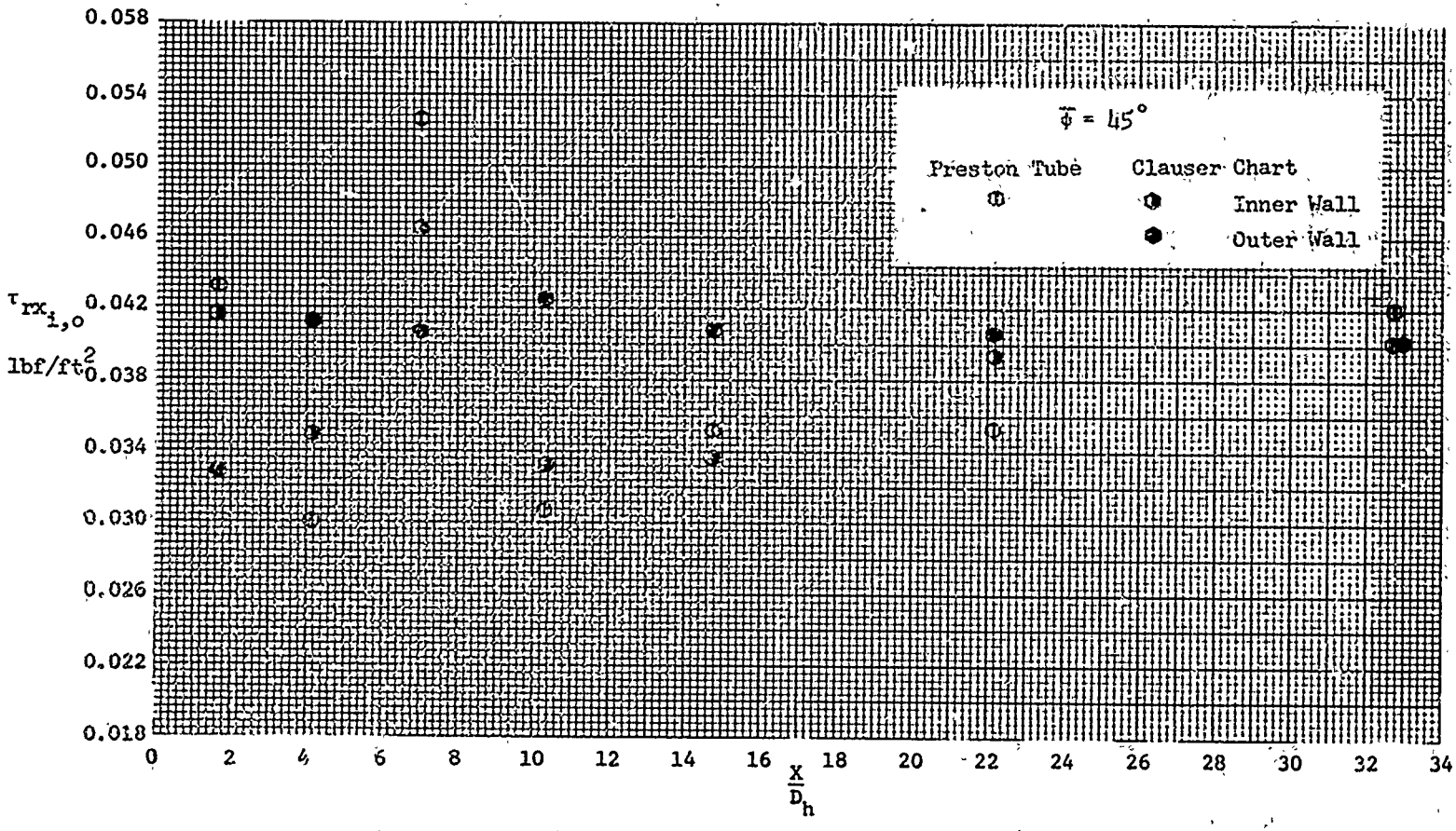

Figure 23. Experimental Values of Inner and Outer Wall Axial Shear.

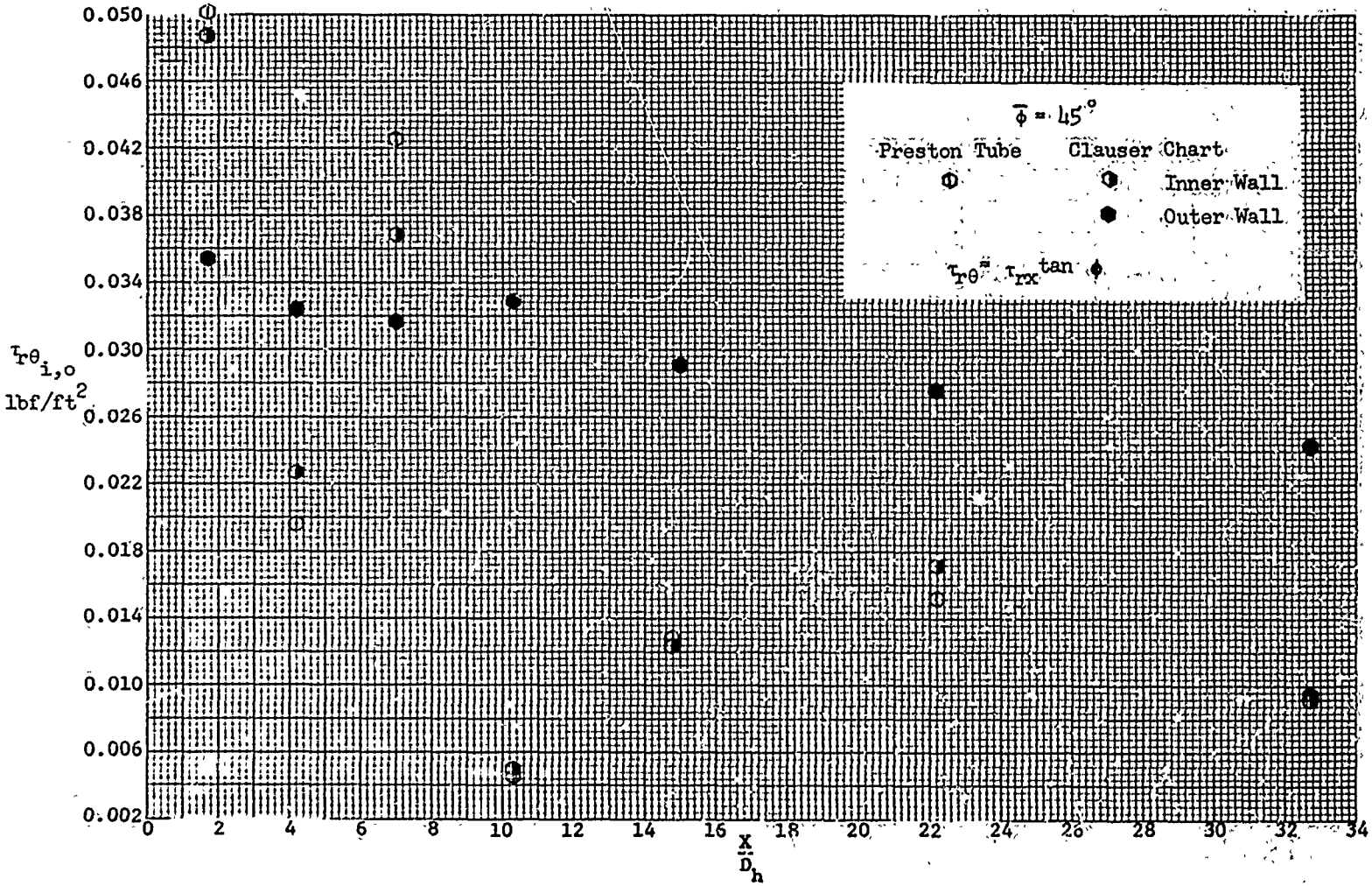

Figure 24. Experimental Tangential Shear.

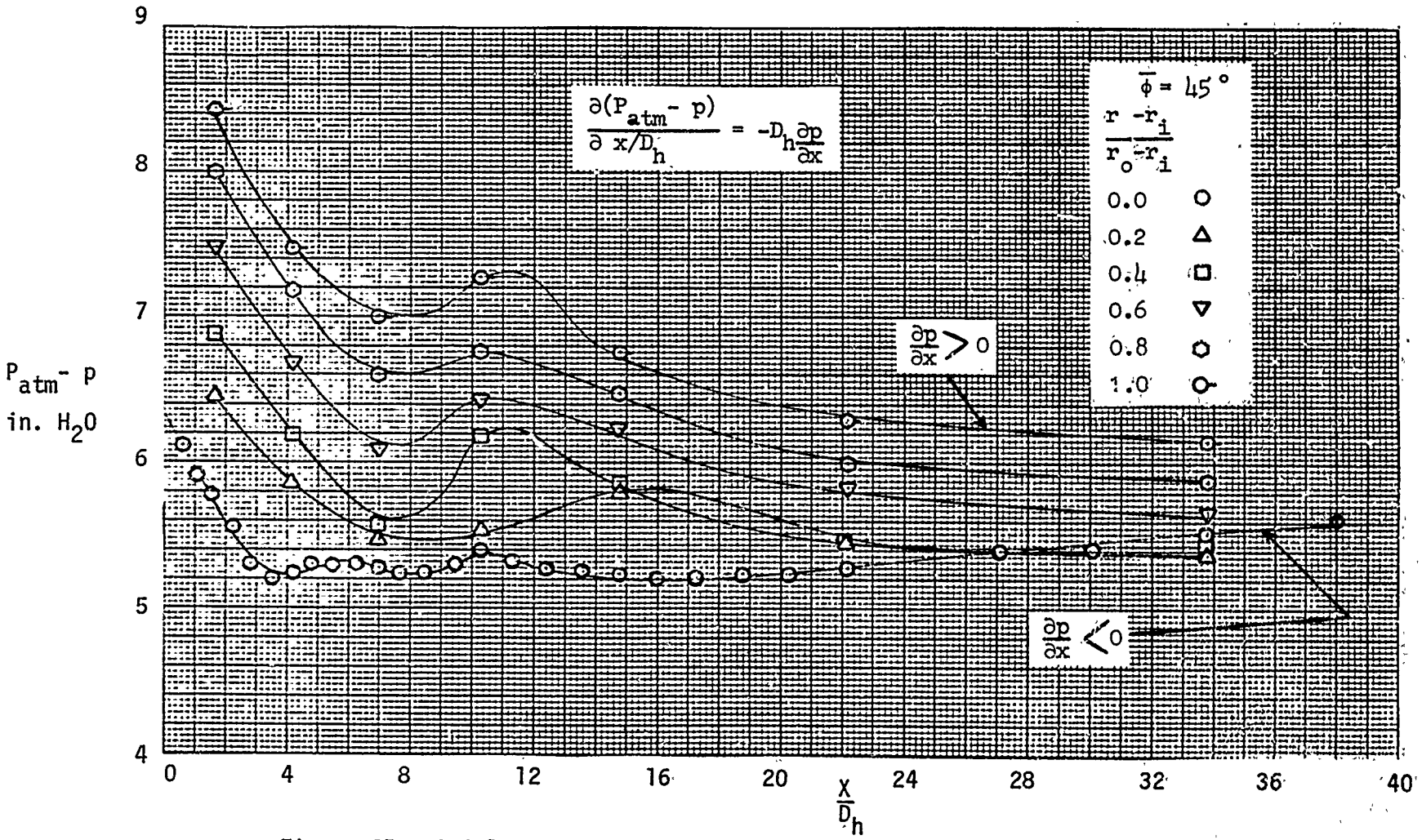

Figure 25. Axial Pressure Distribution at Several Radial Locations.

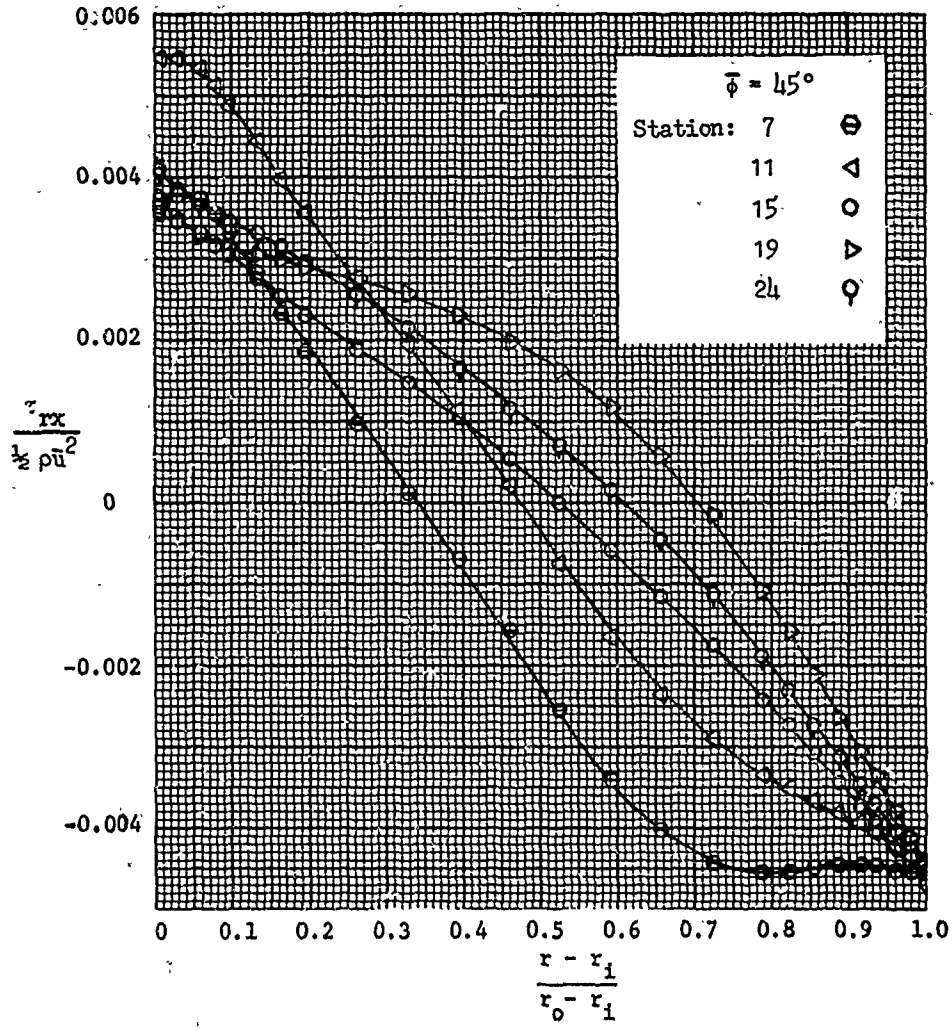

Figure 26. Radial Distribution of Axial Shear.

Contribution of the individual terms in equation 9', which sum to the local shear, are given in Fig. 27 for $\bar{\phi} = 45°$, at station 7. Term 1 (circles) represents the measured inner wall shear modified by the radius ratio r_i/r. Term 2 (triangles) involves axial derivatives in the integral of the axial velocity. This second term is zero at each wall and nearly symmetrical because of axial velocity near-symmetry. At the outer wall, the integral represents the average axial velocity which does not change significantly with x. As the flow develops, the velocities decrease such that term 2 is positive. Term 3 (inverted triangles) result from changes in kinetic energy. These points are all negative and nearly symmetrical about the radial location for maximum axial velocity. The fourth term (squares) represents the net pressure force term. This term is very small near the inner radius but grows due to the increased swirl near the outer wall. The total shear, plotted as the x's, is the sum of terms 1 - 4.

Similar comparisons are available in Fig. 28. Here the composition of the axial shear at $\Delta r/\Delta r_o = 0.2$ is given at 5 axial stations. This radial location was selected because the swirl velocities are normally near their maximum values nearby. This figure does not answer the question of exactly how the inner wall shear obtains its' value. It is simply a measured value and the integral equation 9' demonstrates why the shear changes radially. The effect of swirl enters only indirectly through the pressure and the axial profile modifications. At $\Delta r/\Delta r_o = 0.2$ the acceleration and kinetic energy terms tend to cancel each other out while the pressure term remains small such that the local shear is nearly equal to the inner wall value.

Comparable local tangential shear curves, resulting from the numerical integration and differentiation of equation 11', are given in Figs. 29 and 30 for $\bar{\phi} = 45°$. Near the inlet $\tau_{r\theta} \approx 0$ at very small $\Delta r/\Delta r_o$ values (less than 0.1). At station 24, $\tau_{r\theta} \approx 0$ at $\Delta r/\Delta r_o = 0.44$. Near the inner wall, $\tau_{r\theta}$ is proportional to $\Delta r/\Delta r_o$ whereas near the outer wall $\tau_{r\theta}$ is constant.

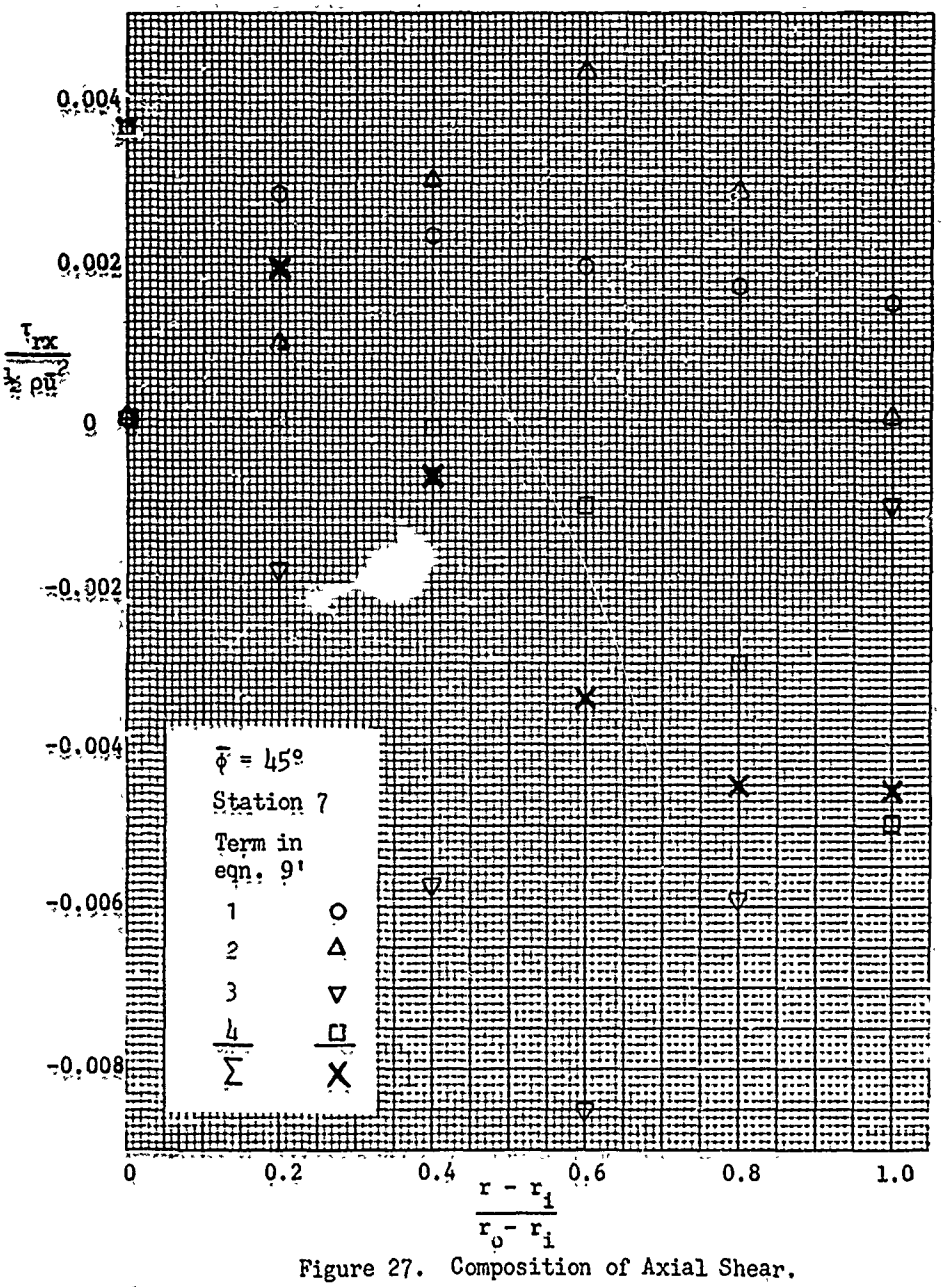

Figure 27. Composition of Axial Shear.

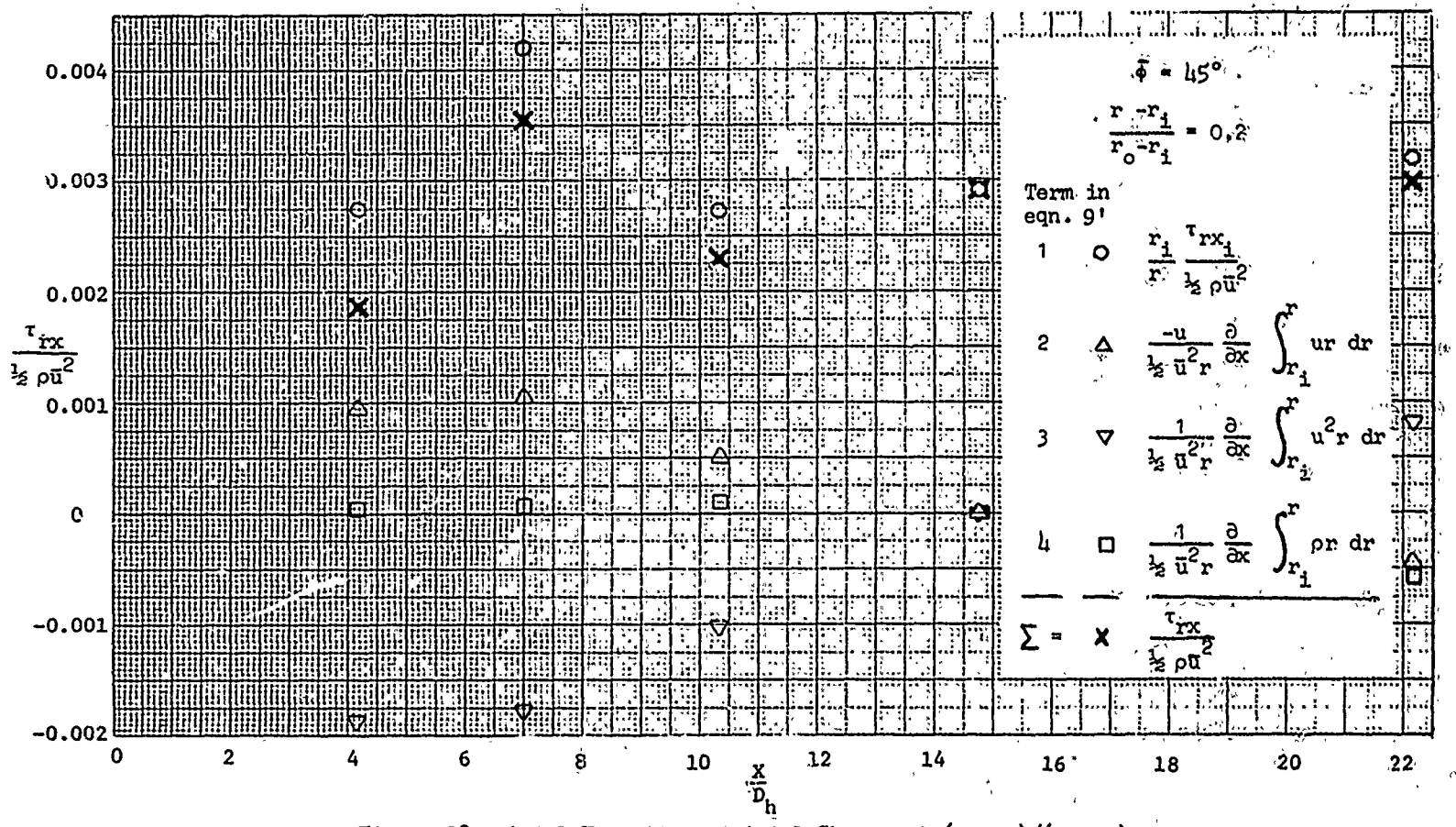

Figure 28. Axial Variation of Axial Shear at $(r - r_i)/(r_o - r_i) = 0.2$

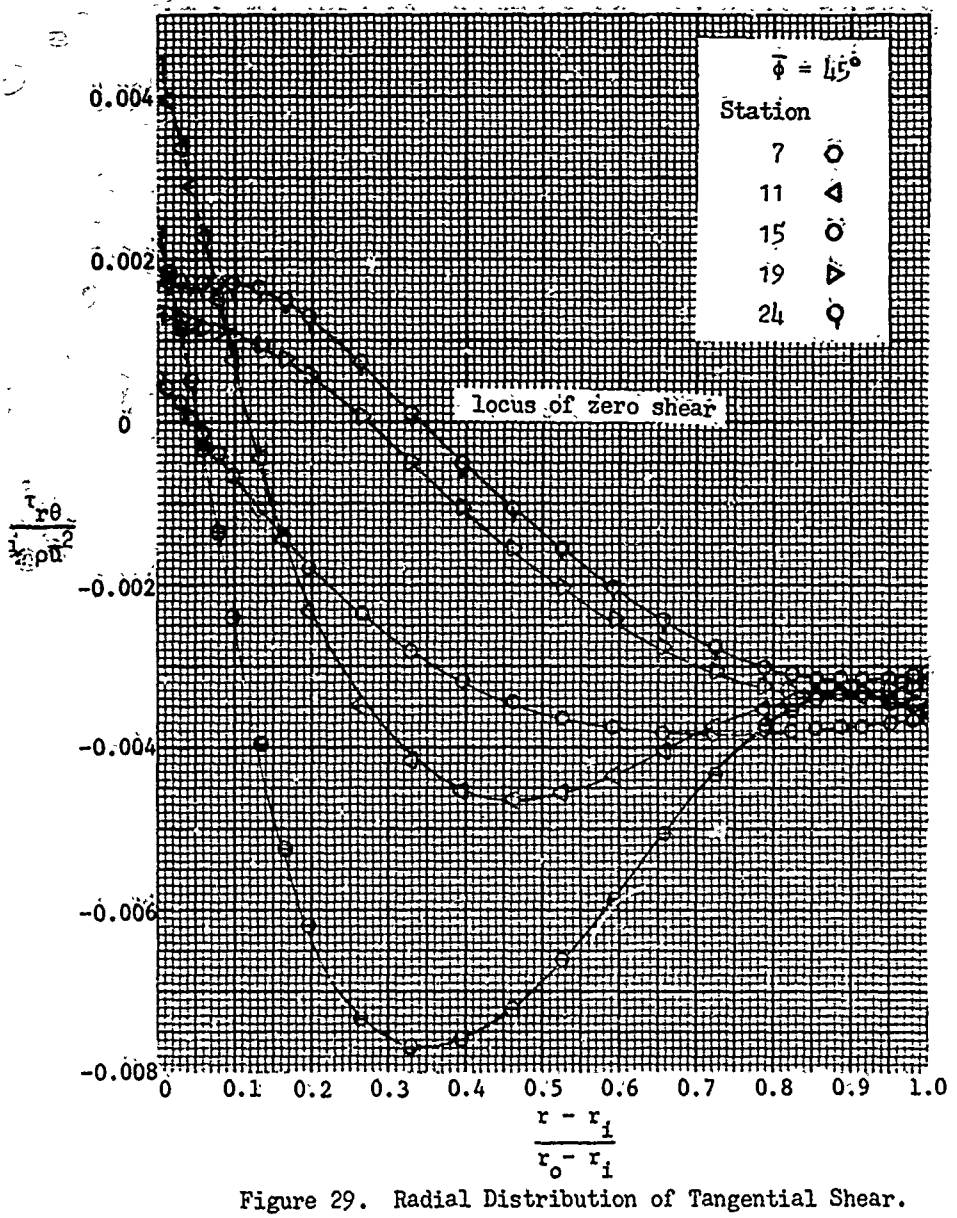

Figure 29. Radial Distribution of Tangential Shear.

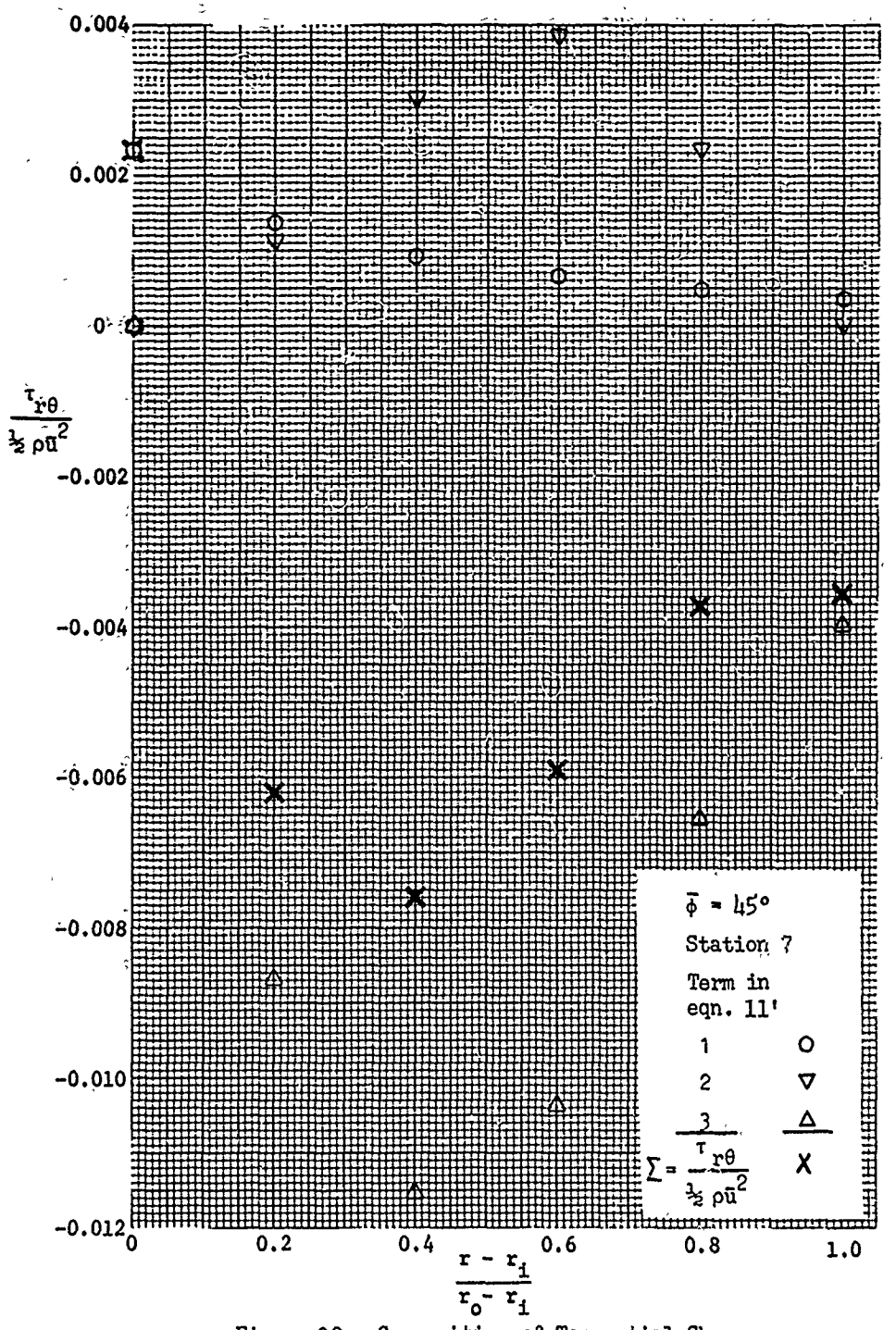

Figure 30. Composition of Tangential Shear.

The magnitudes of the individual terms in equation 11' are plotted in Fig. 30 for $\bar{\phi} = 45°$, station 7. The circles represent term 1, the torque per unit length on the inner wall modified by a radius ratio squared. Terms 2 and 3 are the change in axial flux of angular momentum, and the effect of acceleration on the axial flux of angular momentum. These terms are of opposite sign and tend to cancel. Symmetry about the position of maximum axial velocity is weak because the swirl velocity is quite unsymmetric. The tangential shear changes most rapidly in the radial direction near the zero shear location.

The dominant term is the change in axial flux of angular momentum between the inner wall and location r. The shear "bulge" located in the range $0.2 < \Delta r/\Delta r_o < 0.8$ appears to be an effect of the entrance condition which has disappeared between station 15 and 19. The tangential shear profiles at stations 19 and 24 are quite similar in shape, indicating that the entrance effects are probably finished and the final process of swirl decay is underway.

The tangential shear near the outer wall is approximately twice as great as the inner wall shear. This reflects the existence of larger swirl velocities near the outer wall and, presumably, the increased turbulence.

Axial variations of the shear component terms are plotted in Fig. 31 for location $\Delta r/\Delta r_o = 0.2$, $\bar{\phi} = 45°$. In the initial swirl decay region, $x/D_h < 12$, the local shear is determined almost entirely by the change in the axial flux of angular momentum. As the swirl decays and becomes progressively weaker, a type of fully developed situation arises where the two integral terms in equation 11' approximately cancel while both tend to zero, such that the local shear is nearly equal to the inner wall shear.

EDDY DIFFUSIVITIES

Axial Diffusivities. Axial eddy diffusivities were computed from the relation

$$\tau_{rx} = \rho(\nu + \varepsilon_{rx}) \frac{\partial u}{\partial r} \tag{29}$$

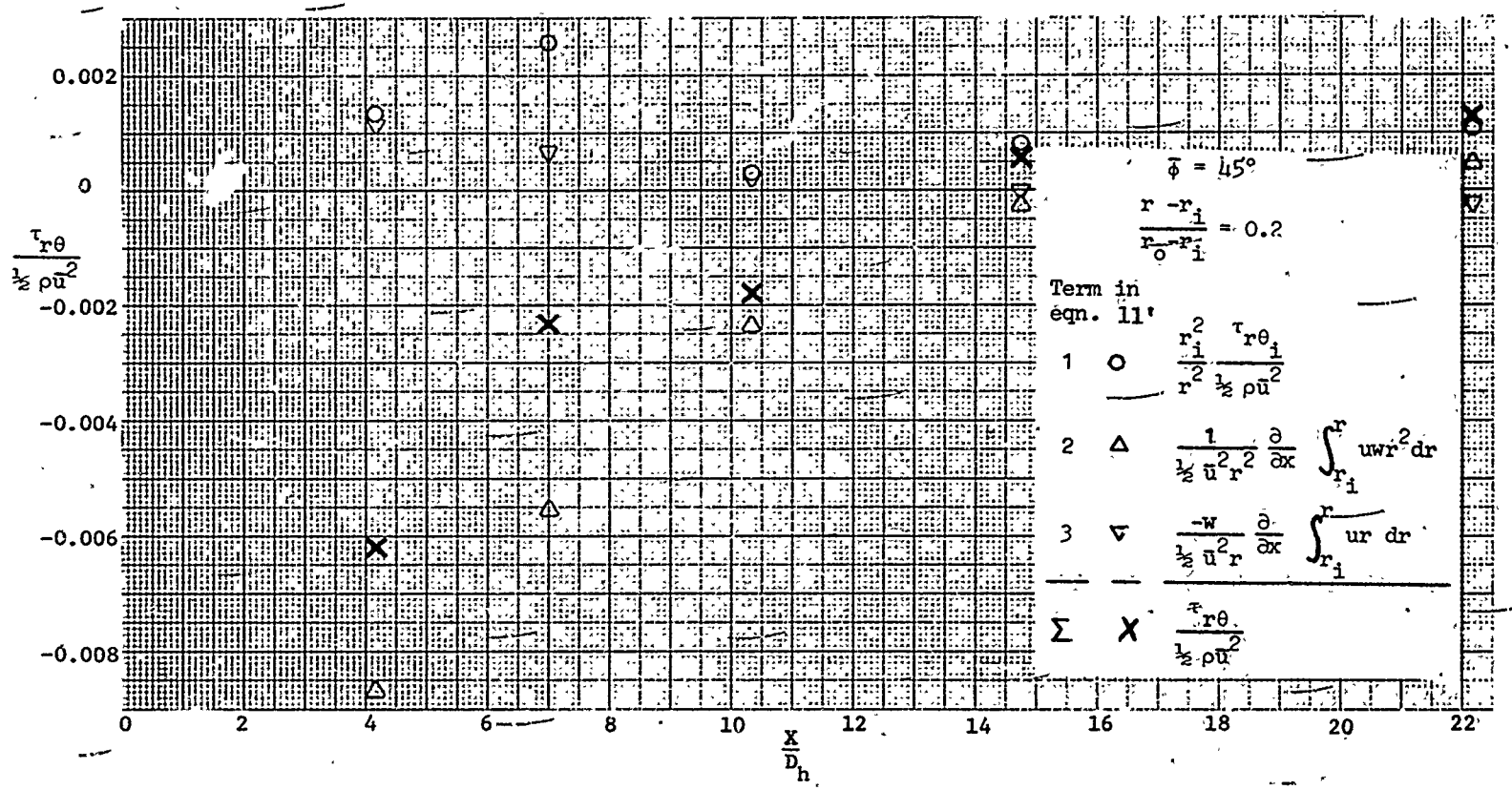

Fig e 31. Axial Variation of Tangential Shear at $(r - r_i)/(r_o - r_i)$ = 0.2

The axial diffusivities are plotted in Figs. 32-36 as the ratio of turbulent to molecular diffusivities plus unity ($\varepsilon_{rx}/\nu + 1$) vs the radial station $\Delta r/\Delta r_o$. The ordinate is the ratio of the total diffusivity to the molecular diffusivity for air at the same temperature. The axial diffusivity data are lowest near the walls in all cases. Diffusivities for $\Delta r/\Delta r_o > 0.5$ usually exceed corresponding values below 0.5. For example, a $\Delta r/\Delta r_o$ of 0.1 is located the same radial distance from the inner wall as $\Delta r/\Delta r_o = 0.9$ is from the outer wall. At station 7, that data for zero swirl are represented by the circles. One point near $\Delta r/\Delta r_o = 0.4$ is missing because the shear stress was opposite in sign to the velocity gradient. The observed diffusivity ratio exceeds 600 near the inner wall for $\bar{\phi} = 60°$ as compared with a value of 120 for $\bar{\phi} = 0$. A great many 60° swirl points are missing near the outer wall. The apparently "wild" points in the central areas of the figure are misleading. All of the data is systematic. The apparent scatter is associated with the onset of zero shear and zero gradients. The total axial diffusivity ratio, as computed from measured shear stress and measured velocity gradient, goes to infinity--plus or minus--in a variety of ways. Most of the effects observed in the range $0.3 < \Delta r/\Delta r_o < 0.7$ are due to this effect.

The axial velocity profiles are nearly fully developed by station 24. Therefore, comparisons may be made with other fully developed diffusivity results and predictions. The experiments of Jonsson [64] are closely applicable. He worked with a concentric annulus with a radius ratio of $r_i/r_o = 0.56$ (compared with the present value of 0.4). His diffusivity data apply at $x/D_h = 132$ and an axial Reynolds number of $Re_{D_h} = 115{,}000$. The agreement is fair although Jonsson's inner data lie above, and the outer data below, the present zero swirl data at station 24.

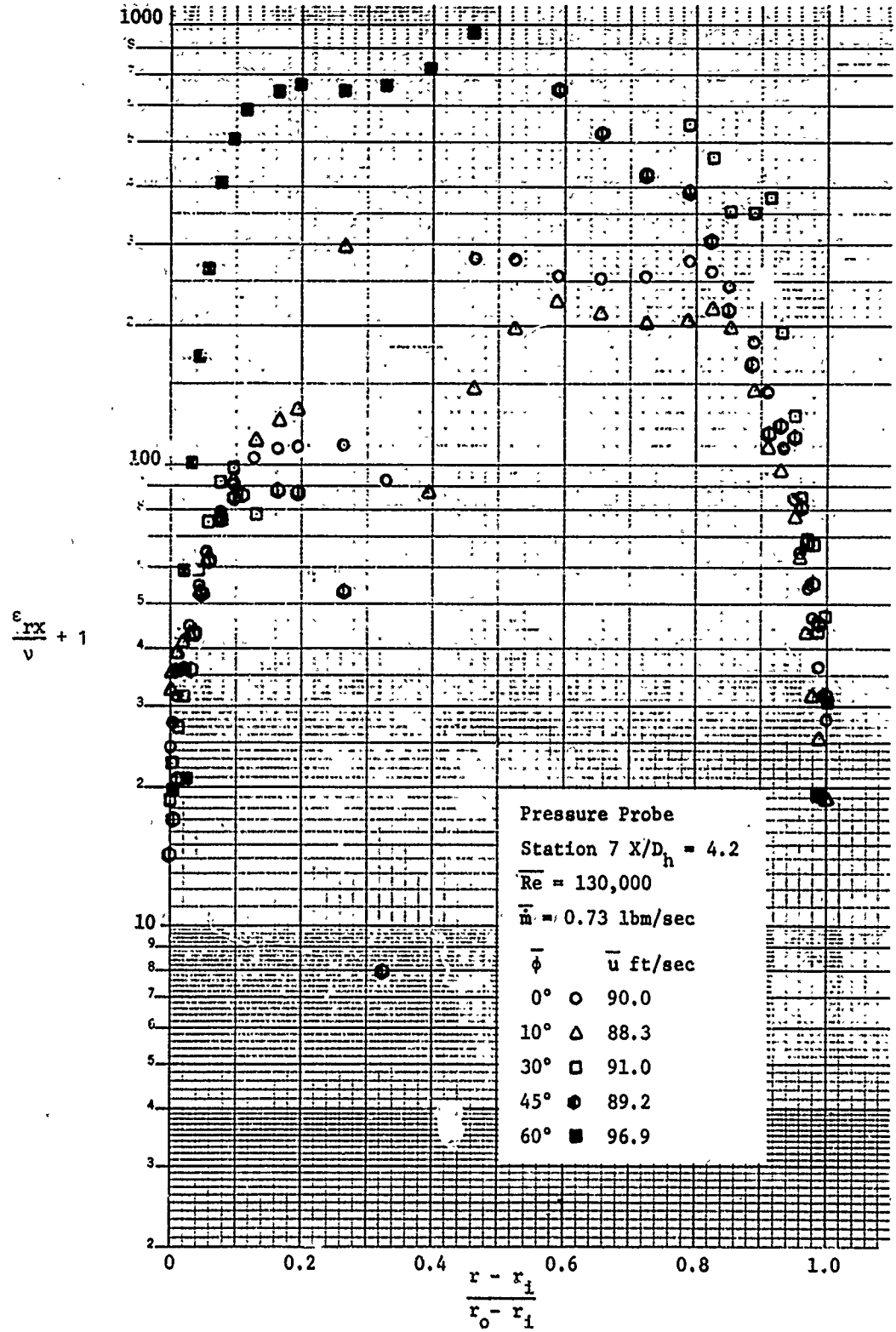

Figure 32. Turbulent Axial Eddy Diffusivity--X/D$_h$ = 4.2

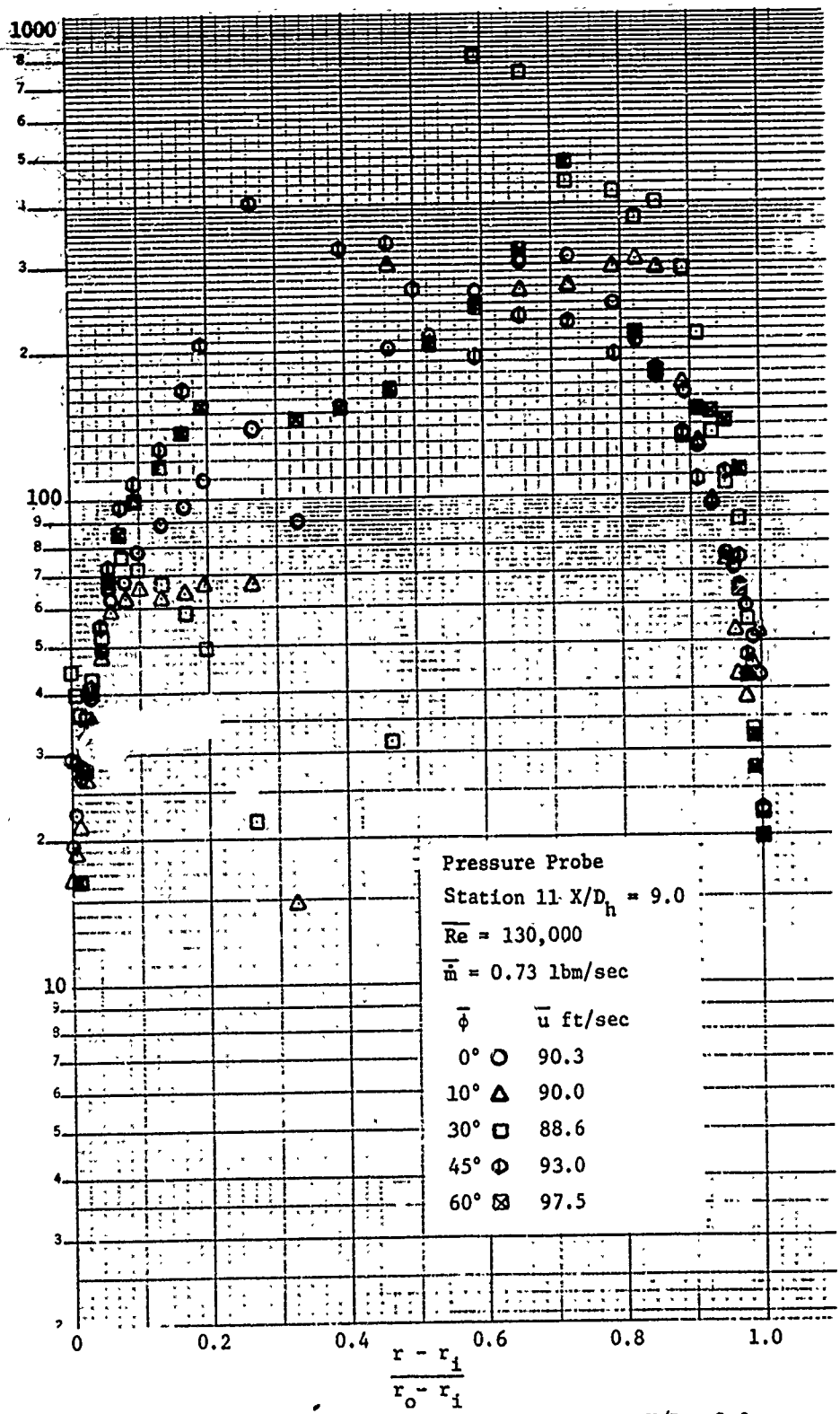

Figure 33. Turbulent Axial Eddy Diffusivity--X/D_h = 9.0

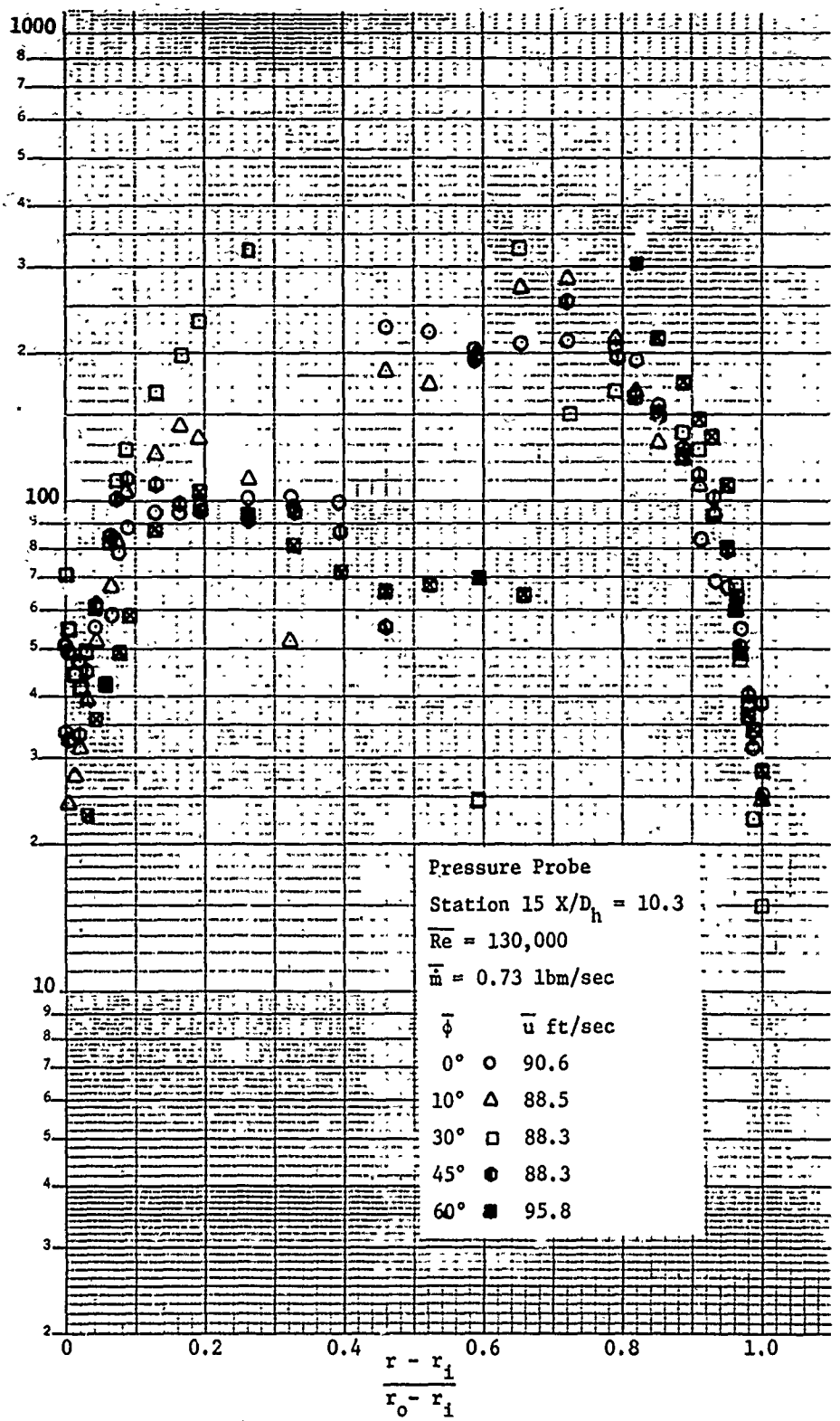

Figure 34. Turbulent Axial Eddy Diffusivity--X/D_h = 10.3

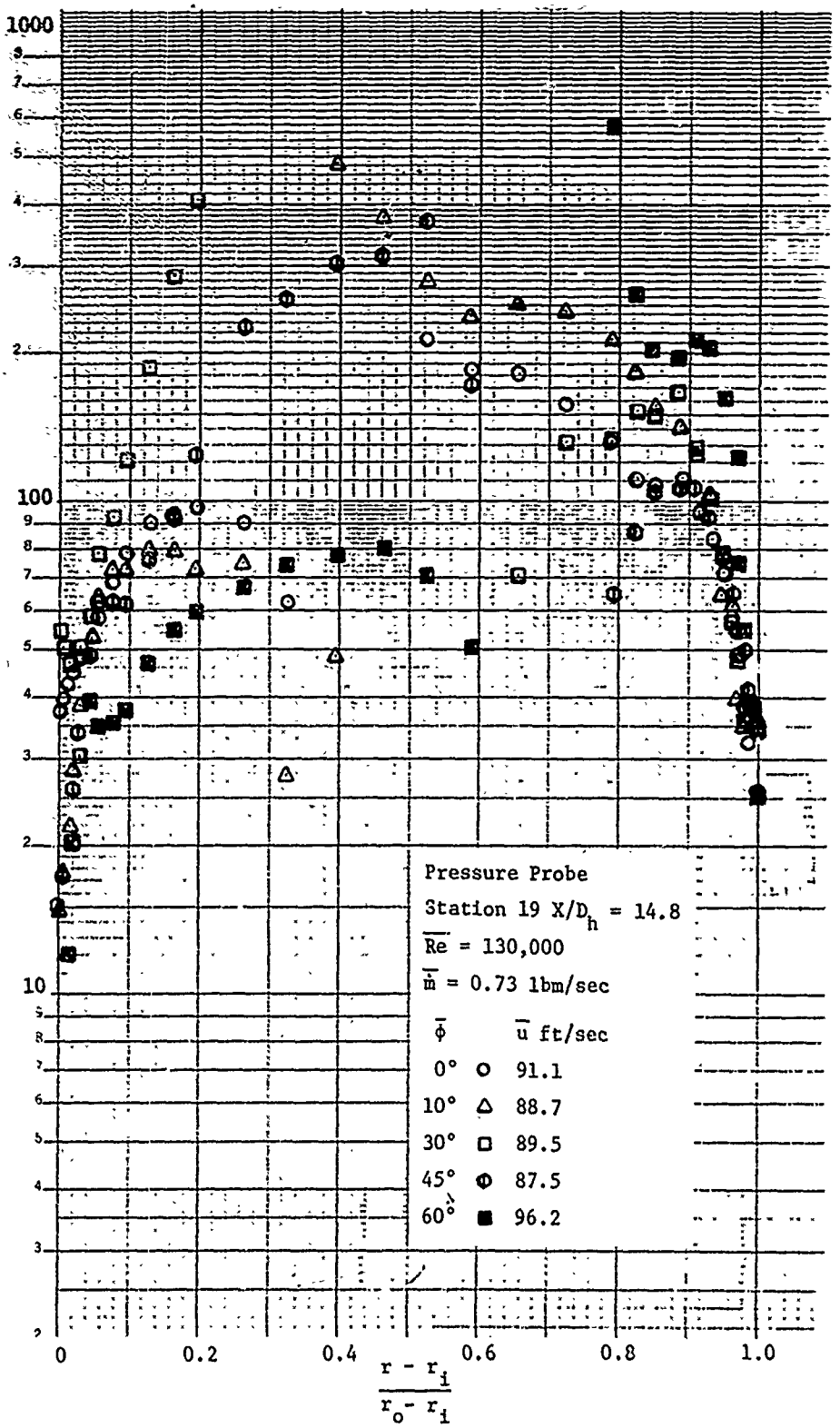

Figure 35. Turbulent Axial Eddy Diffusivity--X/D_h = 14.8

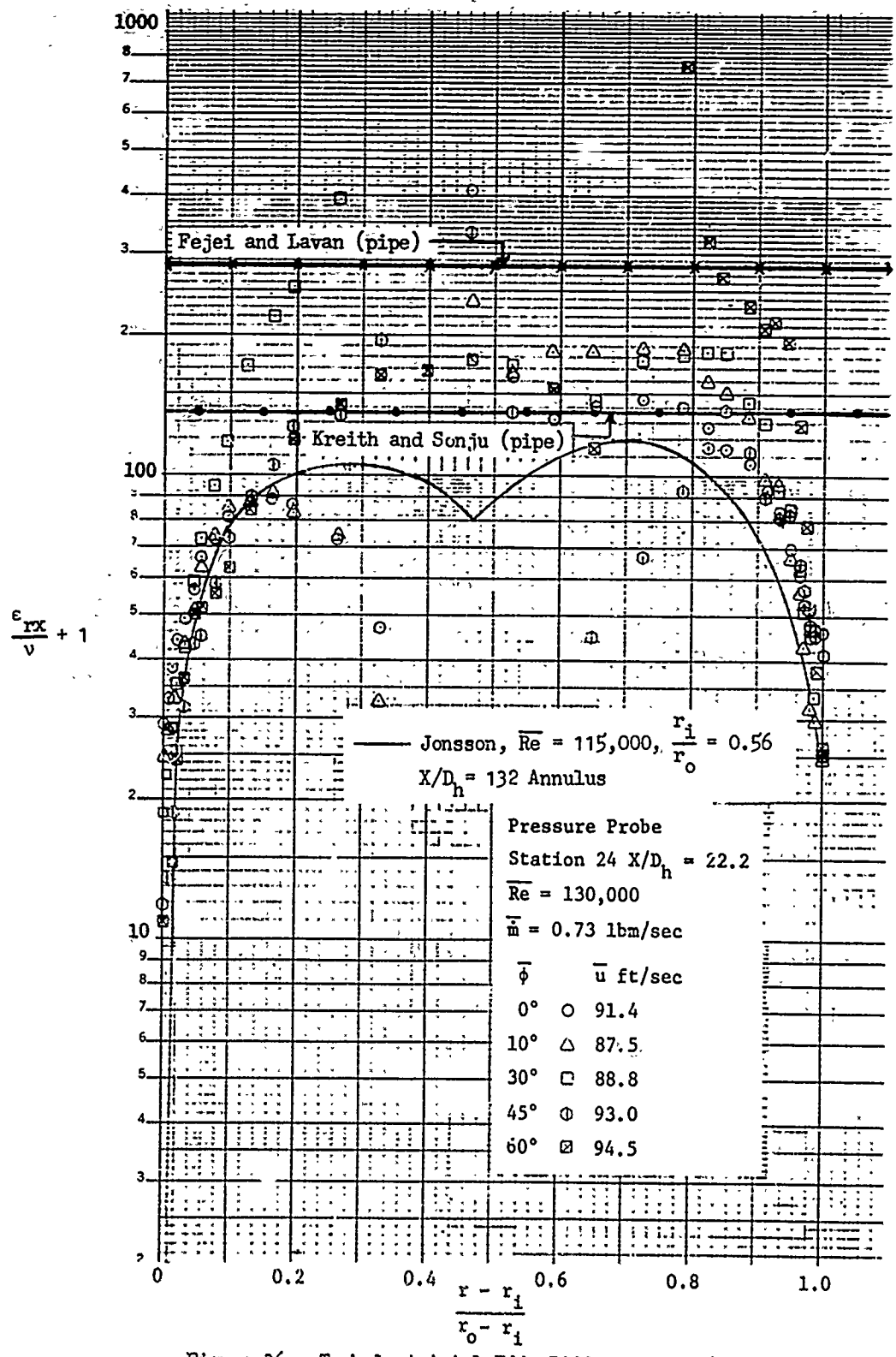

Figure 36. Turbulent Axial Eddy Diffusivity--X/D$_h$ = 22.2

Two emperical relations, which compute a constant diffusivity for solid body rotation in a stationary pipe, are plotted in Fig. 36. They are labelled Fejer and Lavan [16]

$$\frac{\varepsilon_{rx}}{\nu} = 8.32\left(\frac{\overline{U}D_h}{\nu}\right)^{0.3} = (8.32)(1.3\text{x}10^5)^{0.3} = 285 \tag{30}$$

and Krieth and Sonju [37]*

$$\frac{\varepsilon_{rx}}{\nu} = 5.44\text{x}10^{-3}\left(\frac{\overline{U}D_h}{\nu}\right)^{0.86} = (.00544)(1.3\text{x}10^5)^{0.86} = 135.9 \tag{31}$$

Away from the wall boundary layers, most of the present data at station 24 fall within these values.

Recently, Wassan, Tien, and Wilke [65] pointed out that most of the proposed (axial) diffusivity distributions do not satisfy the theoretical criterion of Townsend, which requires that the turbulent contribution to the Reynolds stress-- $\rho\overline{u'v'}$ is proportional to y^n near the wall where n is not less than three. They propose the relation

$$\frac{\varepsilon_{rx}}{\nu} = \frac{4.16\text{x}10^{-4}y^{+3} - 15.15\text{x}10^{-6}y^{+4}}{1 - 4.16\text{x}10^{-4}y^{+3} + 15.15\text{x}10^{-6}y^{+4}} \tag{32}$$

which applies for $0 \leq y^+ \leq 20$.

---

* The predictions of Krieth and Sonju are based on data presented in an M.S. Thesis by Musolf [40]. Mussolf's data is not complete because he did not measure either the axial or the tangential velocity profiles. His tangential velocities were calculated from measurements of the local flow direction, the total mass flow through the pipe, and an assumed axial velocity distribution.

The lowest y^+ values measured in the present study are found in Fig. 22 to be 20. For a y^+ of 20, the above equation yields $\varepsilon_{rx}/\nu = 10$.

For simple mixing length theories in which $\tau = \rho \ell^2 (\partial u/\partial y)^2$, $\ell = ky$

$$\frac{\varepsilon_{rx}}{\nu} = ky^+ \tag{33}$$

Normally, $k = 0.4$ and $\varepsilon_{rx}/\nu = 8$ for $y^+ = 20$. It is clear from these values that the present data were not taken sufficiently close to either wall to distinguish any viscous layer details.

Tangential Diffusivities. The tangential eddy diffusivities were computed using the defining relation

$$\tau_{r\theta} = \rho(\nu + \varepsilon_{r\theta})\left(\frac{\partial w}{\partial r} - \frac{w}{r}\right) \tag{34}$$

Again, the results are plotted vs $\Delta r/\Delta r_o$ in Figs 37-41 with the ordinate taking the form of the ratio of total tangential diffusivity to molecular diffusivity ($\varepsilon_{r\theta}/\nu + 1$). In general $\varepsilon_{r\theta} < \varepsilon_{rx}$. The values of $\varepsilon_{r\theta}$ are quite low near the inner wall--particularly at the large swirl rates. There is a definite decrease in $\varepsilon_{r\theta}$ with $\bar{\phi}$ near the inner wall at station 7 and at most of the following stations.

The emperical predictions of Fejer and Lavan [16] and Kreith and Sonju [37] for the decay of solid body rotation in pipes are plotted for reference. They represent average values in several senses. First, they apply to both the axial and the tangential diffusivities. Secondly, they do not vary with the radius. The predictions agree best near the outer regions of the annulus where most of the annular area occurs.

The fully developed curved channel experimental diffusivity results of Wattendorf also appear in Fig. 41. Near the inner wall, the straight channel

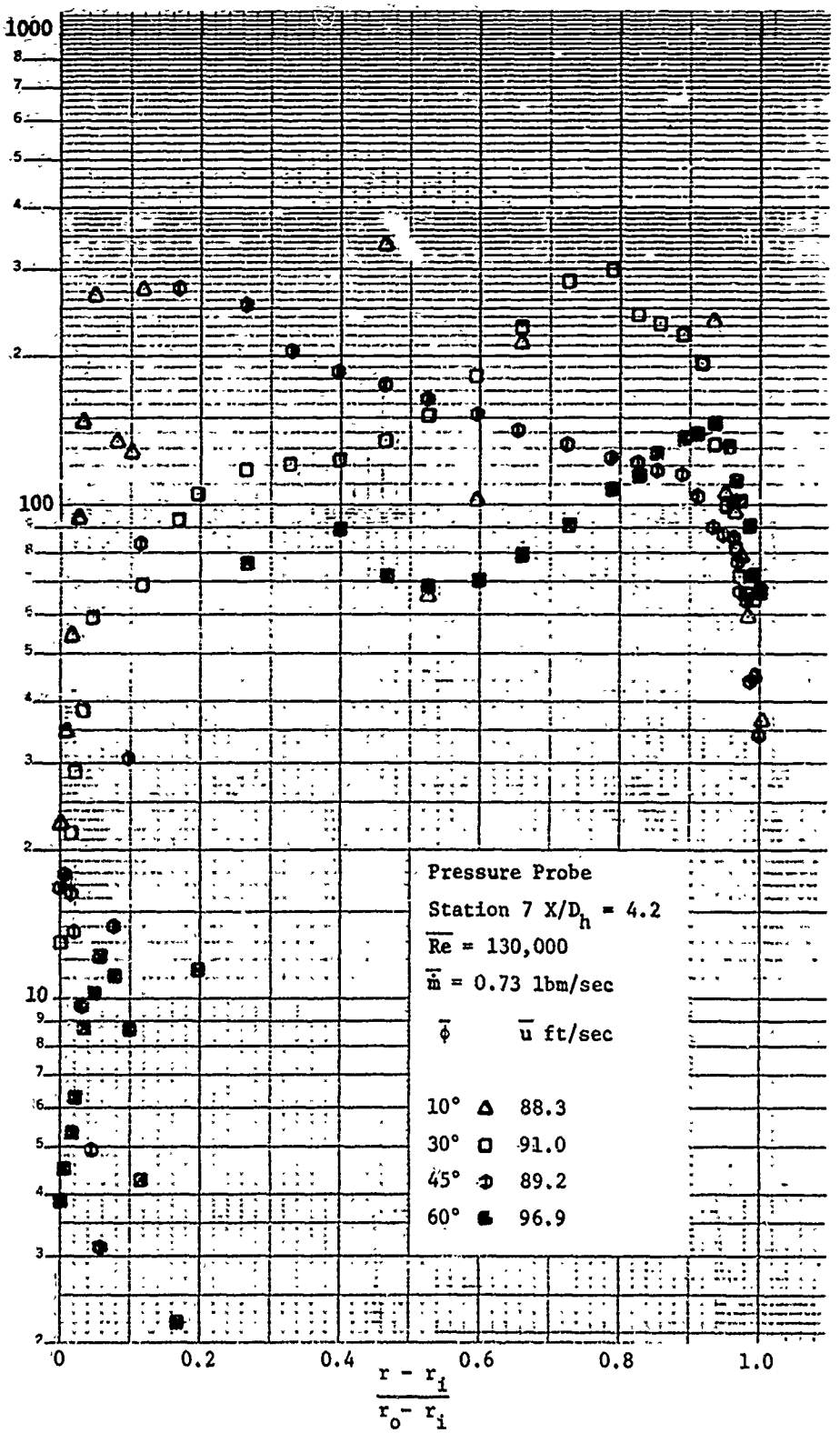

Figure 37. Turbulent Tangential Eddy Diffusivity--X/D_h = 4.2

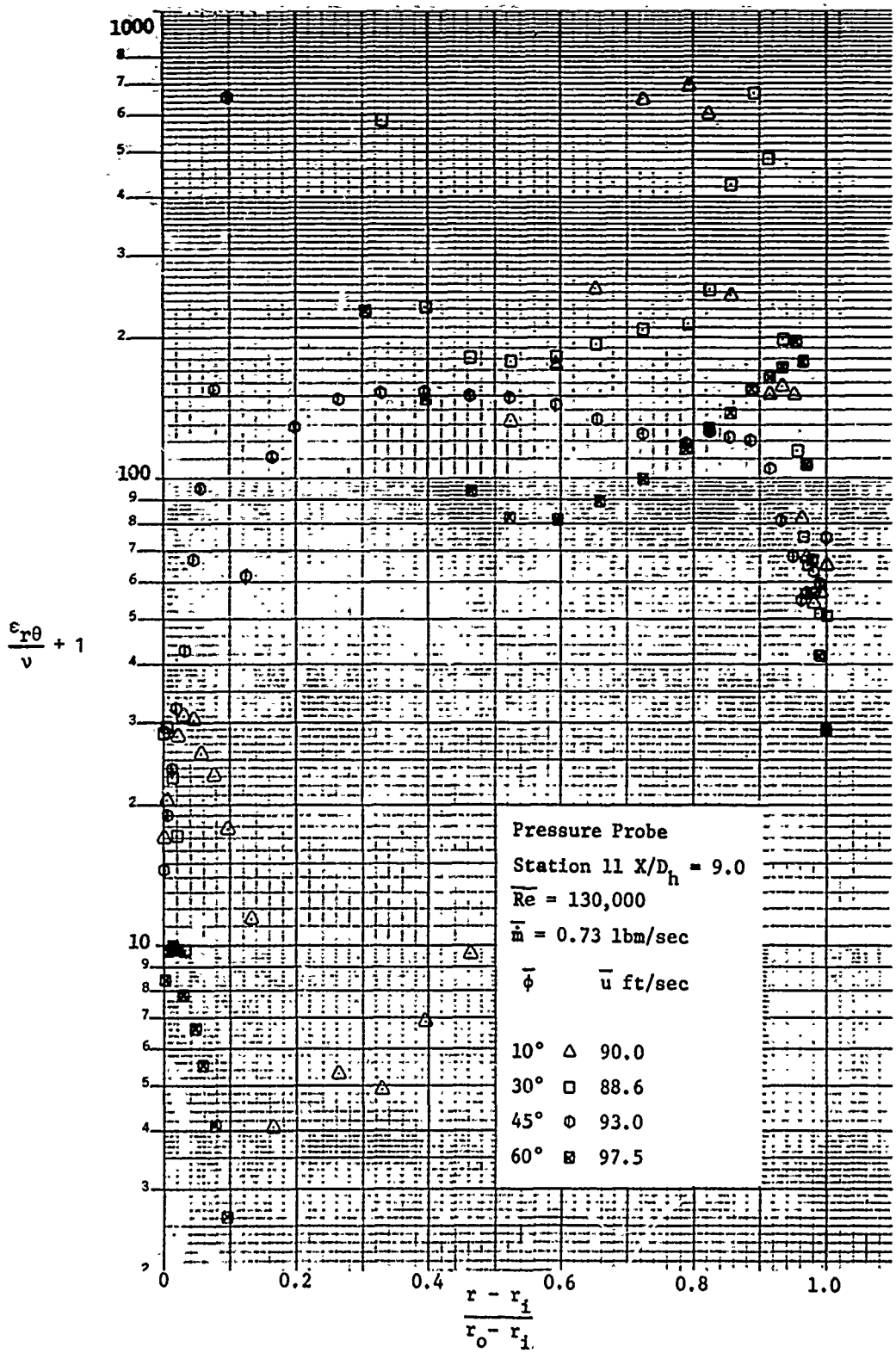

Figure 38. Turbulent Tangential Eddy Diffusivity--X/D_h = 9.0

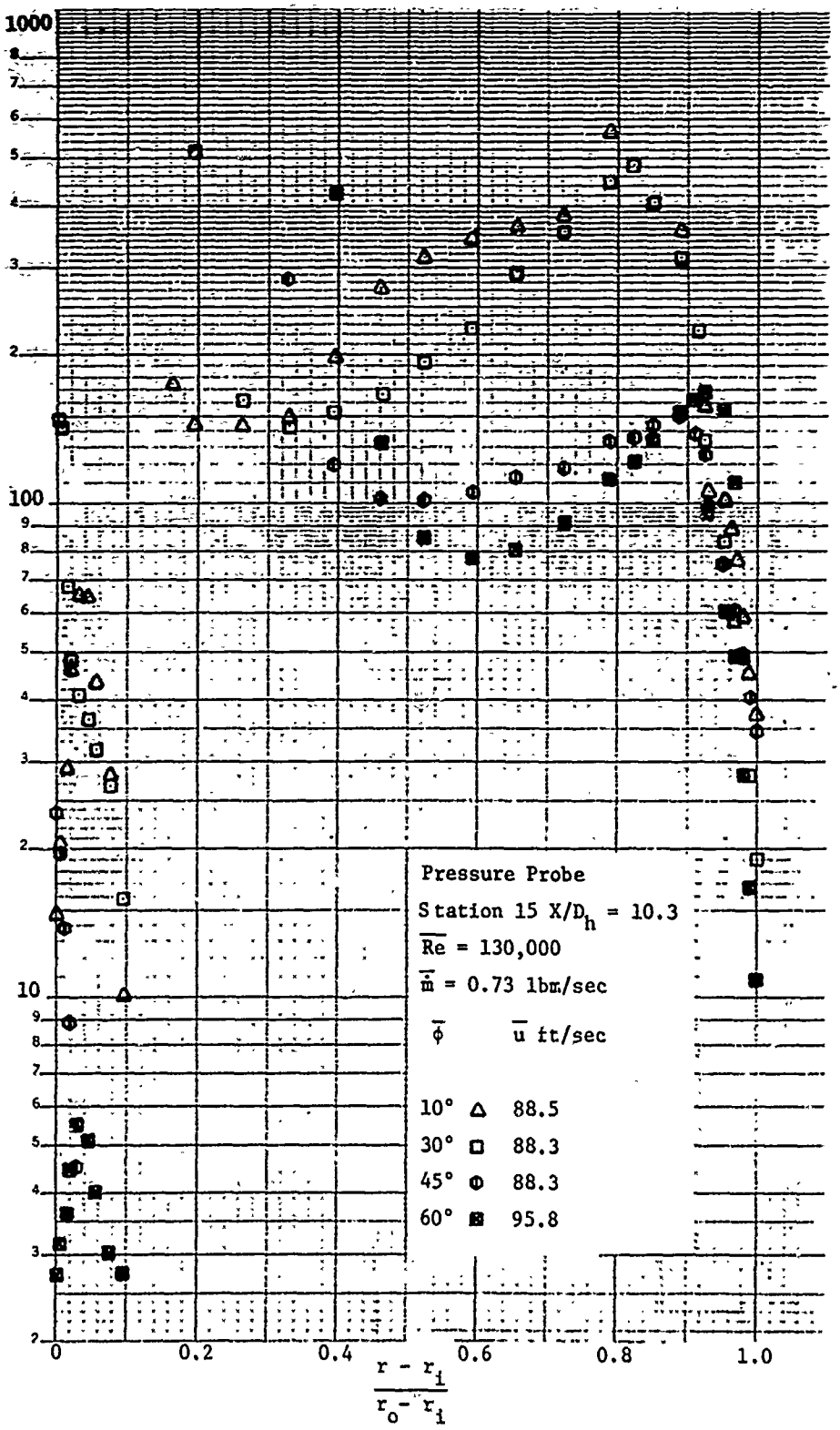

Figure 39. Turbulent Tangential Eddy Diffusivity--X/D_h = 10.3

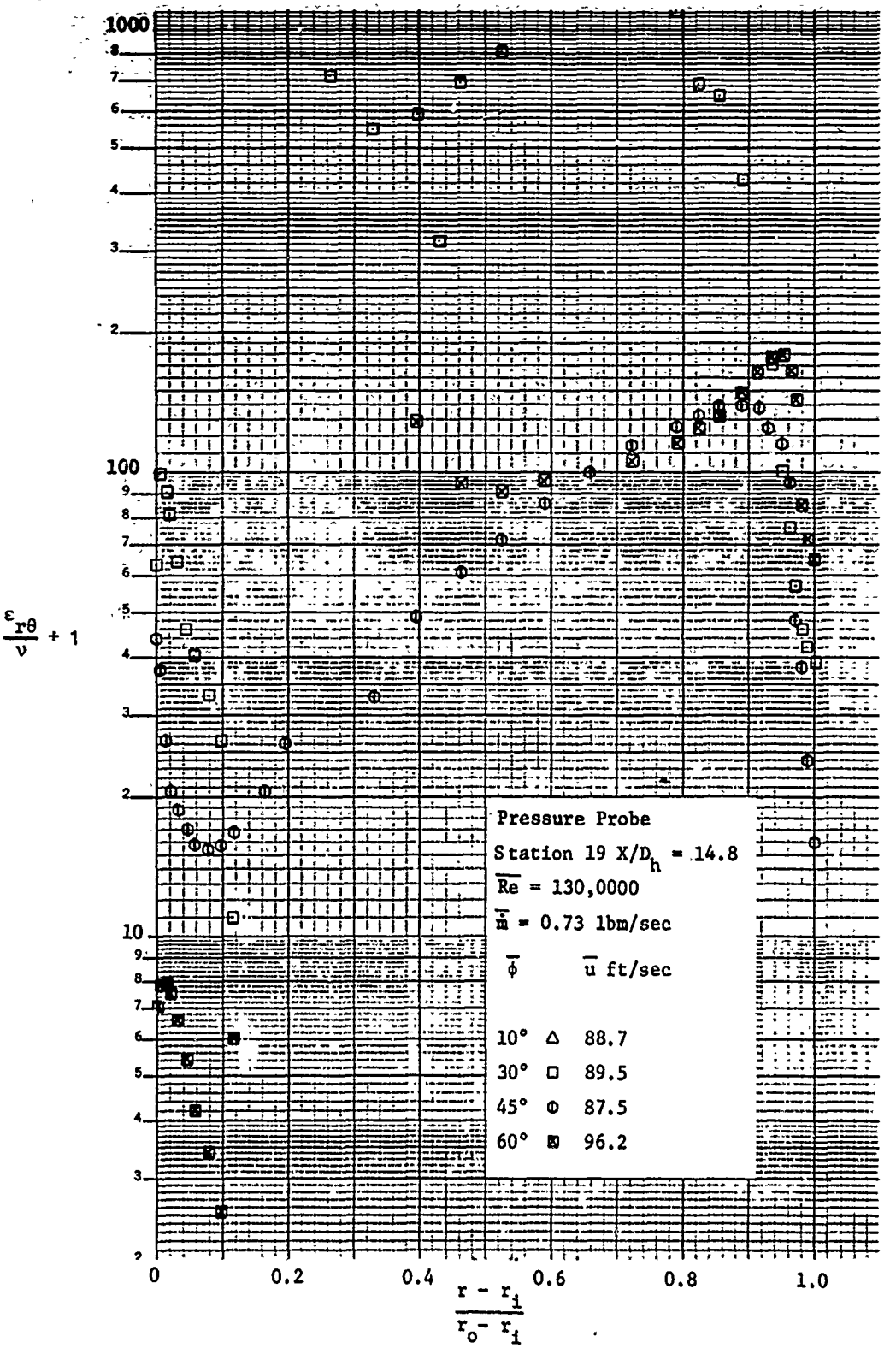

Figure 40. Turbulent Tangential Eddy Diffusivity--X/D_h = 14.8

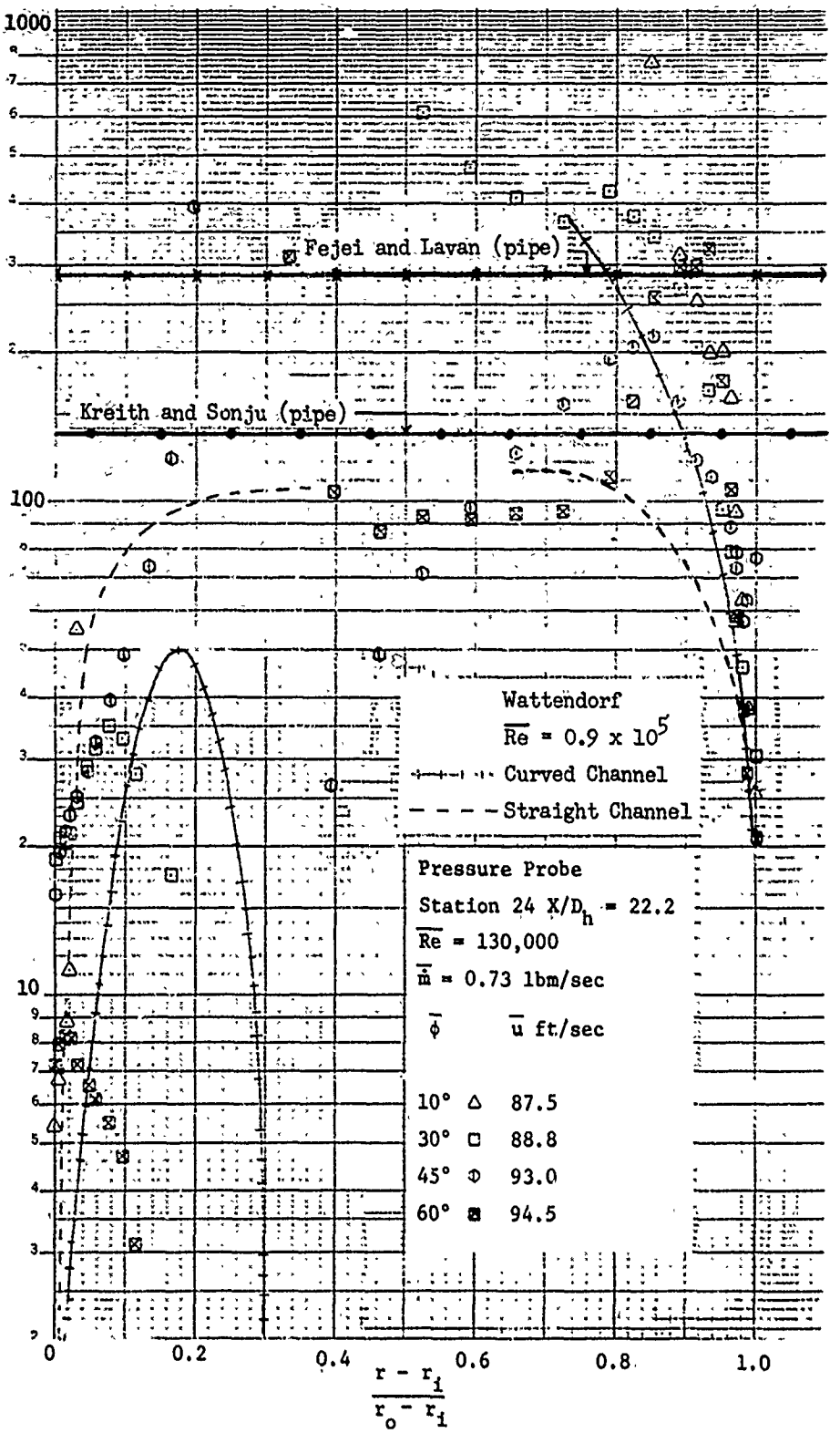

Figure 41. Turbulent Tangential Eddy Diffusivity--$X/D_h = 22.2$

diffusivities are approximately one-half the curved wall values. Near the outer wall, the reverse is true. The locations of the zeroes: $\partial w/\partial r = 0$, $(\partial w/\partial r - w/r) =$ and $(\partial w/\partial r + w/r) = 0$ closely match the present $\bar{\phi} = 30°$ data. In fact, the similarity in behavior in all respects suggests that the Wattendorf curved channel flow and the present flow are of the same class.

As is the case with the axial momentum transport, the locations of zer shear do not occur at the same radial location. Infinities in $\varepsilon_{r\theta}$ are approached. This is the same type of "apparent scatter" found in the axial diffusivity data. In general, the zero tangential shear location occurs closer to the inner wall than the zero axial shear because of the subtraction in the rate of strain term $(\partial w/\partial r - w/r)$. The computed diffusivities do increase, reaching maximum values at the edge of the tangential boundary layer adjacent to the outer wall. Lavan and Fejer [16] have suggested that in a decaying swirling flow in a station pipe, the eddy diffusivity is a strong (approximately cubic) function of the radial coordinate. This trend is usually followed by the present data outside of the point of zero shear. Finally, the diffusivity values in the outer swirl boundary layer decrease as the wall is approached.

Turning to the last stati , Fig. 41, the different behavior near the two walls is evident. The tangential diffusivities first increase with $\Delta r/\Delta r_o$. Outside of this "inner" boundary layer $\varepsilon_{r\theta}$ decreases, approaching a value of less than 10.

As was anticipated in the earlier sections, axial diffusivities near the inner wall are considerably lower than corresponding values near the outer wall. This is a result anticipated in the Introduction and is due, presumably, to the different turbulence characteristics of the two layers. Also, there appears to be a slight increase in outer wall axial and tangential diffusivities with an increase in swirl.

An alternate form of presenting the dimensionless diffusivities is revealed

in Figs. 42-51. The ratio of turbulent diffusivity to the product of wall friction velocity times an appropriate scale length is the inverse of a Reynolds number. The flow is divided into two parts by the zero shear radius. The two correlation parameters are

$$\frac{\varepsilon_{rx}}{u_i^*(r_{\tau_{rx}=0} - r_i)} \quad \text{or} \quad \frac{\varepsilon_{rx}}{u_o^*(r_o - r_{\tau_{rx}=0})} \tag{35}$$

where

u_i^* = inner wall friction velocity = $\sqrt{\tau_{rx_i}/\rho}$

u_o^* = outer wall friction velocity = $\sqrt{\tau_{rx_o}/\rho}$

$r_{\tau_{rx}=0}$ = radial location for zero axial shear

r_i = inner wall radius

r_o = outer wall radius

The radial location for zero shear was used rather than the more frequently used radius for maximum velocity because it is more sharply defined and also applies to the tangential case where the correlations used are

$$\frac{\varepsilon_{r\theta}}{w_i^*(r_{\tau_{r\theta}=0} - r_i)} \quad \text{or} \quad \frac{\varepsilon_{r\theta}}{w_o^*(r_o - r_{\tau_{r\theta}=0})} \tag{36}$$

The two abscissas are the fractional distances from either wall to the zero shear location. In effect, the inner scale is stretched disproportionately since $r_{\tau_{r\theta}=0} - r_i$ is typically 0.3 $(r_o - r_i)$. In short, the outer profiles are the more important since they represent the major fraction of the flow. The dashed line in each figure represents the simple mixing length limit, $\tau = \rho\ell^2(\partial u/\partial y)^2$ where $\ell = ky$ and $k = 0.4$. Since $\varepsilon_t/\nu = 0.4\ y^+$, $d(\varepsilon_t/u^*\Delta r)/d(y/\Delta r) = 0.4$. The constant k was determined from fully developed pipe, channel, and boundary layer experiments. It is drawn for reference purposes

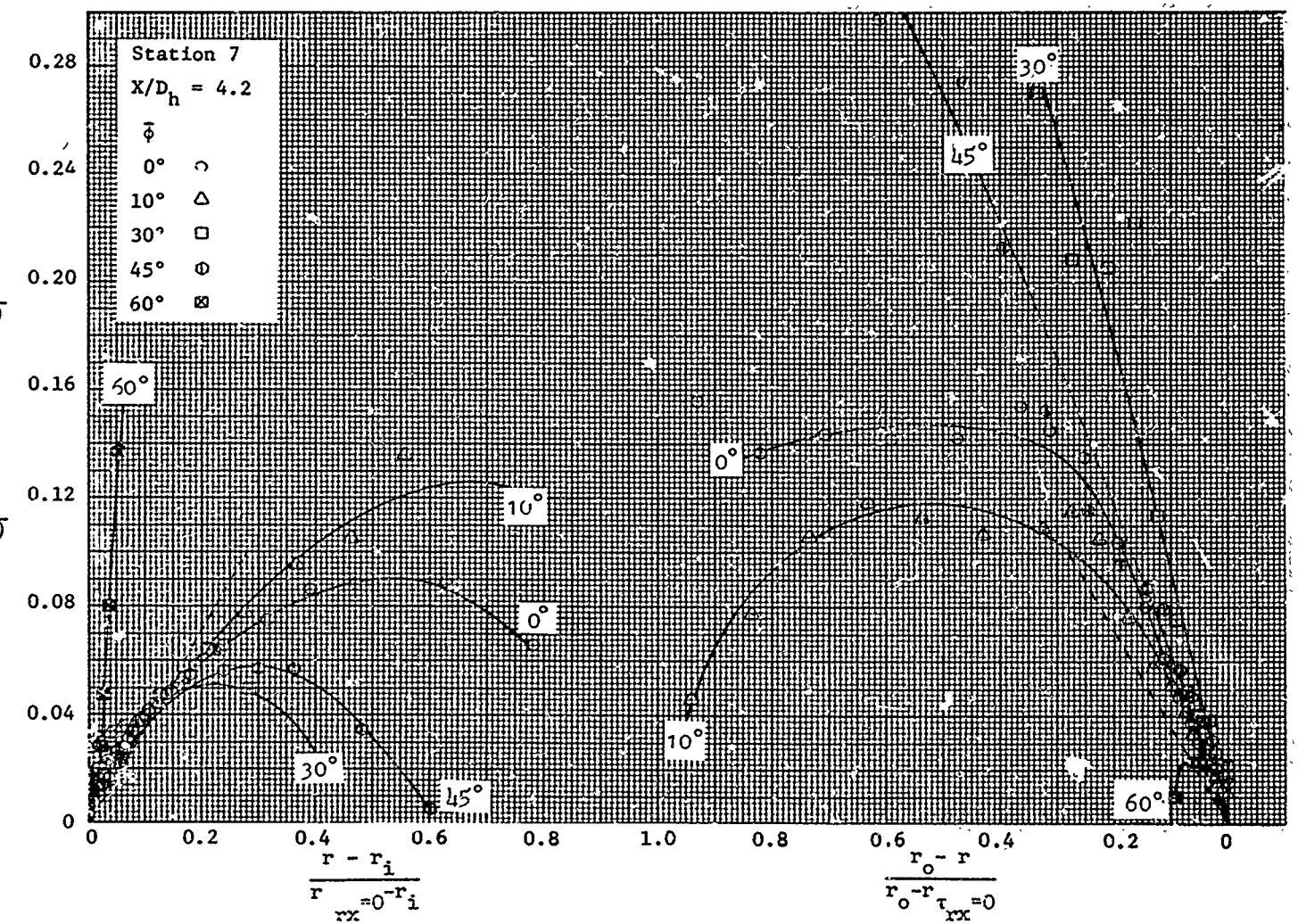

Figure 42. Dimensionless Axial Eddy Diffusivity--$X/D_h = 4.2$

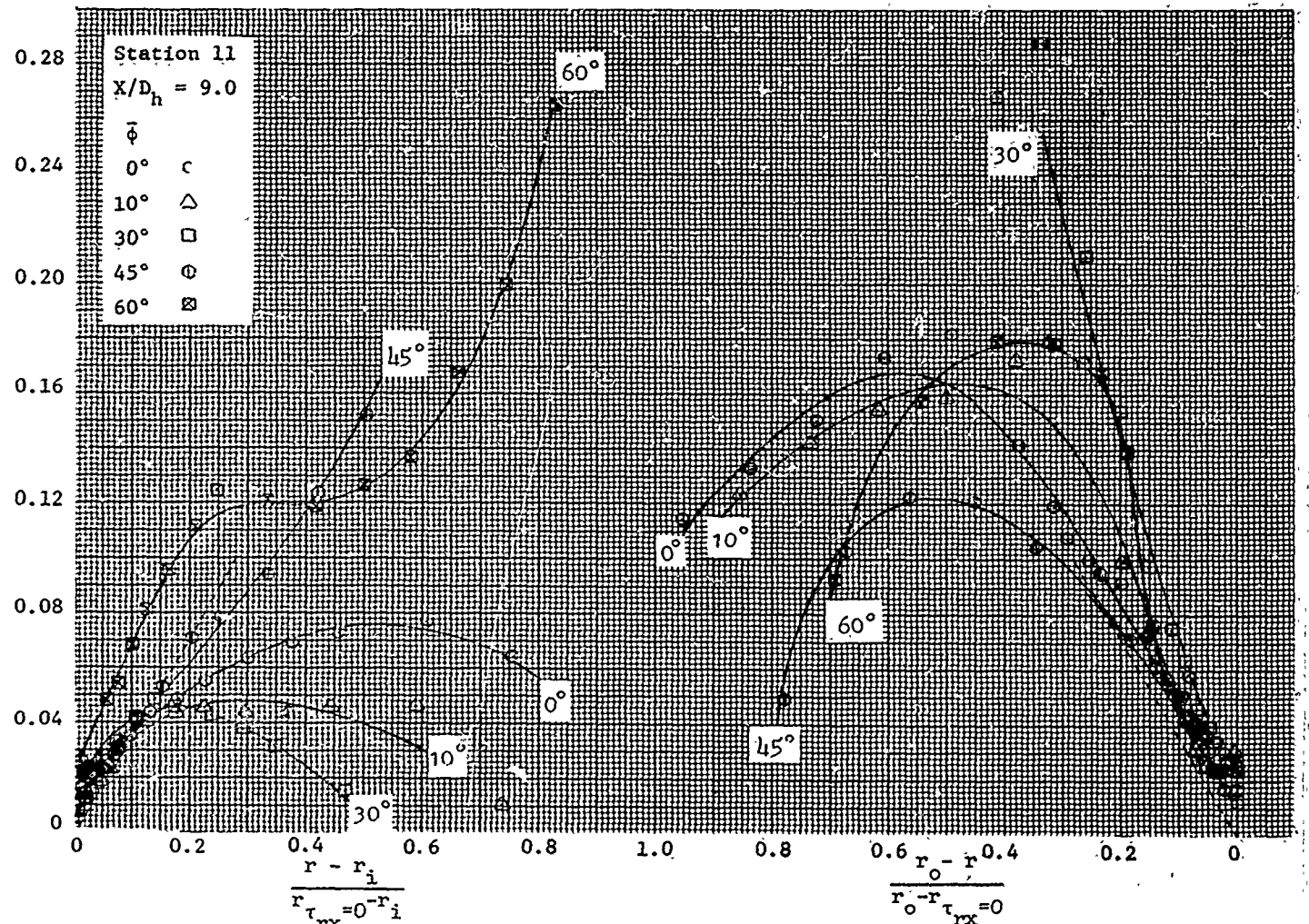

Figure 43. Dimensionless Axial Eddy Diffusivity--$X/D_h = 9.0$

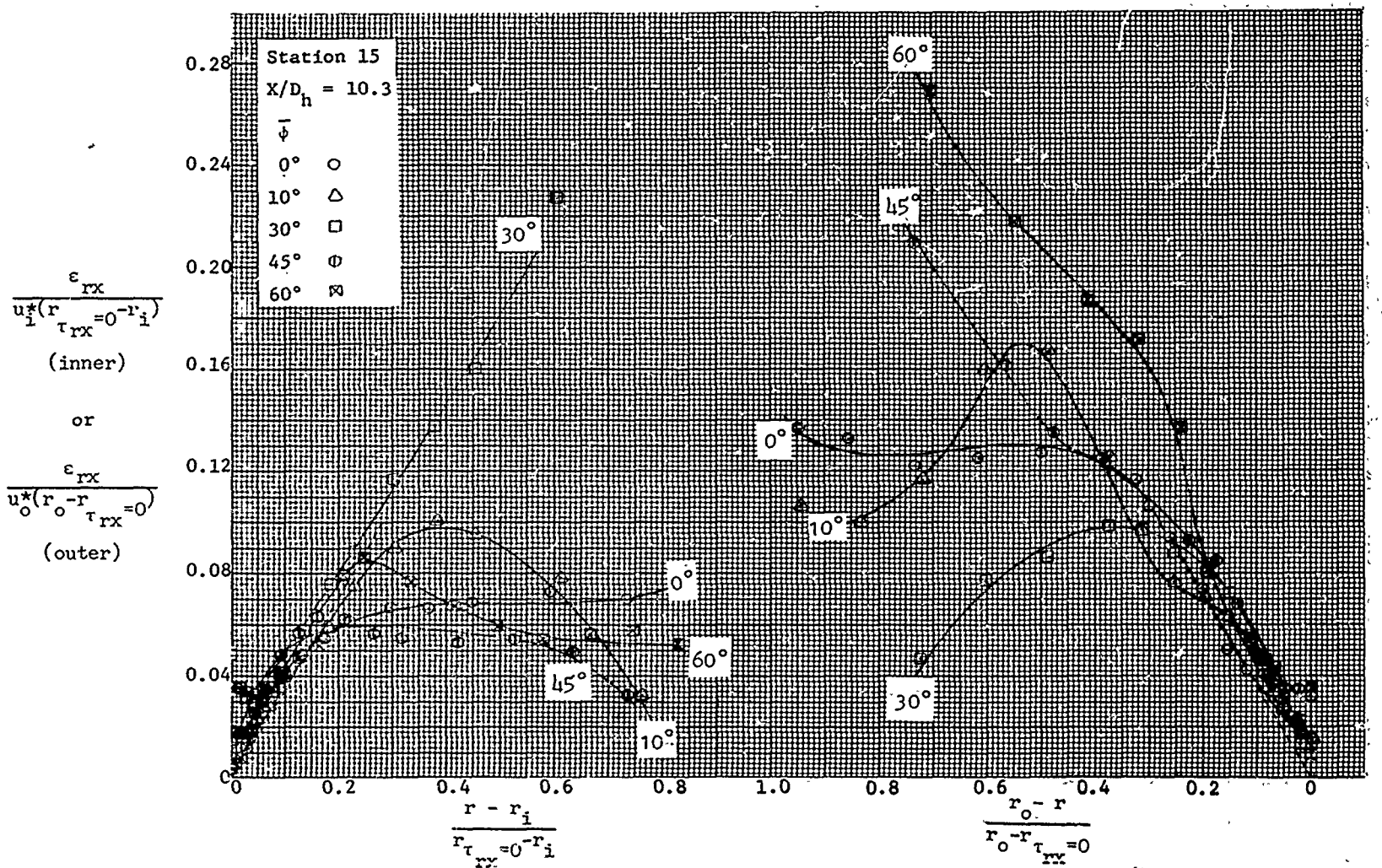

Figure 44. Dimensionless Axial Eddy Diffusivity--$X/D_h = 10.3$

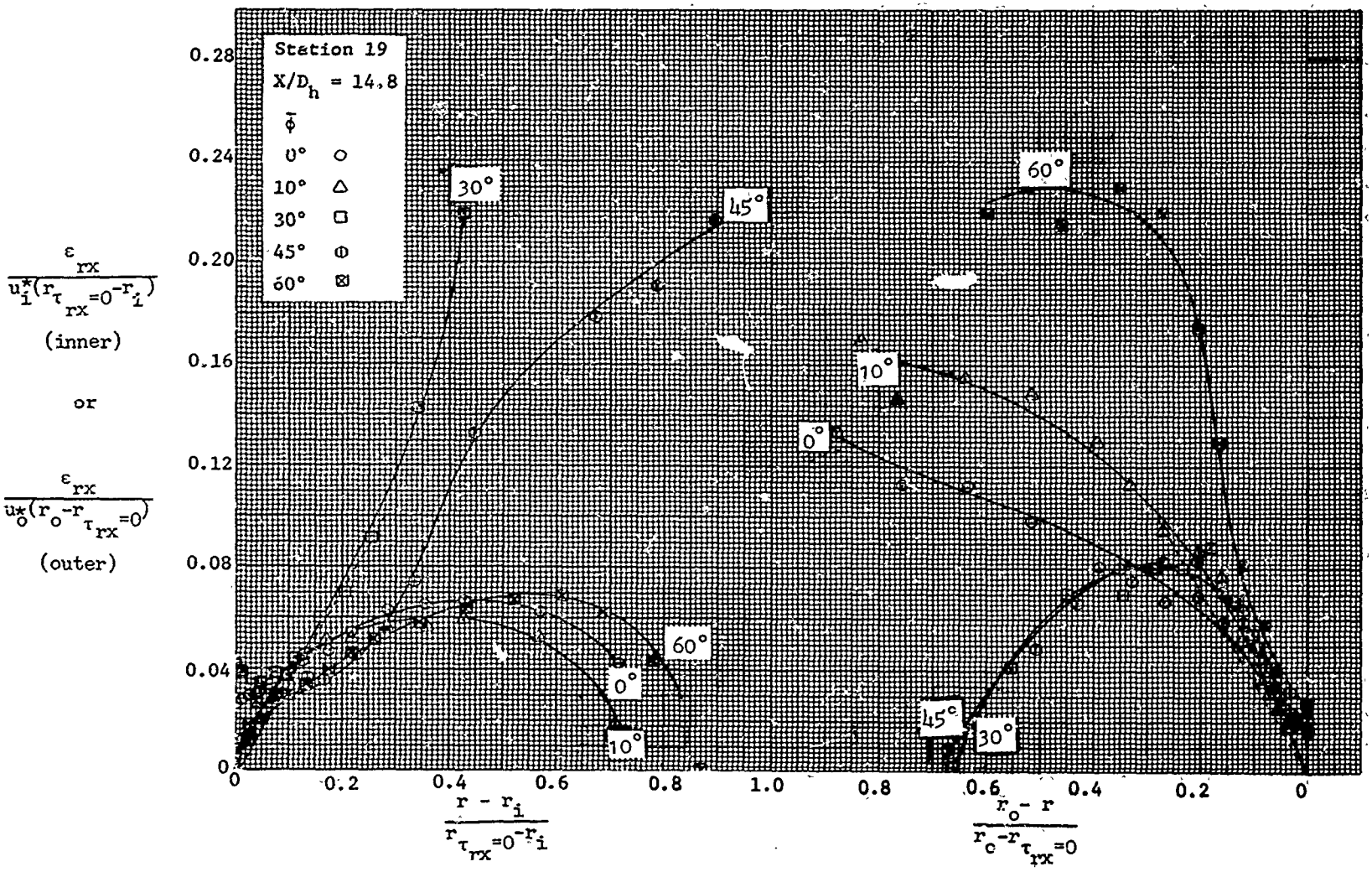

Figure 45. Dimensionless Axial Eddy Diffusivity--X/D_h = 14.8

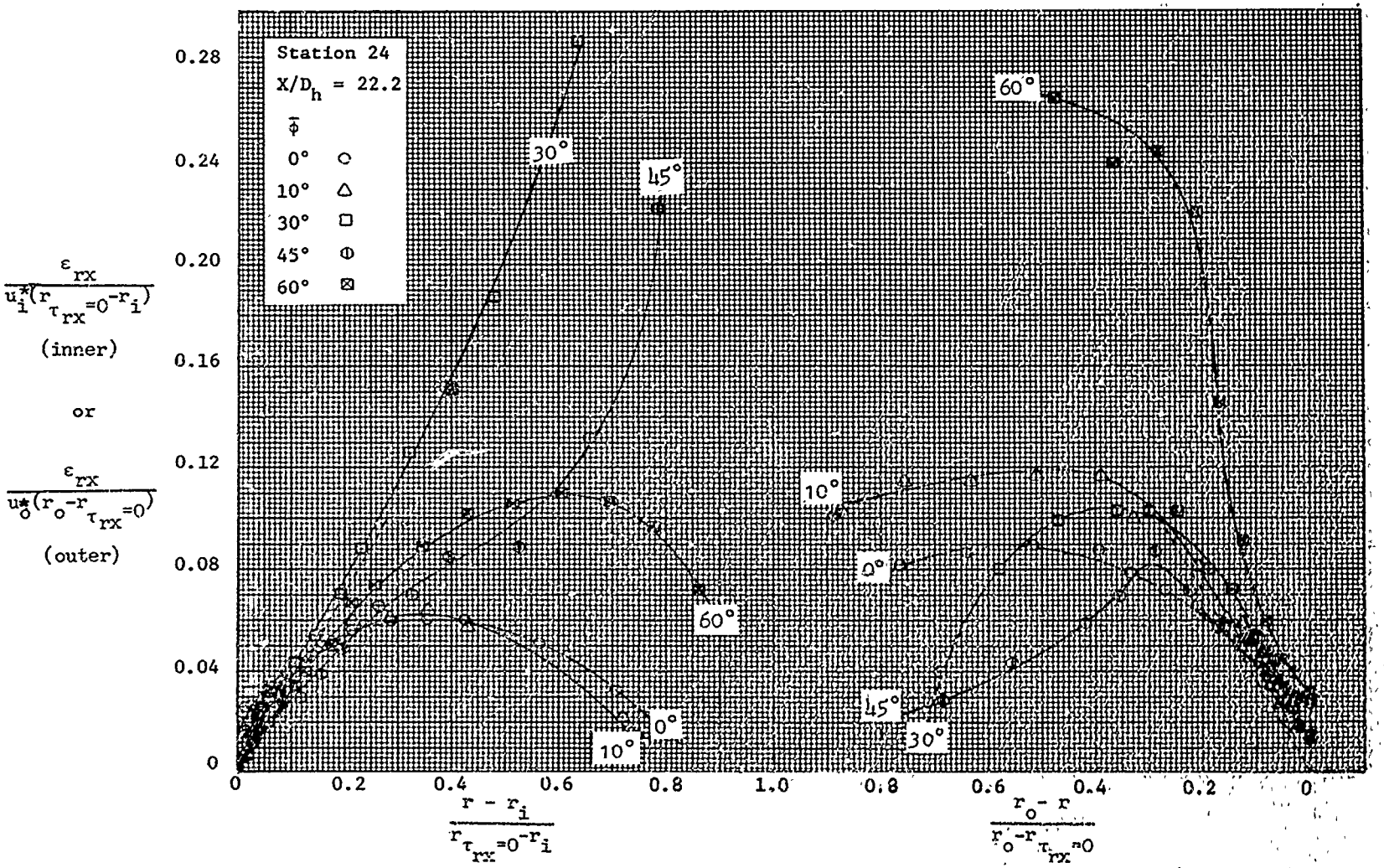

Figure 46. Dimensionless Axial Eddy Diffusivity---X/D_h=22.2

only, although it is quite surprising how close the slope of 0.4 matches much of the data--both axial and tangential--similar to the findings of Liu, et al. [66]. They observed that for a fourfold increase in surface roughness, the Karman constant is unaltered, and the value $\varepsilon_{rx}/u^*\delta$ is 0.09 for the outer half of a turbulent boundary layer.

Inspection of the limiting slopes in Figs. 42-46 reveal that for the axial diffusivities the Karman constant is unaltered by swirl for $\bar{\phi}$ = 0° - 45°. Values of $\varepsilon_{rx}/u^*\Delta r$ = 0.1 apply in the central core of the annulus for swirl angles of $\bar{\phi}$ = 0° and 10°. Larger axial diffusivity values appear whenever the local flow is more nearly the free-vortex type (wr = constant). That is, for low swirl rates, 0° and 10°, the inlet produced a nearly solid body rotation which does not alter the axial diffusivities. For $\bar{\phi}$ = 30° and 45°, the early x/D_h stations have a free vortex character and relatively large outer flow diffusivities. The $\bar{\phi}$ = 60° profiles behave differently. The free vortex character is suppressed at the early stations due to strong inlet pressure forces but is observed at the later stations.

The inner flow tangential diffusivity data depicted in Figs. 47-51 challenge the concept of mixing length. Expected positive slopes, $d\varepsilon_{r\theta}/dr$ later become negative. Spikes in the $\varepsilon_{r\theta}$ curves disappear at larger x/D_h. For the largest swirl rates, the diffusivities approach zero--a result in agreement with solid body flows. There is no clearly defined inner, tangential boundary layer. The velocity in this region is already increasing with a near forced-vortex character.

Spikes also occur in the outer flow tangential viscosity data. Large viscosities are observed for the low swirl angles. For $\bar{\phi}$ = 60°, the outer core flow viscosities agree remarkably well with the universal value of $\varepsilon_{r\theta}/w_o^* r_o$=0.028 derived by Kinney from Taylor's free vortex experiments with rotating cylinders

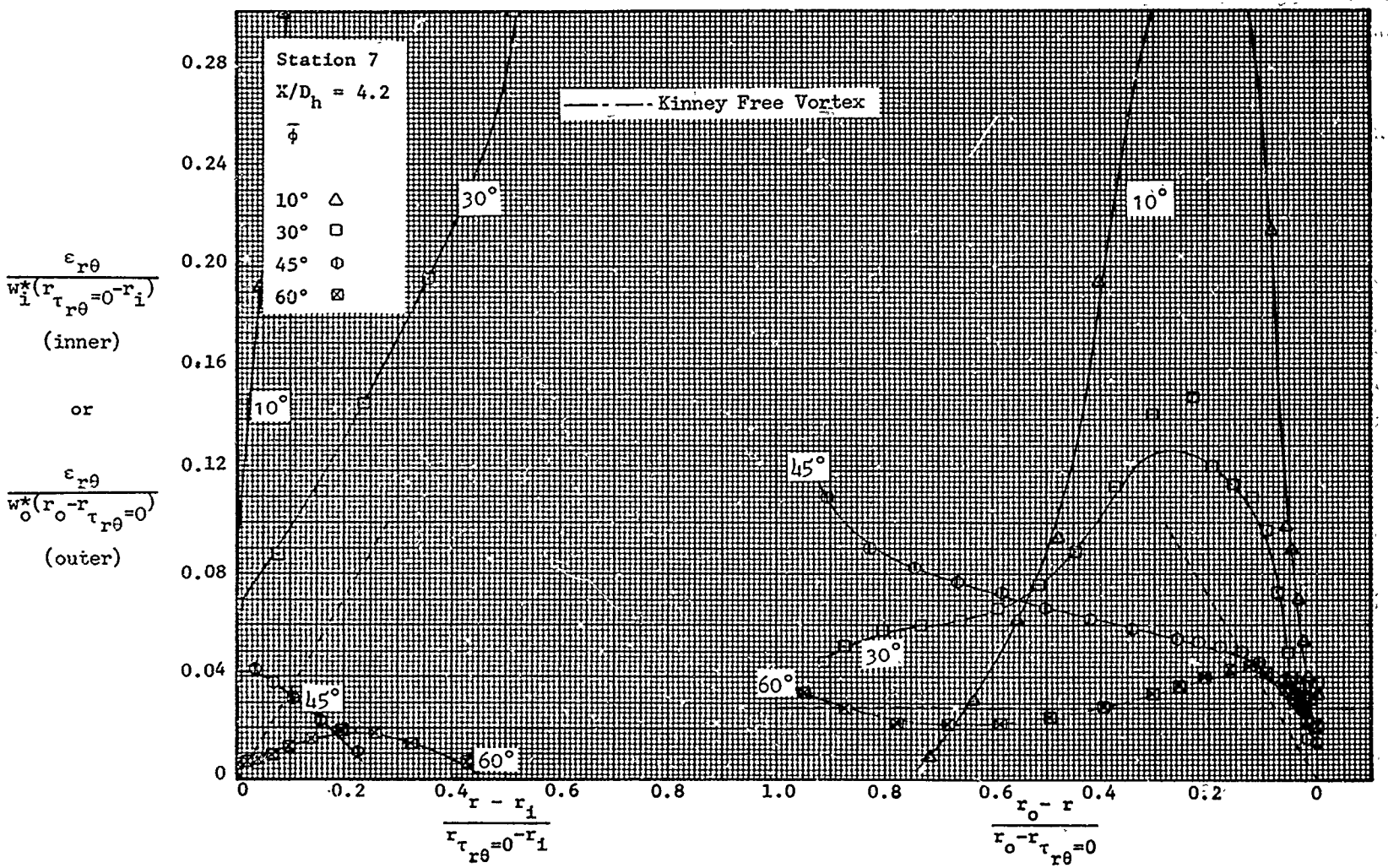

Figure 47. Dimensionless Tangential Eddy Diffusivity--X/D_h = 4.2

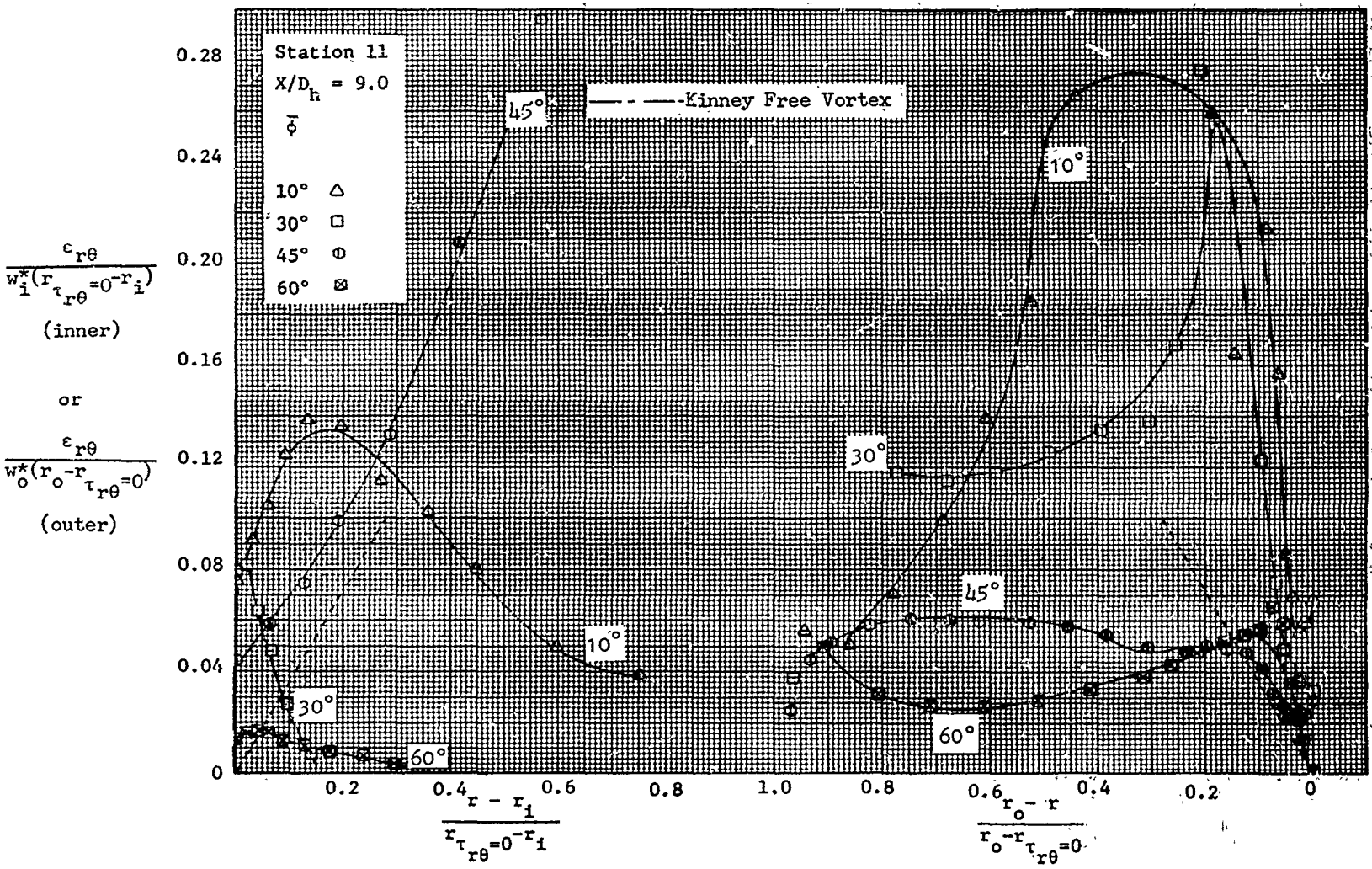

Figure 48. Dimensionless Tangential Eddy Diffusivity--$X/D_h = 9.0$

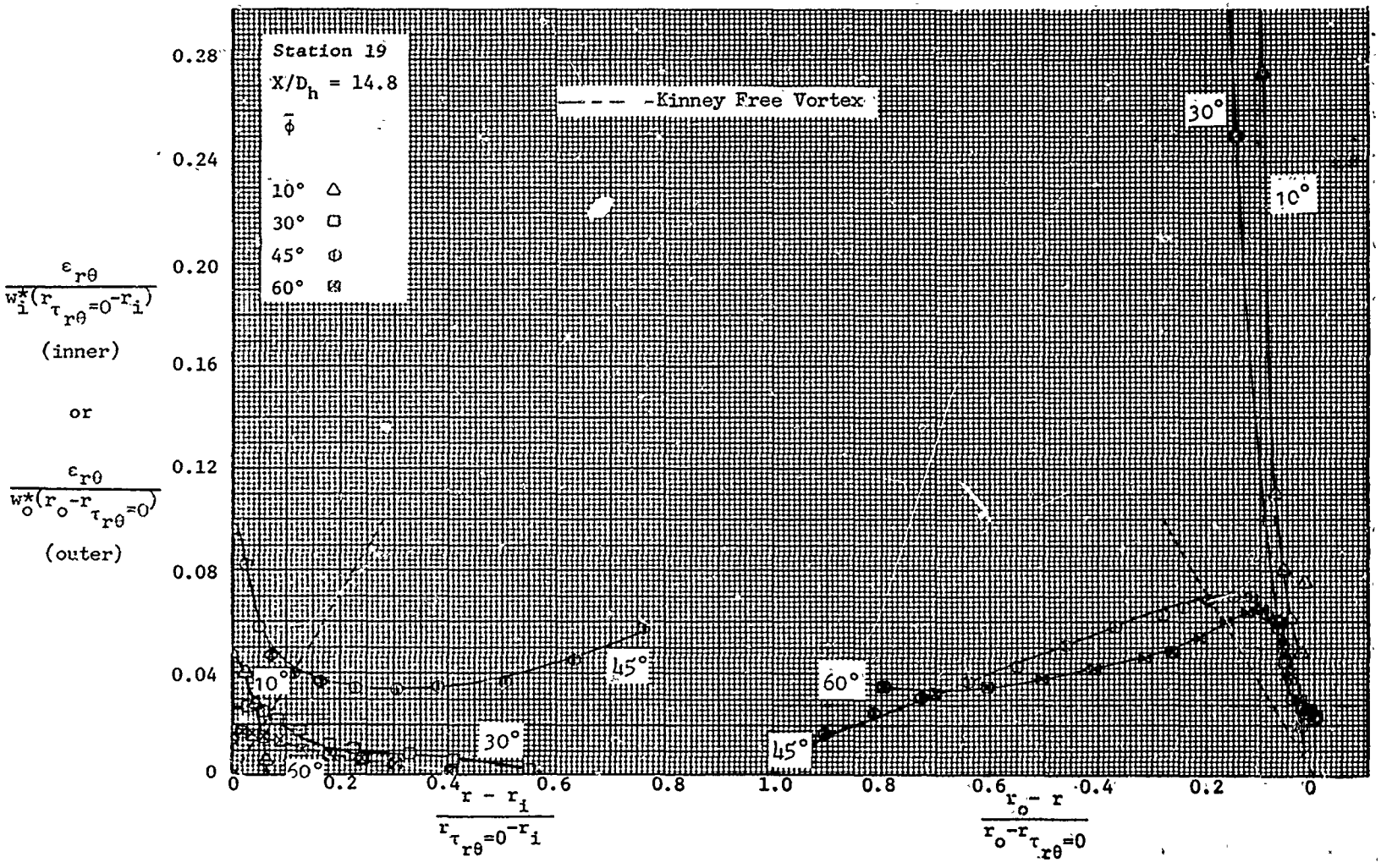

Figure 50. Dimensionless Tangential Eddy Diffusivity--X/D_h = 14.8

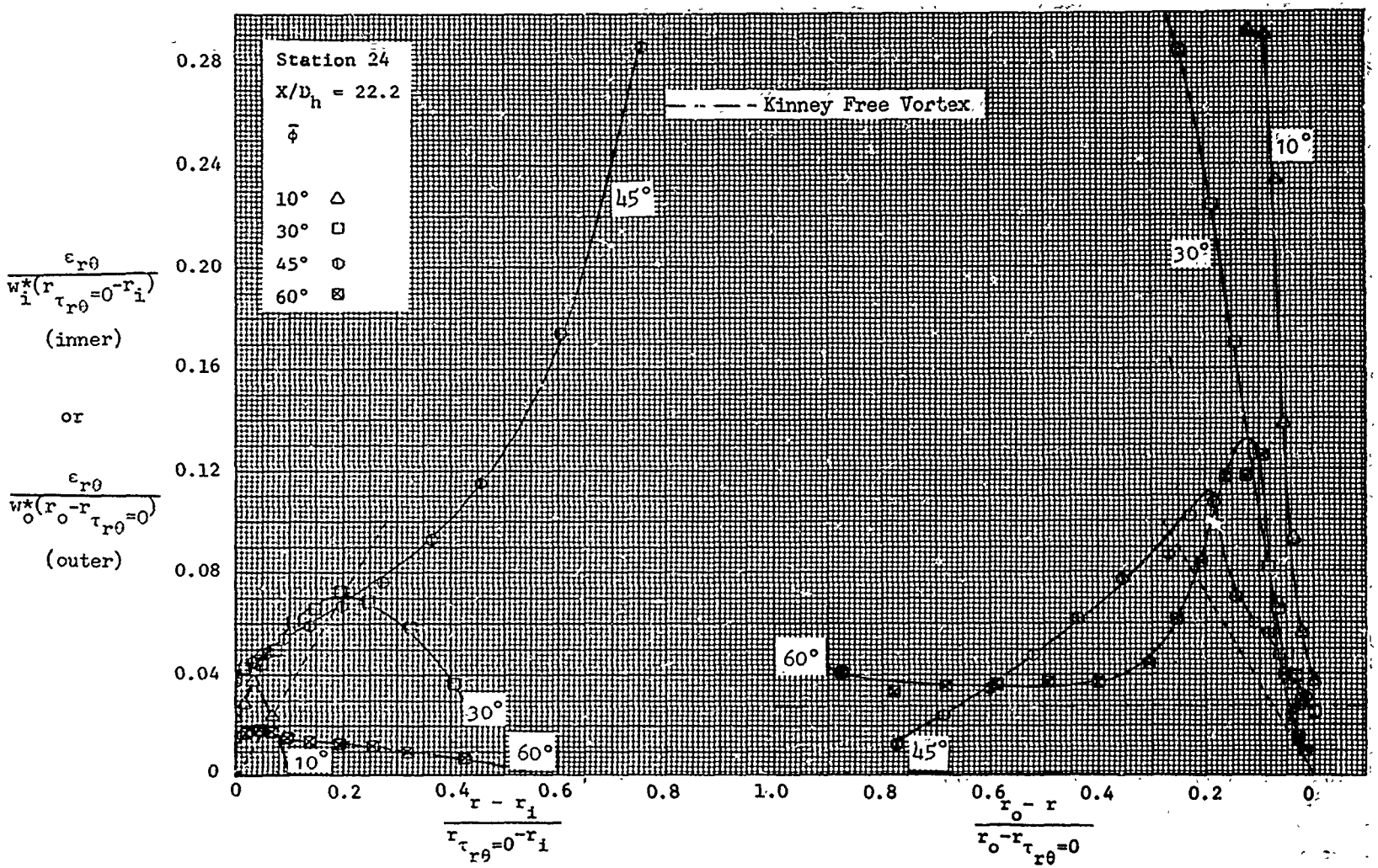

Figure 51. Dimensionless Tangential Eddy Diffusivity--X/D_h = 22.2

(in the absence of axial "carrier" flow). Near the outer wall, the slopes decrease sharply with increased swirl indicating that the Karman constant, $k = 0.4$ is sensitive to swirl, especially at the smaller swirl rates.

It appears that large deviations in turbulent diffusivities occur in regions where the character of the tangential velocity profile is changing from an essentially free vortex flow to an essentially forced vortex type of flow. The observed diffusivity values exhibit unexpected peaks temporarily as the gradient in angular momentum decreases from 0 to negative values. This is not a sharply defined quantity. A possible classification parameter is discussed in Appendix B.

The present method of determining turbulent transport coefficients involves integration and differentiation of large amounts of experimental profiles--a procedure which virtually guarantees a large amount of scatter. Secondly, some turbulence intensity terms were omitted in the integral equations because no equipment was available. In order to test the validity of these simplified equations, a complete static pressure field for all six of the Reynolds stresses, and a complete mean velocity field for all three components are all needed.

CONCLUSIONS

On the basis of the experimental results, the following remarks can be made (for the swirl rates tested):

1) The axial velocity profiles for $\overline{\phi} = 0°$ to 45°, at the first station had the characteristic shape of a fully developed profile because of the entrance conditions. At $\overline{\phi} = 60°$, the flow is approaching a reversed flow condition along the inner wall and hence the maximum velocity point has moved out closer to the outer wall.

2) For $\overline{\phi} = 10°$ to 45°, very little change was noted in the axial velocity profiles with swirl relative to those for straight flow.

3). The major characteristic noted in the decay of the tangential velocity for $\overline{\phi}$ = 10° to 45° was the change from a free vortex nature in the inlet to that of a forced vortex nature at the outlet. Also, the decay did not occur in a smooth, gradual fashion. For $\overline{\phi}$ = 60°, the forced and free vortex nature of the profiles did not change much with axial distance and the decay did occur in a smooth, gradual fashion.

4) The flow angle for $\overline{\phi}$ = 10° to 45° close to the inner wall exhibits a "snake-like" nature as one moves downstream. This was not noticed at the outer wall to any extent. At $\overline{\phi}$ = 45°, the path followed by the flow close to the inner wall would be similar to that followed if one could imagine himself walking along the coils of a spring that was in various degrees of tension alternating with compression along its length. No "snake-like" nature was noted in the flow angle with axial distance at the highest swirl rate tested.

5) Good to relatively poor agreement was obtained in the inner axial velocity profile between the data and the universal velocity distribution. The $\overline{\phi}$ = 60° data showed the poorest agreement.

6) No regular shift in the local axial skin-friction distribution at the inner wall is noted with increasing swirl rate for $\overline{\phi}$ = 0° to 45°. A definite decrease in the axial skin-friction seems to occur in the inlet region for $\overline{\phi}$ = 45°. To generalize, no significant change in axial skin-friction coefficient was found with swirl rates up to $\overline{\phi}$ = 30°. The $\overline{\phi}$ = 60° distribution shows a definite decrease in the axial skin-friction coefficient.

7) It appears as though the axial pressure gradient will approach a fully developed state before the swirl completely decays.

8) Five distinct zones were observed in the tangential velocity profile.

9) Pitot cylinder and hot film probe velocity profiles are in agreement in the central annular core. The pitot cylinder indicates high velocities near solid boundaries.

10) Preston tube and Clauser chart determinations of axial and tangential shear components agreed within 15 percent for the inner wall shear.

11) Axial and tangential shear stress profiles were computed from integral-differential forms of the conservation equations using the measured velocity profiles in the integrands. Turbulence intensity terms were not measured and were excluded.

12) Axial and tangential diffusivities were computed from the appropriate shear profiles computed from the integral-differential equations and a Boussinesq hypothesis relating the turbulent Reynolds stress to the rate of deformation. In general, the location of zero shear stress did not occur where the rate of deformation was zero and their ratio, the diffusivity, approached infinity-both positively and negatively.

13) Axial diffusivities are weakly influenced by swirl. This is probably due to the fact that the axial velocity profile is only mildly influenced by swirl.

14) For axial diffusivities, the Karman constant is unaltered by swirl.

15) The tangential diffusivities behave in much the same manner as those observed in curved channels.

16) At large swirl rates where the tangential swirl has a free vortex character, the outer flow diffusivities agree with the universal value $\varepsilon_{r\theta}/w^*_o r_o = 0.028$ derived by Kinney from Taylor's free vortex experiments with rotating cylinders.

17) Large spikes in the tangential viscosities occur in regions where the character of the tangential velocity profile is changing from essentially free vortex to forced vortex nature.

18) Kinney's conclusion that states that in plane curved turbulent flows which possess universal similarity, the angular velocity is a transferable quantity in the same sense as linear momentum is a transferable quantity in rectilinear flows, also applies for nonsimilar profiles with an axial carrier flow.

APPENDIX A. Comparisons Between Pitot Cylinder Probe and Hot Film Probe

The hot film probe used was purchased from Thermo-Systems, Inc., St. Paul, Minnesota. A hot film sensor was selected instead of a hot wire sensor because the film sensor is more rugged and less susceptible to fouling. The model number of the probe was 1270-10-6. The diameter of the film sensor was 0.001 inches and the sensing length was 0.020 inches. The anemometry system used was a Thermo-Systems, Inc. constant temperature anemometer, model 1050. The instructions for operating the anemometer are given in the instruction manual for the Model 1050 anemometer.

A Beckman voltage to frequency converter, Model 651, and frequency counter, Model 6148, were connected to the output of the anemometer to monitor the voltage readings. The instrument was accurate to within 0.3%. This setup provided an easy to read digital output and the capability of averaging the input signal, in this case the output of the anemometer, over a ten second gate time.

Typical axial and tangential velocity data gathered with the two probes are presented in Figs. 52 and 53. The hot film flow angles could not be determined as accurately with the hot film probe as they could be with the pressure probe (see Figure 53). The resolution obtainable with the hot film probe was not as great as that of the pressure probe. The flow angles determined with the hot film probe are believed to be within ±1° at best and ±4° at worst. Most of the flow angles determined with the two probes agree within ±2°. The majority of the flow angles determined with the pressure probe are believed to be within ±1/2° or better. Very close to the inner wall at high swirl rates, i.e., at $\bar{\phi} = 45°$, it is believed that the pressure probe gives false, high readings. In equation 7, it is shown that the radial pressure gradient is directly proportional to the square of the tangential velocity divided by the

radius

$$\frac{w^2}{r} = \frac{1}{\rho}\frac{\partial p}{\partial r} \tag{37}$$

As a result, at high swirl rates the resulting downwash or crossflow along the probe and the nature of the flow around the probe is probably quite different than that occuring with weak swirl. Near the inner, wall, the smaller-dimensioned hot film probe should not disturb the flow as severely as the pressure probe or be affected by the downwash. Because of these reasons, it is felt that the pressure probe gives false readings and that the hot film values are closer to the actual values in this instance.

The total velocity measured with the pressure probe near the inner wall at $\overline{\phi} = 45°$ was also somewhat higher than that measured with the hot film probe.

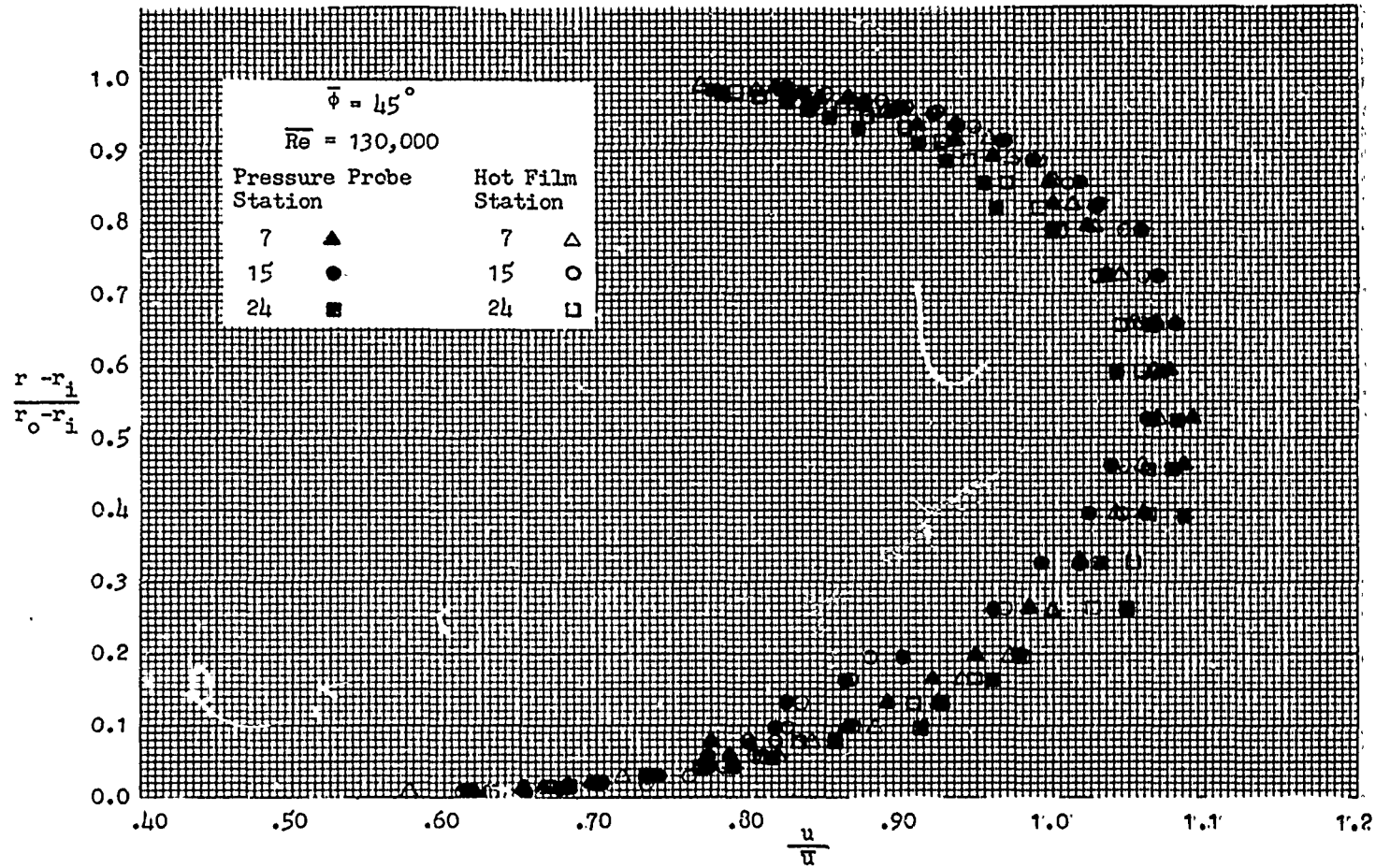

Figure 52. Hot Film and Pressure Probe Axial Velocities.

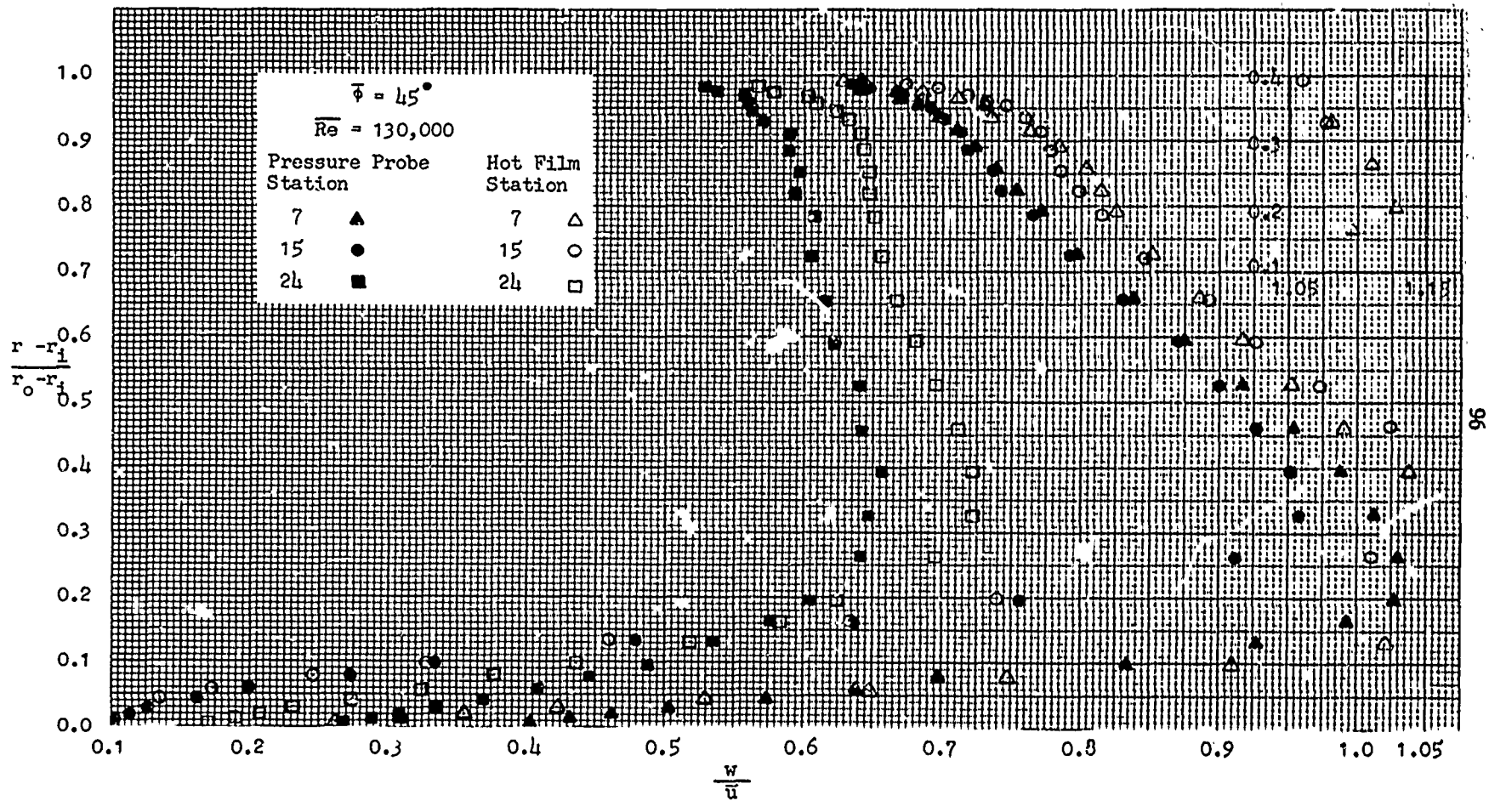

Figure 53. Hot Film and Pressure Probe Tangential Velocities.

APPENDIX B. Approximate Locus of Maximum Turbulent Diffusivity

If the flow can be written in the form $w = cr^m$, then $r/u \cdot du/dr = m$, where $m = +1$ for forced flow and $m = -1$ for free flow; we note that $m = 0$ ($dw/dr = 0$) is a useful boundary between the two flows. The location of zero swirl velocity gradient is not, however, the location where viscosity spikes are observed.

In classifying this character, neither the rate of deformation or the vorticity gives a sharp change. Consider the following table

Mixed Flow Classification

Flow Type	Free Vortex	Forced Vortex
Velocity $w =$	$C_1/r > 0$	$C_2 r > 0$
Velocity Gradient $dw/dr =$	$-C_1/r^2 < 0$	$C_2 > 0$
Deformation Rate		
$D = dw/dr - w/r =$	$-2C_1/r^2$	0
Vorticity		
$F = dw/dr + w/r =$	0	$2C_2 > 0$
Product of D·F		
$DF = (dw/dr - w/r)(dw/dr + w/r)$		
$=[(dw/dr)^2 - (w/r)^2]$	< 0	> 0

Inspection of the present turbulent diffusivity data reveals that the local maximums occur close to the position where the product DF is equal to zero. The diffusivity data appear to be most accurate outside these two points - closer to the walls.

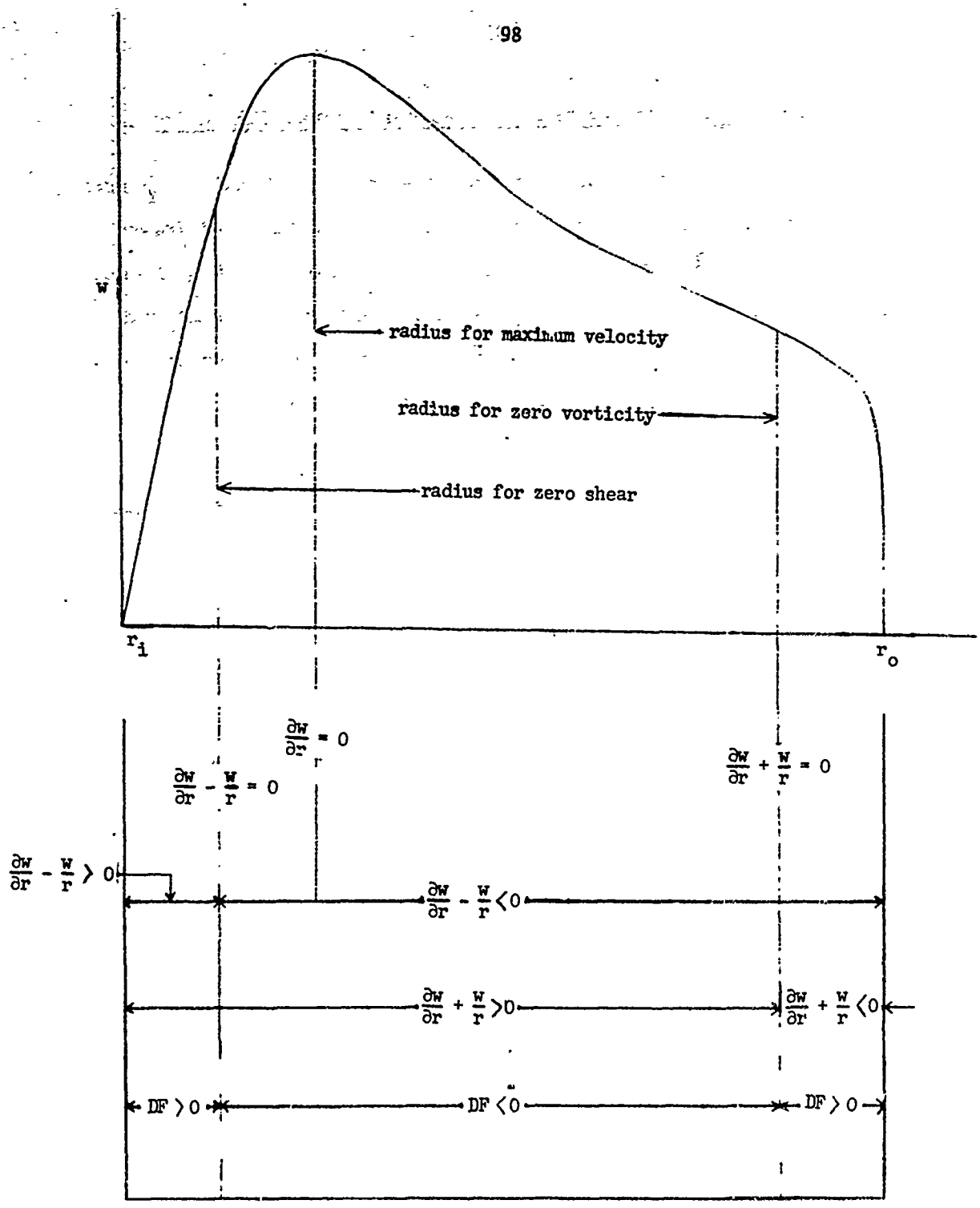

Figure 54. Approximate Location of Tangential Diffusivity "Spikes".

REFERENCES

1. International Union for Theoretical and Applied Mechanics, "Concentrated Vortex Motions in Fluids," University of Michigan, Ann Arbor, Michigan, July 6-11, 1964.

2. Kuchemann, D., "Progress in Aeronautical Sciences," Vol. 7, Pergamon Press Ltd., 1966.

3. King, M. K., Rothfus, R. R., and Kermode, R. I., "Static Pressure and Velocity Profiles in Swirling Incompressible Tube Flow," A.I.Ch.E Journal, Vol. 15, Nov. 6, pp. 837-842, November, 1969.

4. Bossel, H. H. K., "Inviscid and Viscous Models of the Vortex Breakdown Phenomenon," University of California, Berkeley, College of Engineering Report No. AS-67-14, August, 1967

5. Rayleigh, J. W. S., "On the Dynamics of Revolving Fluids," Proc. Royal Soc., Vol. 6A, pp. 148-154, 1916.

6. Taylor, G. I., "Distribution of Velocity and Temperature Between Concentric Rotating Cylinders," Proc. Royal Soc., London, pp. 494-512, 1935; also, "The Scientific Papers of G. I. Taylor," Vol. 2, Cambridge University Press, pp. 336-350, 1960.

7. Taylor, G. I., "Fluid Friction Between Rotating Cylinders. Part I: Torque Measurements," Proc. Royal Soc., London, Series A, Vol. 157, pp. 546-564, 380-396, 1936.

8. Taylor, G. I., "Fluid Friction Between Rotating Cylinders. Part III: Distribution of Velocity Between Concentric Cylinders when Outer One is Rotating and Inner One is at Rest," Proc. Royal Soc., London, Series A, Vol. 157, pp. 565-578, 397-408, 1936.

9. Görtler, H., "Über einer dredimensionale Instabilität laminarer Grenzschichten an konkaven Wänder, ZAMM, Vol. 21, pp. 250-252, 1941.

10. Wattendorf, F. L., "A Study of the Effect of Curvature on Fully Developed Turbulent Flow," Proc. Royal Soc., Vol. 148, pp. 565-598, 1935.

11. Eskinazi, S. and Yeh, H., "An Investigation on Fully Developed Turbulent Flows in a Curved Channel," J. Aero. Sci., Vol. 23, No. 1, January, 1956.

12. Margolis, D. P. and Lumley, J. L., "Curved Turbulent Mixing Layer," Physics Fluids, Vol. 8, No. 10, pp. 1775-1785, October, 1965.

13. Kline, S. J., Markovin, H. V., Sovran, G. and Cockrell, D. J., "Computation of Turbulent Boundary Layers. Vol. I: Methods, Predictions, Evaluation and Flow Structure," Proc. AFOSR-IFP-Stanford Conference, 1968, Stanford University, California.

14. Westley, R., "A Bibliography and Survey of the Vortex Tube," College of Aeronautics, Cranfield, England, 1954.

15. Kreith, F., "Convective Heat Transfer in Rotating Systems, "Advances in Heat Transfer, Vol. 5, pp. 129-251, 1968.

16. Lavan, Z. and Fejer, A. A., "Investigation of Swirling Flows in Ducts," ARL-66-0083, Aerospace Research Laboratories, USAF, Wright-Patterson AFB, Ohio, May, 1966.

17. Gambill, W. R. and Bundy, R. D., "An Evaluation of the Present Status of Swirl-Flow Heat Transfer, Paper 62-HT-42, ASME-AIChE Heat Transfer Conference, August, 1962.

18. Ranque, G. J., "Method and Apparatus for Obtaining from a Fluid Under Pressure two Currents of Fluids at Different Temperature," United States Patent Office No. 1, 1952, 281. Patented, March 27, 1934.

19. Milton, R. M., "Maxwellian Demon at Work," Industrial and Engineering Chemistry, Vol. 38, No. 5, 1946.

20. Reed, G. A., "Vortex Tube Refrigeration, "M.S. Thesis, M.I.T., 1947.

21. Kassner, R. and Knoernschild, R., "Friction Laws and Energy Transfer in Circular Flow," USAF Technical Report F-TR-2198-ND, Wright-Patterson AFB, Ohio, 1947.

22. Deissler, R. G. and Perlmutter, M., "An Analysis of the Energy Separation in Laminar and Turbulent Compressible Vortex Flows," Heat Transfer and Fluid Mechanics Institute, 1958.

23. Deissler, R. G. and Perlmutter, M., "Analysis of the Flow and Energy Separation in Turbulent Vortex," Int. J. Heat Mass Transfer, Vol. 1, No. 2/3, pp. 173-191, August, 1960.

24. Donaldson, C. duP. and Sullivan, R. D., "Examination of the Solutions of the Navier Stokes Equations for a Class of Three-Dimensional Vortices," Heat Transfer and Fluid Mechanics Institute, 1960.

25. Kreith, F. and Margolis, D., "Heat Transfer and Friction in Turbulent Vortex Flow," Appl. Sci. Res., Vol. 8, Sec. A., pp. 457-473, 1959.

26. Smithberg, E. and Landis, F., "Friction and Forced-Convection Heat Transfer Characteristics in Tubes with Twisted Tape Swirl Generators," J. Heat Transfer, Vol. 86, pp. 39-49, February, 1964.

27. Thorson, R. and Landis, F., "Friction and Heat Transfer Characteristics in Turbulent Swirl Flow Subjected to Large Transverse Temperature Gradients," J. Heat Transfer, Vol. 90, pp. 87-97, February, 1968.

28. Hartnett, J. P. and Eckert, E. R. G., "Experimental Study of the Velocity and Temperature Distribution in a High Velocity Vortex Type Flow," Trans.ASME, Vol. 79, pp. 751-758, 1957.

29. Ragsdale, R. G., "NASA Research on the Hydrodynamics of the Gaseous Vortex Reactor," NASA TN D-288, September, 1960.

30. Keyes, J. J., "An Experimental Study of Gas Dynamics in High Velocity Vortex Flow," Heat Transfer and Fluid Mechanics Institute, 1960.

31. Kerrebrock, J. L. and Meghreblian, R. V., "Vortex Containment for the Gaseous Fission Rocket," J. Aerospace Sci., Vol. 28, p. 710, 1961.

32. Reynolds, A. J., "On the Dynamics of Turbulent Vortical Flow," Zeitschrift fur angewandte Mathematik und Physik, Vol. 12, p. 149 and p. 343, 1961.

33. Kendall, J. M., "Experimental Investigation of a Compressible Viscous Vortex," Jet Propulsion Lab., TR No. 32-290, June, 1962.

34. Sibulkin, M., "Unsteady Viscous Circular Flow, Part 3, Application to the Ranque-Hilsch Vortex Tube," J. Fluid Mech., Vol. 12, pp. 289-293, 1962.

35. Collatz, L. And Görtler, G., "Rohrstromung mit schwachen Drall," Zeitschrift fur angewandte Mathematic and Physik, Vol. 5, pp. 95-110, 1954.

36. Talbot, L., "Laminar Swirling Pipe Flow," J. Appl. Mech., Vol. 76, 1954.

37. Kreith, F. and Sonju, O. K., "The Decay of Turbulent Swirl in a Pipe," J. Fluid Mech., Vol. 22, Part 2, pp. 257-271, 1965.

38. Rochino, A. P. and Lavan, Z., "Analytical Investigation of Incompressible Turbulent Swirling Flows in Pipes," NASA CR-1169, September, 1968.

39. Scott, C. J., "A Series Solution for Decay of Swirl in an Annulus," J. of Appl. Mech., March 1972.

40. Musolf, A. O., "An Experimental Investigation of the Decay of Turbulent Swirl Flow in a Pipe," M.S. Thesis, University of Colorado, 1963.

41. Persen, L. N., "Preliminary Analytical Explorations of Heat Transfer from Boundary Layers Containing Streamwise Vortices," Office of Aerospace Research, ARL 67-0280, Wright-Patterson AFB, Ohio, December, 1967.

42. Rask, D. R. and Scott, C. J., "Decay of Turbulent Swirl in an Annular Duct," University of Minnesota, Department of Mechanical Engineering, HTL No. 89, 1970.

43. Boerner, C. J., "Numerical Solution of Turbulent Annular Swirl Flows," University of Minnesota, Department of Mechanical Engineering, HTL No. 93, July, 1970.

44. Palanek, E. J., "Experimental Study of Vortex Flow in a Cylinder," M.S. Thesis, GAM 55A/AE/66-6, Wright-Patterson AFB, Ohio.

45. Talcott, R. C., "Experimental Investigation of the Heat Transfer from a Coaxial Heat Source to Confined Straight Axial or Vortex Flow," M.S. Thesis, GAM 65AE/65-5, Wright-Patterson AFB, Ohio.

46. Yeh, H., "Boundary Layer Along Annular Walls in a Swirling Flow," NASA TN-57-105, April, 1957.

47. Acharya, Y. V. G., Krishnamurthy, K. and Irani, P. A., "Investigation on Vortex Flows," TN-AE-28-65 National Aeronautical Laboratory, Bangalore, India.

48. L. Prandtl, "Einfluss Stabilisierender Kräfte auf die Turbulenz," Vortage auf dem Gebeite der Aerodynamik und verwandter Gebiete, Aachen, 1929.

49. Kinney, R. B., "Universal Velocity Similarity in Fully Turbulent Rotating Flow," J. Appl. Mech., Vol. 34, ASME Trans. Vol. 89, pp. 437-442, June, 1967.

50. Erian, F. F., "The Influence of Pressure Gradient on Turbulent Flows with Asymmetric Mean Velocity," J. Appl. Mech., pp. 901-904, December 1969.

51. Hinze, J. O., Turbulence, McGraw-Hill, 1959.

52. Olson, R. M. and Sparrow, E. M., "Measurements of Turbulent Flow Development in Tubes and Annuli with Square or Rounded Entrances," AIChE Jl., Vol. 9, No. 6, pp. 766-777, 1963.

53. Okiishi, T. H. and Serovy, G. K., "An Experimental Study of the Turbulent Flow-Boundary Layer Development in Smooth Annuli," ASME Paper No. 67 - WA/FE - 10.

54. Thom, H., British Rand M. No. 1194, British ARC, 1928.

55. Glaser, A. H., "The Pitot Cylinder as a Static Pressure Probe in Turbulent Flow," J. Sci. Instr., Vol 29, No. 7, pp. 219-221, 1952.

56. Bruun, H. H., "Experimental Investigation of the Energy Separation in Vortex Tubes," British J. Mech. Engng Sci., Vol. 11, No. 6, pp. 567-582, 1969.

57. Laufer, J., "The Structure of Turbulence in Fully Developed Pipe Flow," NACA TR 1174, 1954.

58. Nikuradse, J., "Untersuchungen uber die Geschwindigkeitsverteilung in turbulenten Strommgen," Thesis, Gottingen, 1926. Also, VDI-Forschungsheft, p. 281, 1926.

59. Brighton, J. A. and Jones, J. B., "Fully Developed Turbulent Flow in Annuli, J. Basic Engng., Vol. 86, No. 4, 1964, pp. 835-844.

60. J. G. Knudsen and D. L. Katz, "Velocity Profiles in Annuli," Proceedings, Midwestern Conference on Fluid Dynamics, pp. 175-203, May, 1950.

61. Clauser, F. H., "Turbulent Boundary Layers in Adverse Pressure Gradients," J. Aeronautical Sci., Vol. 21, No. 2, pp. 91-108, February, 1954.

62. Pierce, F., "Three Dimensional Turbulent Boundary Layers," Proceedings, Symposium on Fluidics and Internal Flows, Penn. State University, pp. II-97-150, 1969.

63. Preston, J. H., "The Determination of Turbulent Skin Friction by Means of Pitot Tubes," J. Royal Aero. Soc. Vol. 58, 1954.

64. Jonsson, V. K., "Experimental Studies of Turbulent Flow Phenomena in Eccentric Annuli," Ph.D. Thesis, University of Minnesota, Minneapolis, Minnesota, August 1965.

65. Wasan, D. T., Tien, C. L., and Wilke, C. R., "Theoretical Correlation of Velocity and Eddy Viscosity for Flow Close to a Pipe Wall," A.I.Ch.E. Jl.. Vol. 9, No. 4, pp. 567-569, 1963.

66. Lui, C. K., Kline, S. J., and Johnson, J. P., "An Experimental Study of the Turbulent Boundary Layer on a Rough Wall," Thermosciences Div., Mech. Engng. Dept., Report MD-15, Stanford University, 1966.